



UNIVERSITÀ DELLA
CALABRIA


UNIVERSITÀ DELLA CALABRIA
Dipartimento di Fisica

Dottorato di Ricerca in
Scienze e Tecnologie Fisiche, Chimiche e dei Materiali
CICLO XXXIII


**Cryobiophysics: librational dynamics and solvent
accessibility in the low-temperature phases
of supramolecular aggregates**

Settore Scientifico Disciplinare FIS/07


Coordinatrice: Prof.ssa Gabriella Cipparrone

 Firma oscurata in base alle linee
guida del Garante della privacy

Supervisore: Prof.ssa Rosa Bartucci

 Firma oscurata in base alle linee
guida del Garante della privacy

Dottoranda: Dott.ssa Erika Aloï

Firma oscurata in base alle linee
guida del Garante della privacy 

*A Giulio Regeni,
cittadino del mondo*

*A Patrick Zaki,
e alla sua libertà*

Contents

Abstract (<i>Italian</i>)	1
Abstract (<i>English</i>)	3
1 Introduction	5
2 Electron Paramagnetic Resonance	12
2.1 A short history of EPR	12
2.2 The EPR phenomenon	13
2.2.1 Zeeman interaction	13
2.2.2 Hyperfine interaction	15
2.2.3 The nitroxide spin labels	15
2.2.4 Librational motion from cw-EPR	18
2.3 Fourier-Transform EPR	19
2.4 Electron Spin Echo	19
2.5 Librational motion from ED-EPR spectra	21
2.6 ESEEM spectroscopy	25
2.6.1 Three-pulse ESEEM	26
2.6.2 D ₂ O-ESEEM	29
3 Materials and methods	32
3.1 Materials	32
3.2 Sample preparation	32
3.3 EPR measurements	33

4	Water penetration in biosystems	35
4.1	Lyotropic phase behavior of bilayer-forming lipids and micelle-forming lipids mixtures	36
4.1.1	Diacyl- and polymer-lipids mixtures	36
4.1.2	Diacyl- and Lyso-lipids mixtures	42
4.2	Interdigitated lamellar phases	46
4.3	Micellar phases	50
4.4	Membrane protein: the case of Na ⁺ ,K ⁺ -ATPase	54
5	Dynamics of lipid assemblies at cryogenic temperatures	62
5.1	Librational dynamics of unsaturated bilayers	62
5.2	Angular librational oscillations in interdigitated lamellar phases	70
5.3	Dynamical transition	74
6	Role of hydration water in the dynamical properties of proteins and lipid membranes	77
6.1	Effect of hydration on librational oscillations of α vs β globular proteins	78
6.2	Effect of hydration on segmental librational oscillations of lipid bilayers	81
7	Hydration water dynamics in tau protein from neutron scattering data analysis	87
7.1	Quasi elastic neutron scattering: theoretical background	87
7.1.1	Principles of neutron scattering	88
7.1.2	Scattering functions	91
7.1.3	The incoherent contribution	92
7.1.4	Characterization of hydration water dynamics	94
7.1.5	The Time-of-Flight spectrometer: TOFTOF at FRM-II	94
7.2	A model for water dynamics in perdeuterated tau protein	95
7.2.1	Spectra normalization	97
7.2.2	DTAU-H ₂ O temperature dependence	100
7.2.3	Discussion and perspective	105
	Conclusions	107
	References	110
	Acknowledgments	128

Abstract

Studi biofisici realizzati a temperature criogeniche permettono di investigare proprietà dinamiche, cinetiche e strutturali di biosistemi che, sebbene presenti, sarebbero di difficile risoluzione a temperature più alte. Queste proprietà hanno rilevanza in molti processi fisiologici che influenzano la funzionalità biologica di macromolecole. I metodi di spettroscopia di risonanza paramagnetica di spin (EPR) sia in onda continua (cw-EPR) che in regime pulsato (FT-EPR) sono particolarmente efficienti per la caratterizzazione di aggregati sopramolecolari nello stato congelato. In questo lavoro sono presentati e discussi esperimenti di cw- e FT-EPR a 9 GHz condotti su diversi biosistemi spin-labellati (membrane lipidiche a doppio strato, fasi lamellari interdigitate, micelle, membrane naturali e proteine) nelle fasi a bassa temperatura. È dato particolare risalto allo studio delle proprietà dell'acqua di idratazione entro una distanza di 0.5 nm dai radicali nitrossidi, alla caratterizzazione della dinamica a bassa temperatura dei biosistemi e come le condizioni di idratazione influenzino le proprietà dei biosistemi a bassa temperatura. Sono anche inclusi i risultati ottenuti dall'analisi di dati di scattering di neutroni per investigare la dinamica dell'acqua di idratazione nella proteina tau umana, una proteina intrinsecamente disordinata coinvolta nell'insorgere di patologie neurodegenerative come la malattia di Alzheimer.

Esperimenti a tre impulsi di modulazione dell'eco di spin elettronico dall'interazione iperfine con deuterio (D_2O -ESEEM) ed esperimenti di cw-EPR sono stati combinati a $T = 77$ K per caratterizzare il grado di permeazione dell'acqua e la polarità dell'ambiente, rispettivamente, nella shell di idratazione più prossima di aggregati lipidici spin-labellati selettivamente. È stato studiato il comportamento di fase litotropico di miscele a completa idratazione di lipidi formanti doppi strati (*bilayers*) di dipalmitoilfosfatidilcolina (DPPC) con lipidi formanti micelle di dipalmi-

toilfosfatidiletanolamina (DPPE) derivati sulla testa polare con poli-etilene glicole di peso molecolare 2000 Da (PEG:2000-DPPE) o di Liso-palmitoilfosfatidilcolina (Lyso-PPC), studiando l'intero range di composizione (concentrazioni tra 0 e 100 mol%). Sono stati delineati i profili transmembranal di accessibilità del solvente e di polarità in liposomi stabilizzati stericamente (SSL), formati da miscele di DPPC e 2 mol% di PEG:2000-DPPE, e in micelle di polimero-lipidi. Questi profili sono stati confrontati con quelli registrati per lipidi organizzati in bilayer e in lamelle con catene interdigitate e per micelle di lipidi a singola catena. Inoltre, misure di D₂O-ESEEM e cw-EPR condotte su steroidi cardiotonici spin-labellati nella pompa sodio-potassio Na⁺,K⁺-ATPase hanno mostrato che il vestibolo che conduce ai siti di legame di steroidi e cationi è relativamente ampio e ricco di acqua.

Sono stati, poi, combinati spettri cw-EPR e spettri rilevati tramite echo in esperimenti a due impulsi (spettri ED) per caratterizzare la dinamica di campioni spin-labellati nello stato congelato nel range di temperatura tra 77 K e 270 K. In tutti i sistemi modello di membrana analizzati in questo lavoro, costituiti da lipidi con catene sature o insature o con catene interdigitate, si manifestano moti librazionali di piccola ampiezza angolare ($< 20^\circ$) che avvengono sulla scala dei nanosecondi. Tutti i campioni studiati hanno mostrato un comportamento simile nella dipendenza in temperatura dell'ampiezza angolare librazionale, manifestando un rapido incremento in corrispondenza della transizione dinamica che avviene ad una temperatura, T_d , di circa 200 - 220 K. La transizione è associata all'attivazione di moti stocastici di maggiore ampiezza che fanno sì che i bilayers superino una barriera energetica con energia di attivazione $E_a \approx 15 - 30$ kJ/mol.

La prima shell di acqua di idratazione che circonda le macromolecole è fondamentale per l'attivazione della loro funzionalità biologica. È stata, pertanto, caratterizzata l'influenza dell'idratazione sulla dinamica nello stato congelato di due proteine con diversa struttura secondaria, cioè α per l'albumina del siero umano e β per la β -lattoglobulina, e del più comune sistema modello di membrana lipidica costituito da DPPC. Mentre la dinamica delle proteine è inibita nello stato liofilizzato per attivarsi progressivamente in presenza di molecole di acqua, nel caso della membrana lipidica le librations di ampiezza significativa si registrano nella regione idrofobica interna del bilayer anche in assenza di acqua.

Infine, è presentato uno studio della dinamica traslazionale e rotazionale dell'acqua di idratazione della proteina tau perdeuterata attraverso l'analisi di dati di scattering di neutroni quasi-elastico, raccolti allo spettrometro TOF/TOF alla sorgente di neutroni Heinz Maier-Leibnitz.

Abstract

Biophysical studies at cryogenic temperatures allow us to unravel dynamic, kinetic, and structural features of biosystems that are present also at higher temperatures but difficult to resolve explicitly. These properties impact on functionally important processes of physiological relevance in biological media. Methods of electron paramagnetic resonance (EPR) spectroscopy, both in continuous wave (cw-EPR) and in pulsed, Fourier transform version (FT-EPR), are appropriate to characterize supramolecular aggregates in the frozen state. In this work, results from 9 GHz cw- and FT-EPR investigations on differing spin-labelled biosystems (such as lipid bilayers, interdigitated lamellae, micelles, natural membranes and proteins) in the low-temperature phases are presented and discussed. Emphasis is given to investigate the properties of hydration water within 0.5 nm from the spin-label nitroxide moieties, to characterize the low-temperature dynamics of the different biosamples, and to highlight the influence of hydration conditions on the low-temperature properties of the biosystems. Analysis of neutron scattering data on the intrinsically disordered human tau-protein to investigate the hydration water motion is also included.

Three-pulse electron spin echo envelope modulation from ^2H -hyperfine interaction with deuterium (D_2O -ESEEM) and cw-EPR are jointly employed at 77 K to detect the extent of solvent permeation and the environmental polarity, respectively, in the nearest hydration shell of site-specifically spin-labelled self-assembled lipid aggregates. The lyotropic phase behaviors of fully hydrated mixtures of the bilayer forming lipid dipalmitoylphosphatidylcholine (DPPC) with either the micelle-forming lipid poly(ethylene glycol:2000)-phosphatidylethanolamine (PEG:2000-DPPE) or Lyso-palmitoylphosphatidylcholine (Lyso-PPC) are investigated over the entire composition range (0 – 100 mol%). The transmembrane water accessibility and polarity

profiles of sterically stabilized liposomes (SSL), formed by admixture of DPPC and 2 mol% of PEG:2000-DPPE, and of polymer-lipid micelles have been delineated. They are compared to those of lipid bilayers and lamellae with interdigitated chains and those of small, single-chain micelles. Additionally, D₂O-ESEEM and cw-EPR measurements of spin-labelled cardiotonic steroids in Na⁺,K⁺-ATPase revealed that the vestibule leading to steroid-binding and cation binding sites is relatively wide and water-filled.

Cw-EPR and two-pulse echo detected ED-spectra are used to characterize the dynamics of spin-labeled samples in the frozen state over the temperature range 77 – 270 K. Rapid librations (in the nanosecond timescale) of small angular amplitude (< 20°) manifest themselves in all the model membranes of saturated or unsaturated lipids or with interdigitated chains studied in this work. A feature shared by the investigated samples is that the temperature dependences of the segmental librational amplitudes show a rapid increase at the dynamical transition occurring at $T_d \approx 200 - 220$ K. The transition is associated with the onset of stochastic motions with the bilayers crossing low-energy barriers of activation energy $E_a \approx 15 - 30$ kJ/mol.

The hydration water surrounding macromolecules is fundamental in the activation of their biological functionality. The effects of hydration on the dynamics of proteins of different structures, namely α for Human Serum Albumin and β for β -Lactoglobulin, and model membranes of the most common lipid DPPC in cell membrane in the low-temperature phases have been also addressed. While the protein dynamics is suppressed in the lyophilized state and is progressively activated in the presence of water molecules, it is found that segmental librations of considerable amplitudes are detected in the inner membrane hydrocarbon region even in the dry state.

Finally, results on the analysis of quasi-elastic neutron scattering data collected at the Time-Of-Flight spectrometer TOFTOF of the research neutron source Heinz Maier-Leibnitz on perdeuterated human tau protein are presented, in order to describe the translational and rotational dynamics of hydration water molecules.

CHAPTER 1

Introduction

Nowadays, biophysical studies of macromolecules and supramolecular assemblies are routinely carried out at low (samples cooled with nitrogen down to 77 K) and very low (samples cooled with helium below 77 K) cryogenic temperatures by using high-resolution spectroscopic techniques that operate on different time, space and energy scales [1–4]. By suppressing the molecular tumbling and the conformational exchange and by trapping (by rapid freeze quenching) transient intermediate states in non-equilibrium kinetic processes, low-temperature studies allow to unravel structural, dynamic and kinetic features of biosystems that are inevitably present but not explicitly detectable at higher physiological temperatures. As such, they play an important role in elucidating the molecular mechanisms underlying the structure/dynamics/function relationships in biosystems. Moreover, biological media are intensively investigated at cryogenic temperatures in several fields of applied research because of the relevance to (cryo)preservation and (bio)protection of cells, tissues, therapeutic proteins, vaccines and food [5–9].

Among the other spectroscopic techniques, such as X-ray and neutron crystallography, cryo-transmission electron microscopy, solid state nuclear magnetic resonance, Raman and infrared spectroscopy, methods of electron paramagnetic resonance (EPR) spectroscopy, both in continuous wave (cw-EPR) and in pulsed, Fourier Transform (FT-EPR) version and at different operating frequency, represent efficient tools to investigate frozen spin-labeled biosystems [10–14]. By using conventional EPR and spin-echo methods of FT-EPR at 9 GHz, relevant properties have been addressed in spin-labeled biomembranes and proteins in the low-temperature phases (see, i.e., [15]). These include the solvent penetration at specific region around the

spin-label site, the transmembrane polarity profiles as revealed by polarity-sensitive spin-label EPR parameters, the segmental librational dynamics, and the heterogeneity of protein substates [16–22].

The properties of water within 0.5 nm from the spin-label nitroxide moiety in fully hydrated samples are readily detected by three-pulse electron spin echo envelope modulation by deuterium (D₂O-ESEEM) at 77 K. By using this pulsed technique, it is possible to reveal the direct accessibility of the solvent around the spin-label site, to distinguish and resolve the component due to solvent molecules hydrogen-bonded to the nitroxides from that due to unbound, more distant deuterons, as well as to determine the fractions of spin-labels singly and doubly hydrogen-bonded to the solvent molecules (see, i.e., [17, 23]). These results have important general implications for the binding of water to H-bond acceptors and donors within the membrane; for instance, water H-bonded at the intramembranous surface of integral proteins could potentiate the diffusive water permeation pathway through membrane [24]. Moreover, it has been reported that bound hydration water has a dynamics slower than both unbound hydration water and bulk water [25]. Therefore, the D₂O-ESEEM results could also be relevant in relation to the slowdown of biological activity upon dehydration. The interaction of water with macromolecules, as well as the direct solvent accessibility at specific regions in macromolecules, are fundamental to transport studies and to the formation and stability of biological membranes. Further, the penetration of water into lipid membranes and the resultant transmembrane polarity profiles delineated in D₂O-ESEEM studies of chain-labelled lipids have direct relevance for the permeability across biological membranes and for the energetic of the insertion of proteins, peptides, and amphiphiles into the membrane.

Two-pulse, partially relaxed echo detected ED-EPR spectra and cw-EPR spectra acquired in nitroxide-labelled samples in the temperature interval 77 - 270 K are indicative of isotropic librational motion. This consists of rapid torsional oscillations in the nanosecond timescale of small angular amplitude occurring simultaneously and independently around the three perpendicular molecular nitroxide axes [16, 26–28]. From the pulse and conventional EPR measurements, the librational motion can be fully characterized via the evaluation of the motional parameter, $\langle\alpha^2\rangle\tau_c$, the mean-square angular amplitude, $\langle\alpha^2\rangle$, and the correlation time, τ_c , of the librations. High frequency librations are an important feature of the rotational dynamics of biosystems at low, cryogenic temperatures. Stochastic librations explicitly detected in biosystems at low temperatures are also present at higher temperatures hidden by rotational motions of large amplitude. These motions are involved in functionally important processes at physiological temperatures; for instance, they can contribute

to pathways between the different conformational substates in proteins and may be involved in ion conduction within hydrophobic peptide channels in lipid membranes; also, fluctuations in the lipid environment can drive solvent-mediated transitions in membrane proteins [29–32]. Librations are also important for the survival upon cryopreservation of tissues, cells and genetic materials [6, 33].

A remarkable feature of the biosystem dynamics at cryogenic temperatures observed by EPR is that the temperature dependence of the mean-square librational amplitude, $\langle\alpha^2\rangle$, starts to increase very rapidly for temperatures around 200 K [26, 32–41]. This behavior is rather similar to the temperature dependence of the mean-square atomic displacement, $\langle r^2\rangle$, measured in membranes and proteins from diffraction studies [29, 42–52]. The temperature at which the sharp rise occurs in both $\langle\alpha^2\rangle$ and $\langle r^2\rangle$ is identified with the temperature, T_d , of the so called dynamical transition, which has been associated with the onset of stochastic, diffusive motions and the crossing of low energy barriers of about 20 kJ/mol [29, 39, 41, 53, 54]. The dynamical transition is detected not only in fully hydrated biological media and supramolecular aggregates but also in non-biological aqueous environments [55]. Hydration water influences the stability and function of biomolecules [56–60]. It is reported that the low-temperature dynamics and the dynamical transition are affected by the hydration level of the samples. Protein dynamics is suppressed in the absence of water and is activated by hydration water molecules, which drive the onset of stochastic oscillations of augmented amplitude at the dynamical transition [35, 44, 59, 61]. On the other hand, the influence of the hydrating conditions in lipid membrane librations is currently debated in the literature [25, 52, 62, 63], so that more accurate investigations are needed.

In this thesis, we use D₂O-ESEEM and ED-EPR spectra combined with conventional cw-EPR to investigate biophysical properties of the low-temperature phases of differing spin-labelled biosystems, usually studied at higher physiological temperatures. We aim at advancing the molecular characterization of membrane model systems consisting of either single specie lipids or binary lipid mixtures, lamellar lipid assemblies with interdigitated chains, micelles, soluble proteins, and natural membranes. Emphasis is given to the properties of hydration water and to the solvent penetration at selected sites within biosystems, to the librational motion and the dynamical transition and their dependence on the hydration level, and to the study of the water hydration dynamics.

Spin-label D₂O-ESEEM in fully hydrated biosystems at 77 K is used (*i*) to study the lyotropic phase behavior of mixtures of bilayer-forming lipids and micelle-forming lipids over the entire composition range (0 - 100 mol%); (*ii*) to delineate the transmembrane water accessibility and polarity profiles of sterically stabilized

liposomes, interdigitated lamellar phases and micellar phases; (*iii*) to characterize the interaction of spin-labelled cardiotoxic steroids (CTS, cardiac glycosides) with the sodium pump Na^+, K^+ -ATPase, which is the primary pharmacological receptor for CTS.

For issues (*i*) and (*ii*), as bilayer-forming lipids we use diacyl phosphatidylcholines (PCs) because of their large abundance in the cell membrane of eukaryotes and bacteria [64]. In particular, bilayers composed of dipalmitoylphosphatidylcholine (DPPC) lipids are widely used for cell membrane model systems and represent appropriate matrices in which other types of lipids can be incorporated [65]. Among them, polymer-lipids of diacyl glycerophosphatidylethanolamines (PEs), with poly(ethylene-glycol) polymers (PEGs) of different molecular weight covalently attached at the polar head (PEGs-PEs), find extensive application as biocompatible coating. PEGylated phospholipid aggregates capture the interest in basic research and in biotechnological applications as efficient drug carriers and smart soft materials [66–68]. In particular, mixtures of PCs and appropriate amount of PEGs-PEs polymer-lipids form sterically stabilized liposomes (SSL), also known as Stealth or long-circulating liposomes, that are suitable vehicles for drug encapsulation and delivery [65, 69]. Because of the bulky hydrophilic polymer head groups, PEGs-PEs molecules retain a wedge shape and, at full hydration in water, self-assemble in micelles. PEGs-PEs micelles are promising nanoparticles for drug carriers [70].

Another example of interesting lipids well compatible with the host DPPC matrix are the single-chain micelle-forming Lyso-phosphatidylcholines (Lyso-PCs). Lyso-PCs are found in small amounts in mammalian cell membranes and in various membranes of subcellular organelles, where they play a key role in cellular, physiological and pathological processes [71–73]. As a function of their concentration in the host model membrane, Lyso-PCs affect the order and the structure of the acyl chains as well as the permeability of lipid vesicles [74–80]. At low content, Lyso-lipids are essential components of PC-based thermosensitive liposomes used in drug delivery [81, 82]; at intermediate content (30 - 50 mol%), Lyso-lipids in bilayers of DPPC induces the formation of an interdigitated gel phase [77, 83]. Chain interdigitation can be achieved in DPPC bilayers also with other external inducers such as glycerol, ethylene glycol, short-chain alcohols and chaotropic salts [84].

In this thesis, bilayer-to-micelle phase transformation and the formation of intermediate lipid phases which occur on adding increasing content of either PEG-lipids or Lyso-lipids in DPPC are readily identified from the dependence of the spin-label D_2O -ESEEM signal on the type of lipid aggregate and on the position of labeling. Moreover, the pulsed EPR method, combined with the use of spin-labelled lipids bearing the nitroxide $-\text{NO}$ doxyl ring stereospecifically attached to a C_n atom po-

sition along the *sn*-2 chain, from the polar/apolar interface toward the terminal methyl end (*n*-PCSL, $n = 4, 5, 7, 8, 9, 10, 11, 12, 14, 16$), allows us to investigate the structural heterogeneity and the H-bond propensity of the solvent as well as to delineate at high spatial resolution the water penetration profile and the hydrophobic barriers in a variety of interesting lipids aggregates (SSL, interdigitated lamellar phases, polymer-lipids and Lyso-lipid micelles) never studied before with spectroscopic techniques at cryogenic temperatures. The results are relevant for the interaction of biomacromolecules (peptides and proteins) with surface-functionalized, PEG-grafted lipid aggregates and for the interaction (binding, encapsulation, transport and release) of hydrophobic ligands and active compounds with smart drug-carriers. Moreover, the characterization of interdigitated phases at cryogenic temperature is of biological and biophysical interest because any molecule affecting the structure, the dynamics and the molecular properties of model membranes may influence specific membrane functions. In particular, surface-active molecules and lipids may also have an effect at the water-lipid interface in biomembranes.

The issue (*iii*) is of high biomedical impact. Indeed, for their ability to inhibit Na^+, K^+ -ATPase, cardiotonic steroids are useful in the treatment of heart failure and bufadienolides (i.e., specific CTS subgroup) show significant pharmacological activity against certain types of cancer. The interaction of spin-labelled bufadienolides, namely bufalins and cinobufagins of different length, with Na^+, K^+ -ATPase membranes is explored by D_2O -ESEEM and conventional EPR at 77 K to define the geometry and the water accessibility of the binding channel of the sodium pump. The binding site of CTS overlaps with the extracellular access channel for the cations of the Na^+, K^+ -ATPase, so that the EPR-based experiments at cryogenic temperature are the first step for future studies of possible conformational changes of this fundamental functional site of the enzyme.

Another topic addressed in this thesis is the librational dynamics and the related dynamical transition in membrane model systems in the frozen state. By using echo detected ED-spectra and cw-EPR spectra in the temperature interval 77 – 270 K, the segmental librational motion and the dynamical transition in saturated and unsaturated lipid lamellae and in interdigitated lamellar phases are investigated. We compare the dynamical properties of low- T_m (i.e., low value of the main phase transition temperature, T_m , to the fluid state) unsaturated DOPC and POPC bilayers and of high- T_m saturated DPPC (ca. 253 K and ca. 271 K vs 314 K) [85]. Low- T_m bilayers are in the fluid phase over a broad temperature range of biological relevance, they impart fluidity to membranes and impact on membrane thickness. For these properties they have been used as model systems to study lipid–protein or lipid–peptide interaction, domain formation in membranes, and nanometer-scale

surface properties at high temperatures [64, 86, 87]. We aim at investigating the lipid interactions and the dynamical properties at cryogenic temperatures and to compare the dynamical behavior around 200 K in low- T_m unsaturated bilayers vs high- T_m saturated bilayers.

Particular attention is also given to the role of the solvent on modulating the dynamics of biosamples. It is known that solvent controls protein dynamics and affects macromolecule activity [29, 35, 49]. Since the seminal work of Frauenfelder and coworkers [29, 49, 88, 89], the impact of the hydration on the dynamics of macromolecular systems is a well-accepted fact. The effects of the hydration level on the librational dynamics in soluble proteins of different structure, shape and size as well as in DPPC model membranes (prepared at full hydration, low hydration and in the dry state) are investigated, with specific focus to the dependence of the dynamical transition on the hydrating conditions. Two proteins, the α -structured multidomains Human Serum Albumin (HSA, 66 kDa) and the β -structured β -Lactoglobulin (β -LG, 18 kDa), are studied in the lyophilized state, at low and high hydration. HSA is the principal extracellular protein with a high concentration in blood plasma where it performs different functions, such as binding, storing and transporting of a wide variety of exogenous and endogenous molecules, drugs and metals [90]. β -LG is the most abundant protein in the milk of different mammals, not including humans, and it is involved in the binding and transport of hydrophobic and amphiphilic molecules. The rapid, small-amplitude angular oscillations detected in the proteins and lipid lamellae in the present study may be relevant in regulating their physical properties and function at higher physiological temperatures. The detailed characterization of stochastic librations and the detection of the dynamical transition will contribute to understand whether the low-temperature behavior is common to all hydrated macromolecular systems, and to highlight similarities and differences among the various samples at different water content.

Coupling is suggested between hydration water dynamics and macromolecules dynamics [25, 61, 91–94]. Within this context, in the last chapter of the thesis, neutron scattering data on perdeuterated protein samples are analyzed, focusing the attention on the dynamics of the hydration water. Neutron scattering is particularly appropriate to study the dynamics of biomacromolecules and of the hydration water on the picoseconds to nanoseconds time scale. The technique has revealed that the onset of functionally relevant dynamics observed in proteins around the dynamical transition at ca. 220 - 240 K is closely related to the dynamics of hydration water [47, 92, 93]. Results on the analysis of quasi-elastic neutron scattering data collected at the Time-Of-Flight spectrometer TOFTOF of the research neutron source Heinz Maier-Leibnitz on perdeuterated human tau protein are presented, in order

to describe the translational and rotational dynamics of hydration water molecules. Human tau protein is an intrinsically disordered protein involved in cellular signaling, neuronal development, neuroprotection and apoptosis. Hyperphosphorylated insoluble aggregates of Tau protein are known to be responsible of the occurrence of neurodegenerative pathologies, such as Alzheimer's disease.

In this doctoral thesis on cryobiophysics, by applying EPR experimental methods and by analyzing quasi-elastic neutron scattering data, we investigate specific structural, dynamic and molecular properties of the low-temperature phases of biosystems that would otherwise be of difficult or even of impossible resolution at higher temperatures. The results at cryogenic temperatures contribute to expand the biophysical characterization of samples at an unprecedented level of detail. The thesis is structured in chapters: after a comprehensive illustration of the electron spin resonance theory of nitroxide spin-labels (including cw-EPR, D₂O-ESEEM and ED-spectra; Chapter 2) and the description of the used materials and the applied methods (Chapter 3), the results on the addressed issues are presented and discussed in Chapters from 4 to 7. They concern water penetration in biosystems (Chapter 4), dynamics of lipid assemblies at cryogenic temperatures (Chapter 5), role of hydration water in the dynamical properties of proteins and lipid membranes (Chapter 6), and hydration water dynamics in tau protein from neutron scattering data analysis (Chapter 7). Some of the results presented in this thesis are already published in research journals, while some others will be published soon.

Electron Paramagnetic Resonance

2.1 A short history of EPR

Electron paramagnetic resonance (EPR) or electron spin resonance (ESR) is a spectroscopic technique for unraveling structure, dynamics and chemical processes of free radicals and paramagnetic species. In 1944 at Kazan State University in Russia, scientist E.K. Zavoisky performed the first EPR experiment at a frequency of 133 MHz and in 1946 the first microwave EPR experiment. Then, in 1958, the basis of pulse EPR were set when different scientists simultaneously observed electron spin echoes [95,96]. In the 1960s pioneering work on pulse EPR was made by Mims group at the Bell laboratories, where for the first time a modulation of the echo amplitude because of the electron-nuclear dipole interaction was observed, and by Tsvetkov group in Novosibirsk, where the first echo modulation experiment on a disordered system was performed [97]. EPR has been applied over the years and is applied nowadays in chemistry, biology and physics and has proved useful in archaeology and geology for dating materials and for radiation measurements. A great advantage in the application of the technique is reached adding some paramagnetic probes to the samples. Among them, nitroxides are stable free radicals particularly useful for labelling macromolecules, addressing both their structural and dynamical properties. The first synthesized spin-labels were produced in 1965 in H.M. McConnell's laboratory, where bovin serum albumin and poly-L-lisine were site-directed spin-labelled with a nitroxide label synthesized from triacetoneamine [98], setting the start for site-directed spin-labeling technique for the local investigation of proteins and biomolecules properties.

2.2 The EPR phenomenon

2.2.1 Zeeman interaction

Electron paramagnetic resonance is a spectroscopic technique that detects the absorption of microwave electromagnetic radiation by a paramagnetic system located in a static magnetic field. The technique involves spin transitions among the Zeeman levels of the system, created by the external magnetic field. The electron Zeeman interaction of the magnetic moment $\boldsymbol{\mu}$ of an electron (spin operator \mathbf{S} with components m_s) with an external magnetic field \mathbf{H} ($\mathbf{H} = (0, 0, H_0)$) in the laboratory axis system (x, y, z) is represented by the following spin Hamiltonian \mathcal{H} :

$$\mathcal{H}_Z = -\boldsymbol{\mu} \cdot \mathbf{H} = \beta_e \mathbf{H} \cdot \mathbf{g} \cdot \mathbf{S} \quad (2.1)$$

where β_e is the Bohr magneton for an electron and \mathbf{g} is a second-rank tensor [11].

Analogously, the nuclear Zeeman interaction, arising from the coupling of a nuclear spin \mathbf{I} to the external field \mathbf{H} , is:

$$\mathcal{H}_{nZ} = -g_n \beta_n \mathbf{H} \cdot \mathbf{I} \quad (2.2)$$

where g_n and β_n are the g -factor and the Bohr magneton for a nucleus, respectively. In most EPR experiments the nuclear Zeeman interaction contribution is negligible compared to the electron one [12].

For a spin system with $\mathbf{S} = 1/2$ and $m_s = \pm 1/2$, the energy separation, ΔE , between the two Zeeman levels is:

$$\Delta E = g_e \beta_e H_0 \quad (2.3)$$

with g_e the g -factor for a free electron (see left side of figure 2.1).

Resonant transitions between the Zeeman levels are induced by a perturbative electromagnetic radiation oscillating in the x direction perpendicular to \mathbf{H} , of amplitude $H_1 \ll H_0$ and frequency ν . The excitation of the electronic state by this continuous radiation allows to perform a conventional or continuous wave electron spin resonance (cw-EPR) experiment.

The probability of transition, W , per unit time, according to the Fermi's golden rule, is:

$$W = \frac{2\pi}{\hbar} g_e^2 \beta_e^2 H_1^2 \left| \left\langle \frac{1}{2} | \mathbf{S}_x | -\frac{1}{2} \right\rangle \right|^2 \delta(\Delta E - h\nu) \quad (2.4)$$

Thus, transition is allowed if the selection rule $\Delta m_s = \pm 1$ and the resonance condi-

tion:

$$h\nu = \Delta E = g_e\beta_e H_0 \quad (2.5)$$

are satisfied. Considering a magnetic field of 330 mT, the operating frequency is 9 GHz, the so-called X-band. In an X-band cw-EPR experiment is more convenient to keep the frequency constant and satisfy resonance by sweeping the magnetic field.

The population distribution in the Zeeman levels follows the Boltzmann law:

$$\frac{n_{|1/2\rangle}}{n_{|-1/2\rangle}} = \exp\left(-\frac{\Delta E}{kT}\right) \quad (2.6)$$

where n_i is the population of the i th level, ΔE is the energy separation between the Zeeman levels, k is the Boltzmann constant and T is the temperature. For X-band EPR, $\Delta E \approx 0.3 \text{ cm}^{-1}$ is much smaller than $kT \approx 200 \text{ cm}^{-1}$, therefore there is a small population difference, with the lower level slightly more populated than the upper one. As the stimulated transitions have the same probability to occur in both directions, at the resonance a net (small) absorption of microwave radiation is detected. The maximum of absorption is centered for the g -value that fulfills resonance. To improve the signal-to-noise ratio in a cw-EPR experiment, a magnetic field modulation of small amplitude and at the frequency of 100 kHz is used together with phase sensitive detection. As a consequence, the absorption spectra are typically presented as the first derivative (figure 2.1). The first derivative line-shape is an approximation valid when the modulation amplitude is smaller than the line width. Such a single-line spectrum is recorded for isolated free radicals and when magnetic interactions other than the electron Zeeman interaction can be neglected.

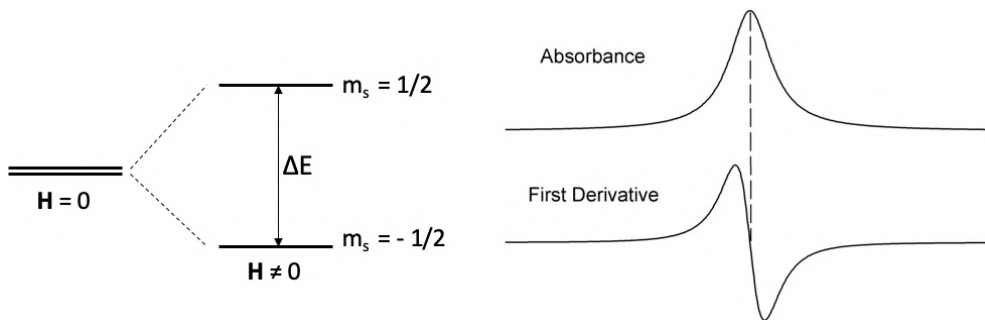


Figure 2.1: *Left:* Zeeman splitting for a spin $\mathbf{S} = \frac{1}{2}$ system. *Right:* Absorbance and corresponding first derivative spectra for a spin $\mathbf{S} = \frac{1}{2}$ system.

While the system absorbs the energy from the perturbative electromagnetic field,

the inverse process of stimulated emission occurs, the small population difference disappears and the system approaches saturation. Saturation is avoided because the Boltzmann population distribution is restored through two relaxation processes. The first one is the *spin-lattice* or *longitudinal relaxation time*, T_1 , on the microseconds time scale, which corresponds to the nonradiative thermal energy loss. The second one is the *spin-spin* or *transverse relaxation time*, T_2 , on the nanoseconds time scale, which is a magnetic interaction modulating the energy of the excited state (affecting the Zeeman levels). It influences the broadening of the absorbance spectral linewidths.

2.2.2 Hyperfine interaction

The electron spin, \mathbf{S} , of the unpaired electron of the paramagnetic species interacts with the nuclear spin, \mathbf{I} , of the atom to which the electron belongs, giving rise to the hyperfine interaction. The hyperfine interaction can be described by the following Hamiltonian [11]:

$$\mathcal{H}_{hf} = -g_e\beta_e g_n\beta_n \left[\frac{(\mathbf{I} \cdot \mathbf{S})}{r^3} - \frac{3(\mathbf{I} \cdot \mathbf{r})(\mathbf{S} \cdot \mathbf{r})}{r^5} - \frac{8\pi}{3}(\mathbf{I} \cdot \mathbf{S}) |\psi_0(0)|^2 \right] \quad (2.7)$$

with \mathbf{r} the distance between the electron and the nuclear spin.

The first two terms of equation (2.7) represents the electron-nuclear dipolar interaction, while the third term, i.e., the Fermi contact interaction, accounts for the electron probability distribution $|\psi_0(0)|^2$ at the nucleus. The equation (2.7) can be written in the compact form:

$$\mathcal{H}_{hf} = \mathbf{I} \cdot \mathbf{A} \cdot \mathbf{S} \quad (2.8)$$

where \mathbf{A} is the hyperfine tensor, which is, like \mathbf{g} , a second-rank tensor. Thus, the spin Hamiltonian is [11]:

$$\mathcal{H} = H_Z + H_{hf} = \beta_e \mathbf{H} \cdot \mathbf{g} \cdot \mathbf{S} + \mathbf{I} \cdot \mathbf{A} \cdot \mathbf{S} \quad (2.9)$$

2.2.3 The nitroxide spin labels

For samples of biophysical or biological interest that are not paramagnetic, it is necessary to introduce a spin probe/spin-label that allows to detect the EPR signal. Widely used are nitroxides -NO ($\mathbf{S} = 1/2$, $\mathbf{I} = 1$), stable free radicals in which the unpaired electron possible reactions are prevented by the presence of four methyl groups.

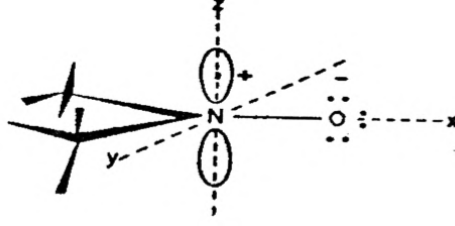


Figure 2.2: Nitroxide radical and associated molecular axis system (X, Y, Z) [99].

In the nitroxide molecular axis system (X, Y, Z) (figure 2.2), the tensor \mathbf{g} and the hyperfine tensor \mathbf{A} are diagonal:

$$\mathbf{g} = \begin{pmatrix} g_{XX} & 0 & 0 \\ 0 & g_{YY} & 0 \\ 0 & 0 & g_{ZZ} \end{pmatrix} \quad \mathbf{A} = \begin{pmatrix} A_{XX} & 0 & 0 \\ 0 & A_{YY} & 0 \\ 0 & 0 & A_{ZZ} \end{pmatrix}$$

At 9 GHz, the hyperfine tensor is axial: $A_{\perp} \simeq A_{XX} \simeq A_{YY} \simeq 0.6 \text{ mT} \ll A_{ZZ} = A_{\parallel} \simeq 3.2 \text{ mT}$; the tensor \mathbf{g} shows little anisotropy: $g_{XX} > g_{YY} > g_{ZZ}$. The Hamiltonian of equation (2.9) can be written in the following extended form:

$$\begin{aligned} \mathcal{H} = & \beta_e (g_{XX} H_X S_X + g_{YY} H_Y S_Y + g_{ZZ} H_Z S_Z) \\ & + A_{XX} I_X S_X + A_{YY} I_Y S_Y + A_{ZZ} I_Z S_Z \end{aligned} \quad (2.10)$$

The transitions allowed for a nitroxide radicals are $2S(2I + 1) = 3$, according to the selection rules $\Delta m_S = \pm 1$, $\Delta m_I = 0$ (figure 2.3).

In the case of immobilized free radicals in the rigid limit motion, at low temperature or in high viscous medium, a powder spectrum can be observed, where the hyperfine splitting $2\langle A_{ZZ} \rangle$ can be evaluated as the outer separation between the maximum of the low-field resonance line and the minimum of the high-field resonance line. The EPR spectral parameter A_{ZZ} reflects environmental polarity and proticity around the spin-label via the dependence on the net unpaired electron spin density on the nitroxide $-\text{NO}$ reporter group [14,100]. It is measured from the spectra at low temperature (i.e., 77 K) when motional contributions are negligible.

In the case of radicals in the fast motion regime, at high temperature and non viscous media, the angular dependence in the Hamiltonian is averaged out and the nitroxide spectrum is isotropic, with three equally intense and equally spaced resonance lines. The isotropic \mathbf{g} -value $g_0 = 1/3(g_{xx} + g_{yy} + g_{zz})$ and the isotropic hyperfine splitting $A_0 = 1/3(A_{xx} + A_{yy} + A_{zz})$ can be evaluated. In axial symmetry $g_0 = 1/3(2g_{\perp} + g_{\parallel})$ and $A_0 = 1/3(2A_{\perp} + A_{\parallel})$.

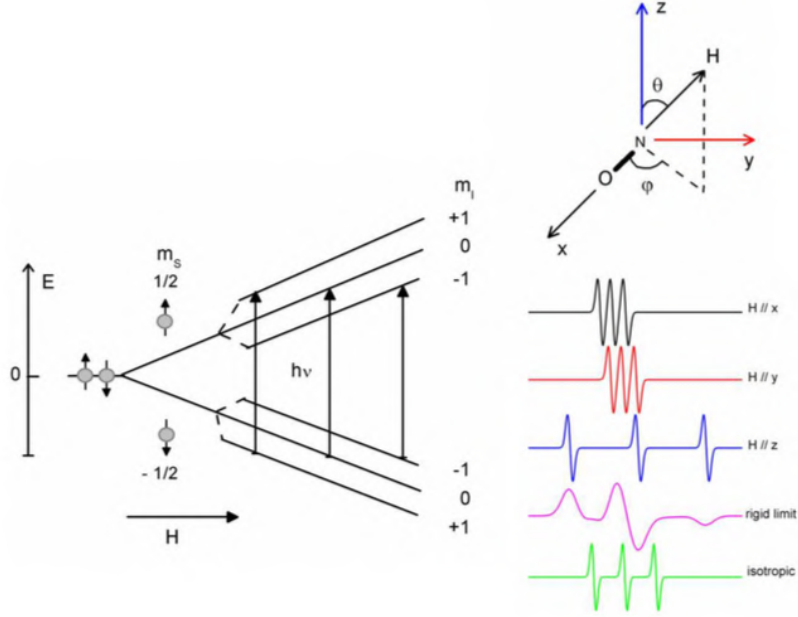


Figure 2.3: *Left:* energy levels and transitions allowed for a nitroxide spin label. *Right:* (*up*) nitroxide molecular axis system and (*down*) simulated nitroxide spectra with the magnetic field oriented along each of the molecular axis X, Y, Z . An anisotropic spectrum in the rigid limit of motion and an isotropic one in the fast motion regime are also shown.

Considering a generic orientation (θ, φ) of the magnetic field with respect to molecular axis Z , the allowed transitions are:

$$h\nu = \beta_e g(\theta, \varphi) H_{m_I}^{(\theta, \varphi)} + A(\theta, \varphi) m_I \quad (2.11)$$

where

$$\begin{aligned} g(\theta, \varphi) &= (g_{XX} \cos^2 \varphi + g_{YY} \sin^2 \varphi) \sin^2 \theta + g_{ZZ} \cos^2 \theta \\ A(\theta, \varphi) &= [(A_{XX}^2 \cos^2 \varphi + A_{YY}^2 \sin^2 \varphi) \sin^2 \theta + A_{ZZ}^2 \cos^2 \theta]^{1/2} \end{aligned} \quad (2.12)$$

and in the axial symmetry:

$$\begin{aligned} g(\theta) &= g_{\perp} \sin^2 \theta + g_{\parallel} \cos^2 \theta \\ A(\theta) &= (A_{\perp}^2 \sin^2 \theta + A_{\parallel}^2 \cos^2 \theta)^{1/2} \end{aligned} \quad (2.13)$$

with θ being the angle between the Z axis and the magnetic field [14].

2.2.4 Librational motion from cw-EPR

At cryogenic temperatures, as in the case of cooling samples in liquid nitrogen (77 K), the nitroxide spin-labels dynamics is librational [101]. The librational motion (figure 2.4) consists of rapid oscillations, in the nanosecond time scale, of small angular amplitude ($< 20^\circ$) around an equilibrium position.

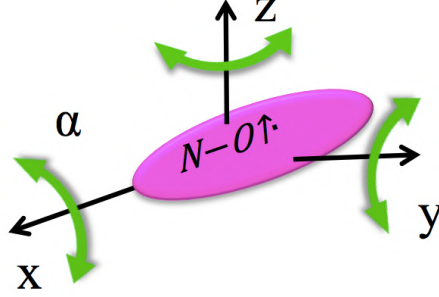


Figure 2.4: Librational angle, α , of the nitroxide group around the three principal axes.

Considering, as an example, small oscillations around the Y molecular axis, the outer hyperfine separation $2\langle A_{ZZ} \rangle$ depends on the X and Z component of the hyperfine tensor \mathbf{A} [26, 101]:

$$\langle A_{ZZ} \rangle = A_{ZZ} - (A_{ZZ} - A_{XX}) \langle \sin^2 \alpha \rangle \quad (2.14)$$

with α the angle determining the radical orientation with respect to the equilibrium position along the motional axes. Analogous equations can be written down considering motion around the other principal axes by permutation of X, Y, Z .

For small amplitude motion, the equation (2.14) can be approximated to:

$$\langle A_{ZZ} \rangle = A_{ZZ} - (A_{ZZ} - A_{XX}) \langle \alpha^2 \rangle \quad (2.15)$$

Therefore, the mean-square angular amplitude of libration can be evaluated as follows:

$$\langle \alpha^2 \rangle = \frac{A_{ZZ} - \langle A_{ZZ} \rangle}{A_{ZZ} - A_{XX}} \quad (2.16)$$

with A_{ZZ} and A_{XX} the principal components of the hyperfine tensor \mathbf{A} and $\langle A_{ZZ} \rangle$ the experimental value obtained from measuring the outer hyperfine splitting from EPR spectra [26].

2.3 Fourier-Transform EPR

Fourier-Transform electron paramagnetic resonance (FT-EPR) allows to overcome some limitations intrinsically present in conventional EPR, such as spectral and time resolution. FT-EPR applies intense microwave pulses to generate a magnetic response in the samples. Considering the simplest case where an ideal pulse $\delta(t)$ rises a system response $h(t)$, then $H(\omega)$ is its Fourier transformation in the frequency domain [12]:

$$\begin{aligned} H(\omega) &= \int h(t)e^{-i\omega t} dt \\ h(t) &= \frac{1}{2\pi} \int H(\omega)e^{i\omega t} d\omega \end{aligned} \tag{2.17}$$

The real part of $H(\omega)$ is the absorbance spectrum $A(\omega)$, while its imaginary part is the dispersion spectrum $D(\omega)$:

$$\begin{aligned} A(\omega) &= \text{Re}\{H(\omega)\} = \int h(t) \cos(\omega t) dt \\ D(\omega) &= \text{Im}\{H(\omega)\} = - \int h(t) \sin(\omega t) dt \end{aligned} \tag{2.18}$$

The pulse applied for a time t_p of intensity ω_1 rotates the magnetization vector \mathbf{M} of an angle $\beta = \omega_1 t_p$, called flip angle. After the pulse, \mathbf{M} precesses around the orientation of the static magnetic field \mathbf{H} (z axis). The transient signal observed is the free induction decay (FID). The free evolution of magnetization depends on the spin-spin relaxation time T_2 on the nanosecond time scale, also identified as the phase memory time T_{2M} .

2.4 Electron Spin Echo

The electron spin echo (ESE) technique detects the spin echo signal originating from the refocusing of the magnetization after the application of a sequence of pulses.

Figure 2.5 shows the Hahn (or primary) echo as a consequence of the application of a sequence of two pulses separated by a time interval τ ($\pi/2 - \tau - \pi - \tau - \text{echo}$). The first pulse ($\pi/2$) fans out the magnetization, \mathbf{M} , oriented along the z axis of the laboratory frame in the xy plane. In the time interval τ , when no microwave pulse is applied, \mathbf{M} dephases and the higher frequency spin packets move faster than the lower frequency ones, according to the relaxation time T_{2M} . The second inverting

pulse (π) flips \mathbf{M} about the x axis, the higher frequency spin packets are now moving towards the lower frequency ones and thus after an interval τ the magnetization is refocused.

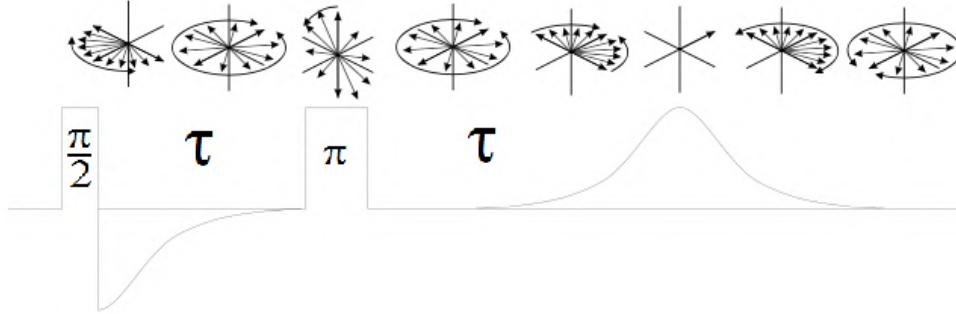


Figure 2.5: ESE signal after the application of a sequence of two pulses. The signal that decays after the first pulse (FID) is recovered by a second pulse and a Hahn (or primary) echo is produced. The magnetization precession and refocusing is also shown [102].

It is not possible to measure the signal until the high power microwaves are dissipated, this process occurs in a 80 ns period called deadtime. A very short FID will disappear before the deadtime ends.

The transverse relaxation processes lead to an exponential decay of the echo signal, $V(2\tau)$ [15]:

$$V(2\tau) \propto \exp\left(-\frac{2\tau}{T_{2M}}\right) \quad (2.19)$$

which depends on the phase memory time T_{2M} . Therefore, studying the echo amplitude decay at increasing interval τ allows the measurements of T_{2M} (figure 2.6). Because of the many contributions to T_{2M} , it is possible that not all of the spin packets after the application of the second pulse are able to refocus and thus not the entire magnetization is refocused.

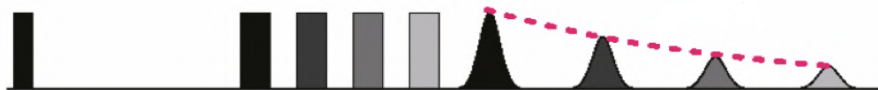


Figure 2.6: Echo height decay as a function of the time interval between pulses, τ .

The pulses choice determines the kind of experiment it is possible to perform. The echo resulting from an experiment that applies long lasting, low intensity pulses

(soft-pulses) does not take into account the modulation arising from the hyperfine interaction between the electron and the nucleus and it is used to determine T_{2M} . An experiment performed by integrating the echo signal while the external magnetic field is swept gives the absorbance spectrum defined as echo-detected (ED-EPR) spectrum. Short lasting, high intensity pulses (hard-pulses) excite not selectively the spectrum and the echo takes into account the hyperfine interaction modulation. An experiment performed as a function of the time interval between pulses reveals the electron spin echo envelope modulation (ESEEM) signal.

2.5 Librational motion from ED-EPR spectra

It is possible to study the dynamics of spin-labelled biosystems at cryogenic temperatures (77 - 270 K) by recording echo-detected electron paramagnetic resonance (ED-EPR) spectra. An ED-EPR experiment is a two-pulses experiment ($\pi/2 - \tau - \pi - \tau - echo$) in which at a fixed τ the primary echo is recorded and integrated while the static magnetic field is swept. The ED-EPR spectra recorded at increasing delay time τ at fixed temperature contain the information about the rotational molecular dynamics of spin-labels [15]. Therefore, an ED-EPR experiment allows studying the dynamics of spin-labelled systems at low temperature [26, 27]. Figure 2.7 shows the ED-EPR spectra of a nitroxide spin-label in a lipid membrane.

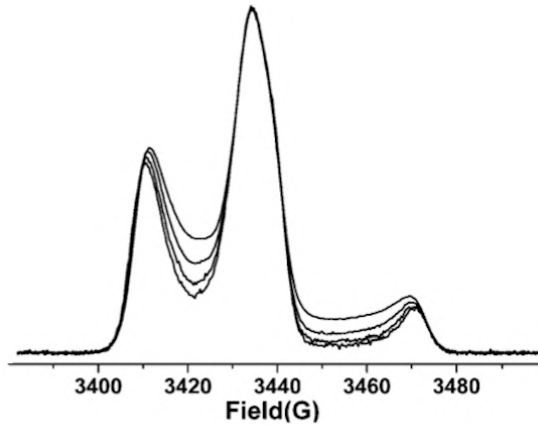


Figure 2.7: Absorbance ED-EPR spectra of a nitroxide spin-label in a DPPC bilayer at fixed temperature $T = 200$ K. Spectra at different delay time between pulses τ are shown. Spectra are normalized to the central line height. Figure adapted from [15].

At increasing τ , the low-field and high-field regions of the spectra relax faster than the others. These are spectral features of librational motion evidenced by

ED-spectra [14–16]. The pronounced changes in the lineshape depend on the re-orientation of the spin-labels with respect to the magnetic field. The outer regions and the central one, instead, do not change because they are not influenced by the angular dependence of the spectra.

For rapid motion, the echo intensity depends on the product of the resonance frequency shift, $\Delta\omega$, and the correlation time, τ_c , $\Delta\omega^2\tau_c^2$, which satisfies the condition for fast and small amplitude librations when $\Delta\omega^2\tau_c^2 \ll 1$. In the case of a ^{14}N -nitroxide, the resonance frequency $\omega_{m_I}(\theta, \varphi)$ is [14]:

$$\omega_{m_I}(\theta, \varphi) = g(\theta, \varphi) \frac{\beta}{\hbar} H + m_I A(\theta, \varphi) \quad (2.20)$$

with $A(\theta, \varphi)$ and $g(\theta, \varphi)$ from equation (2.12), H is the static magnetic field oriented along the Z axis and m_I is the nuclear magnetic quantum number.

Considering the polar angles (θ, φ) as the pair describing the orientation of the magnetic field with respect to the molecular frame, the phase-memory time, T_{2M} , is:

$$\frac{1}{T_{2M}} = \langle \Delta\omega^2(\theta, \varphi) \rangle \tau_c \quad (2.21)$$

and the echo decay curve is:

$$E(2\tau, \theta, \varphi) \approx \exp(-2\Delta\omega^2(\theta, \varphi)\tau_c\tau) \quad (2.22)$$

For librational motion of small amplitude of angular dependence α around the molecular axis Y , the frequency shift can be approximated to:

$$\Delta\omega(\theta, \varphi) = \alpha \left\{ \frac{\beta}{\hbar} H (g_{ZZ} - g_{XX}) + \frac{m_I (A_{ZZ}^2 - A_{XX}^2)}{A(\theta, \varphi)} \right\} \times \sin\theta \cos\theta \cos\varphi \quad (2.23)$$

where g_{ZZ} and g_{XX} , and A_{ZZ} and A_{XX} are the principal values of the \mathbf{g} tensor and the hyperfine tensor \mathbf{A} , respectively; H is the static magnetic field oriented along the Z axis; m_I is the nuclear spin quantum number; $A(\theta, \varphi)$ the hyperfine separation constant reported in equation (2.12). Analogously, for rotations around the molecular axes X and Z , $\Delta\omega(\theta, \varphi)$ is, respectively [14]:

$$\begin{aligned} \Delta\omega(\theta, \varphi) &= \alpha \left\{ \frac{\beta}{\hbar} H (g_{YY} - g_{ZZ}) + \frac{m_I (A_{YY}^2 - A_{ZZ}^2)}{A(\theta, \varphi)} \right\} \times \sin\theta \cos\theta \sin\varphi \\ \Delta\omega(\theta, \varphi) &= \alpha \left\{ \frac{\beta}{\hbar} H (g_{XX} - g_{YY}) + \frac{m_I (A_{XX}^2 - A_{YY}^2)}{A(\theta, \varphi)} \right\} \times \sin^2\theta \cos\varphi \cos\varphi \end{aligned} \quad (2.24)$$

The librational motion can be described with the so-called *isotropic model*. This model assumes stochastic changes in the orientation of the librational axis in all possible directions at different moments in time. The assumption is that simultaneous and independent librational motions each of amplitude α and correlation time τ_c occur around each of the three axes of the molecular frame. The net relaxation will be the product of the three relaxations induced by the independent librational motions around the three axes [16, 28].

The ED-EPR spectrum lineshape is the sum of the echo amplitudes evaluated for each orientation (θ, φ) of the magnetic field and for each hyperfine manifold ($m_I = 0, \pm 1$) of the nitroxide spin-label:

$$ED(2\tau, H) = \sum_{m_I} \frac{1}{4\pi} \int \int \sin \theta \, d\theta \, d\varphi \, f\left(H - \frac{\omega_{m_I}(\theta, \varphi)}{\gamma}\right) \times E(2\tau, \theta, \varphi) \quad (2.25)$$

where $E(2\tau, \theta, \varphi)$ came from equation (2.22) and $f(\Delta H)$ is the lineshape for a single spin packet. The result will be a convolution of a Gaussian and a Lorentzian functions, with inhomogeneous broadening because of the unresolved proton hyperfine interaction [16, 28].

At the temperature $T = 77$ K, it can be assumed that no molecular motion is possible in a spin-labelled system and the spectral lineshape depends just on the instantaneous diffusion, a spin-spin interaction that modulates the resonance frequency. Instantaneous diffusion arises from flipping of surrounding electron spins by the inverting second pulse in the primary-echo sequence. Indeed, the π -pulse changes orientation of spins and therefore changes the direction of dipolar fields. The effect of instantaneous diffusion is the preferential reduction of the central manifold intensity [14, 103]. Because instantaneous diffusion is temperature independent, ED-EPR spectra recorded at temperature $T > 77$ K, need to be corrected with the spectrum recorded at the lowest temperature [16]:

$$ED_T^{corr}(2\tau, H) = ED_T(2\tau, H) \frac{ED_{77K}(2\tau_0, H)}{ED_{77K}(2\tau, H)} \quad (2.26)$$

where τ_0 is the shortest τ value.

By comparing ED-EPR spectra at different τ values and normalized at the central line height, to eliminate any possible contribution to the relaxation processes independent from the magnetic field, it is possible to highlight how the low field and high field spectral regions are influenced by the exponential decay at increasing interpulse delay time τ as a consequence of the librational motion (figure 2.8a) [104].

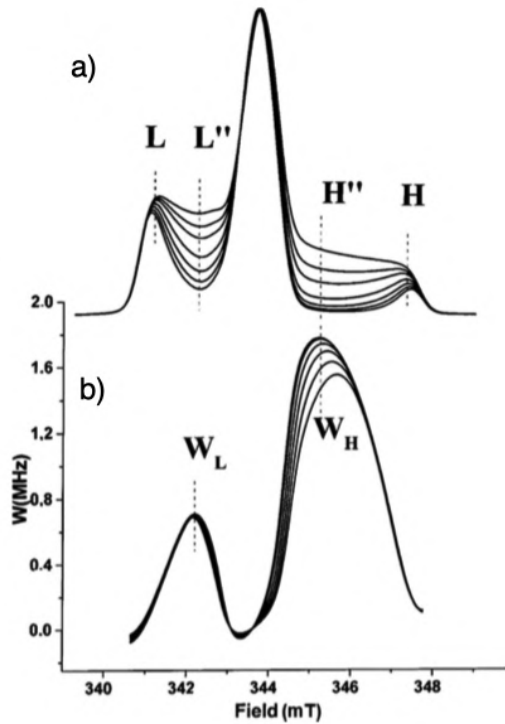


Figure 2.8: a) Simulated ED-EPR spectra recorded at different delay time τ and normalized at the central line height. L, L'', H, H'' are the line heights at low and high field. b) Anisotropic part of the relaxation rate W at low field, W_L , and high field, W_H [16].

The ED-EPR spectra dependence from the librational dynamics can be analyzed from the anisotropic component of the relaxation rate, W . This parameter is the ratio of the lineshape obtained with the shortest interpulse spacing τ_0 to the lineshapes recorded at $\tau_i > \tau_0$:

$$W(H, \tau_0, \tau_i) = \ln \left(\frac{ED(2\tau_0, H)}{ED(2\tau_i, H)} \right) \times \frac{1}{2(\tau_i - \tau_0)} \quad (2.27)$$

with $ED(2\tau, H)$ from equation (2.25) [14, 16].

The anisotropic relaxation process for an individual spin packet and a particular orientation (θ, φ) is exponential, as expected from equation (2.22) both in the low field, W_L , and high field, W_H , region: the W intensities are superimposed at each τ , as it can be seen from figure 2.8b. At each temperature, from the simulated ED-EPR spectra at increasing τ value, the motion parameter $\langle \alpha^2 \rangle \tau_c$ can be obtained, which is the product of the mean-square angular amplitude of libration $\langle \alpha^2 \rangle$ and the correlation time of motion τ_c . The motion parameter depends on the relaxation rate according to the relation $W = k_{cal} \langle \alpha^2 \rangle \tau_c$. The calibration constant, k_{cal} , can be obtained for both W_L and W_H through simulations or considering the

slope of the logarithmic plots of the line heights at low and high field, respectively, $d\ln(L''/L)/\tau = k_{cal}\langle\alpha^2\rangle\tau_c$ and $d\ln(H''/H)/\tau = k_{cal}\langle\alpha^2\rangle\tau_c$ [14,16].

The librational dynamics can be fully characterized combining spin-label two-pulse echo detected spectra and cw-EPR. Indeed, the product $\langle\alpha^2\rangle\tau_c$, depending on the relaxation rate W , can be obtained from the two-pulse experiment, and, independently, the amplitude of the librational motion, $\langle\alpha^2\rangle$, can be deduced from the continuous-wave experiment as described in equation (2.16). Finally, the correlation time of the librational motion, τ_c , can be determined from the two evaluations.

2.6 ESEEM spectroscopy

Electron spin echoes are generated in response to suitable resonant pulse sequences, which reorient the magnetic dipoles [105]. Their dephasing and consequent rephasing originates the echo. The echo, therefore, measures the net magnetization of the spin system at a given time. In an experiment in the time domain in which the interpulse separation, τ , is increased, it is recorded the monotonous decay of the echo amplitude. Sometimes, the echo decay is accompanied by periodic falls and rises in the amplitude. These modulations arise from the weak hyperfine interactions between the electron spin and the nuclear spins of the nearby nuclei. The periodic dependence on τ of the oscillations is determined by the nuclear hyperfine frequencies. The modulation effects are called electron spin echo envelope modulation (ESEEM) [14,106].

The interaction that contributes as first-order splittings in an ESEEM experiment is the nuclear electric quadrupole coupling interaction manifesting for nuclei with spins $\mathbf{I} \geq 1$ (i.e., ^{14}N or ^2H). It arises from the interaction of the nuclear quadrupole moment, Q , with the electric field gradient produced by the electronic environment of the nucleus, and its Hamiltonian can be written as [12,14]:

$$\mathcal{H}_{nq} = \mathbf{I} \cdot \mathbf{Q} \cdot \mathbf{I} \quad (2.28)$$

where \mathbf{Q} is the nuclear quadrupole tensor. Thus, the nuclear quadrupole Hamiltonian is:

$$\mathcal{H}_{nq} = \frac{e^2qQ}{4I(2I-1)\hbar} [(3I_Z^2 - I(I+1)) + \eta(I_X^2 - I_Y^2)] \quad (2.29)$$

where eq is the electric field gradient and $\eta = (Q_X - Q_Y)/Q_Z$.

2.6.1 Three-pulse ESEEM

In a three-pulse ESEEM ($\pi/2 - \tau - \pi/2 - T - \pi/2 - \tau - echo$) experiment, the time delay τ between the first and the second pulses is fixed, instead the time delay T between the second and the third pulses is incremented (figure 2.9). The advantage of a three-pulse ESEEM experiment with respect to the more straightforward two-pulse experiment is an increase in resolution after a Fourier transformation (ESEEM spectrum), because the echo modulation is recorded on a large time period. The linewidth in a three-pulse ESEEM spectrum is determined by the phase memory time of the nuclear spin that is on the time scale of the the spin-lattice relaxation time, T_1 , of the electron spin.



Figure 2.9: ESE signal after the application of a three-pulse sequence.

Considering the two possible spin states for an electron with spin quantum number $m_s = \pm 1/2$, during the evolution time T the magnetization is along the Z -direction and thus the echo amplitude, E_{3p} , is the superposition of the two states [14]:

$$V_{3p}(2\tau + T) = \frac{1}{2} \left[V_{3p}^{1/2}(2\tau + T) + V_{3p}^{-1/2}(2\tau + T) \right] \quad (2.30)$$

with $V_{3p}^{1/2}$ and $V_{3p}^{-1/2}$ the echo amplitudes for the electron spin states $m_s = 1/2$ and $m_s = -1/2$, respectively. In the particular case of a nucleus with nuclear spin $\mathbf{I} = \frac{1}{2}$ (i.e., ^1H) it is [14]:

$$\begin{aligned} V_{3p}(2\tau + T) = & 1 - \frac{k}{4} [(1 - \cos \omega_{-1/2}\tau) (1 - \cos \omega_{1/2}(\tau + T)) + \\ & + (1 - \cos \omega_{1/2}\tau) (1 - \cos \omega_{-1/2}(\tau + T))] \end{aligned} \quad (2.31)$$

with k the modulation depth parameter, and $\omega_{1/2}$ and $\omega_{-1/2}$ the angular frequencies for nuclear transitions for the electron spin states $m_s = 1/2$ and $m_s = -1/2$, respectively. For weak hyperfine couplings, the angular frequencies can be considered equal to the Larmor frequency ω_l of the nucleus.

In analogy, considering a nuclear spin $\mathbf{I} = 1$ (i.e., ^{14}N or ^2H) [14]:

$$\begin{aligned}
 V_{3p}(2\tau + T) = & 1 - \frac{2}{3}k[(1 - \cos \omega_{-1/2}\tau) (1 - \cos \omega_{1/2}(\tau + T)) + \\
 & + (1 - \cos \omega_{1/2}\tau) (1 - \cos \omega_{-1/2}(\tau + T))] + \\
 & + \frac{k^2}{6}[(1 - \cos \omega_{-1/2}\tau)^2 (1 - \cos \omega_{1/2}(\tau + T))^2 + \\
 & + (1 - \cos \omega_{1/2}\tau)^2 (1 - \cos \omega_{-1/2}(\tau + T))^2]
 \end{aligned} \tag{2.32}$$

The modulation depth depends on the nuclear frequency through the only τ -dependent terms in equations (2.31) and (2.32). It is possible to eliminate some ESEEM components simply choosing particular τ values for which $\cos \omega_l \tau = 1$. On the opposite, the echo amplitude can be optimized for a specific nucleus choosing τ values for which $\cos \omega_l \tau = -1$. For instance, $\tau = 168$ ns optimizes deuterium and proton modulation simultaneously, while $\tau = 204$ ns suppresses the proton modulations [14, 17].

If in the case of nuclei with $\mathbf{I} = 1$, we consider a weak quadrupole interaction, which contributes as another components to the modulation, the equation (2.32) becomes:

$$\begin{aligned}
 V_{3p}(2\tau + T) = & 1 - \frac{4B^2}{3\omega_l^2} [1 - \cos \omega_l \tau \cos \frac{1}{2}A\tau \cos Q\tau + \\
 & - \cos \omega_l(\tau + T) \cos \frac{1}{2}A(\tau + T) \cos Q(\tau + T) + \\
 & + \frac{1}{2} \cos \omega_l(2\tau + T) \cos \frac{1}{2}AT \cos Q(2\tau + T) + \\
 & + \frac{1}{2} \cos \omega_l T \cos \frac{1}{2}A(2\tau + T) \cos QT]
 \end{aligned} \tag{2.33}$$

where A and B are hyperfine constants function of the axial hyperfine tensor \mathbf{A} , and Q is the quadrupole coupling that depend on the orientation θ of the static magnetic field [14].

To compare different ESEEM spectra and their intensities, it is important to follow a data-processing procedure that gives a machine independent result [17, 107]. An example of the procedure for the particular case of a nitroxide spin-labeled sample hydrated in deuterium is described in figure 2.10.

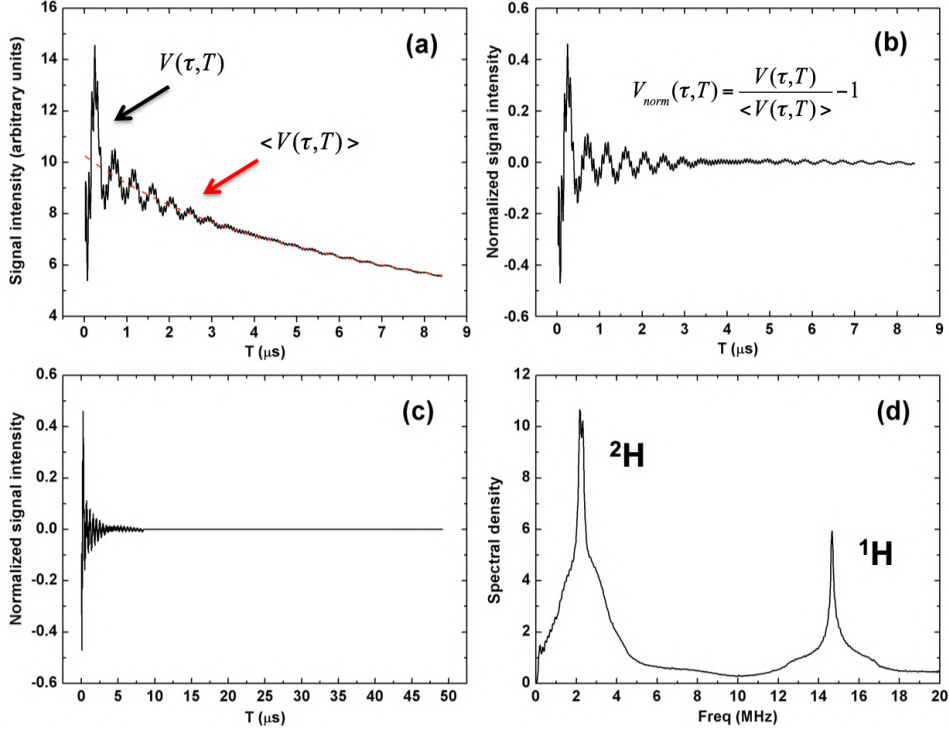


Figure 2.10: (a) Decay of the 3p-ESE; (b) normalized ESEEM modulation signal (c) zero-filling procedure: to increase resolution null points are added (d) Fourier transform (ESEEM spectrum): two peaks at the characteristic NMR frequencies of deuterium (^2H) at 2.5 MHz and of protons (^1H) at 14.6 MHz.

The echo decay amplitude $V_{3p}(\tau, T)$ is fitted with a biexponential function to obtain the average echo decay $\langle V_{3p}(\tau, T) \rangle$; the normalized echo decay amplitude, $V_{norm}(\tau, T)$, is obtained by dividing the echo decay amplitude by the fitted average decay function and subtracting the unit level as described in the following equation:

$$V_{norm}(\tau, T) = \frac{V_{3p}(\tau, T)}{\langle V_{3p}(\tau, T) \rangle} - 1 \quad (2.34)$$

In this way the decay is suppressed and only the modulations are present.

To increase the total number of points and thus the resolution, null points are added at the end of the resulting function, obtaining the full information in the real part of the spectrum. Then the normalized signal in the time domain is Fourier transformed in order to have a discrete signal of finite length in which the noise contribution is confined to a frequency region where no signals are expected. In the frequency domain, the information arising from the different nuclei are separated, with their signals centered at their Larmor frequencies (deuterons resonate at ca. 2.5 MHz, protons resonate at ca. 14.6 MHz), and the quadrupole interaction manifests itself as a doublet splitting (Pake doublet) [17, 107].

2.6.2 D₂O-ESEEM

Three-pulse electron spin echo envelope modulation by deuterium (D₂O-ESEEM) spectroscopy is used to investigate the solvent properties in the nearest hydration shell of nitroxide spin-labelled systems, hydrated in D₂O. It is used to determine the direct solvent (D₂O) accessibility at the labeling site into the biosamples, and it also gives information on the hydrogen-bonding formation (single or double H-bonding of nitroxide with D₂O molecules) [17, 18, 108].

The D₂O-ESEEM echo amplitude decay (see the first panel of figure 2.10) is composed by the superposition of rapid oscillations, due to the weak hyperfine interaction of the spin-label with protons, and slow modulations, reflecting the hyperfine interaction with deuterium. A D₂O-ESEEM spectrum (see the last panel of figure 2.10) consists of the superposition of a broad component of intensity I_{broad} evaluated at 2.6 MHz, and a narrow component of intensity I_{narrow} evaluated at 2.2 MHz. The first one arises from the D₂O molecules H-bonded to the spin-label, while the second one arises by the dipolar interaction of D₂O molecules that are not H-bonded to the spin-labels and originates the doublet (figure 2.11) [17]. The two components have been assigned by combining DTF calculations and classical EPR simulations. A model has been assumed in which the nitroxide spin-label group can form one or two hydrogen bonds with the nearest deuterons, and 12 bulk solvent molecules are distributed over a radius of 0.5 nm [17].

The total amplitude of the deuterium ESEEM signal, I_{tot} , at 2.5 MHz is determined by the distance, r , of the D₂O ²H-nuclei from the spin-label and by the number, n , of D₂O molecules neighboring the spin-label, and it is proportional to n/r^6 [12, 18, 106, 109]. The high order dependence on the distance and the magnetic properties of deuterium indicate that only nuclei within 0.5 - 0.8 nm contribute to the ESEEM signal, as shown in the theoretical models described in [17, 18]. I_{tot} , therefore, gives a direct measure of the solvent (D₂O) permeation at the site-specifically labeled position in the sample.

While I_{tot} varies, the ratio of the narrow component to the broad one remains constant, suggesting that the H-bonding of one and two water molecules to the nitroxide radical follows the following local equilibrium:



where W represent the water molecules, R the nitroxide radical, K_1 and K_2 are the association constants for binding the first and the second water molecules. If the

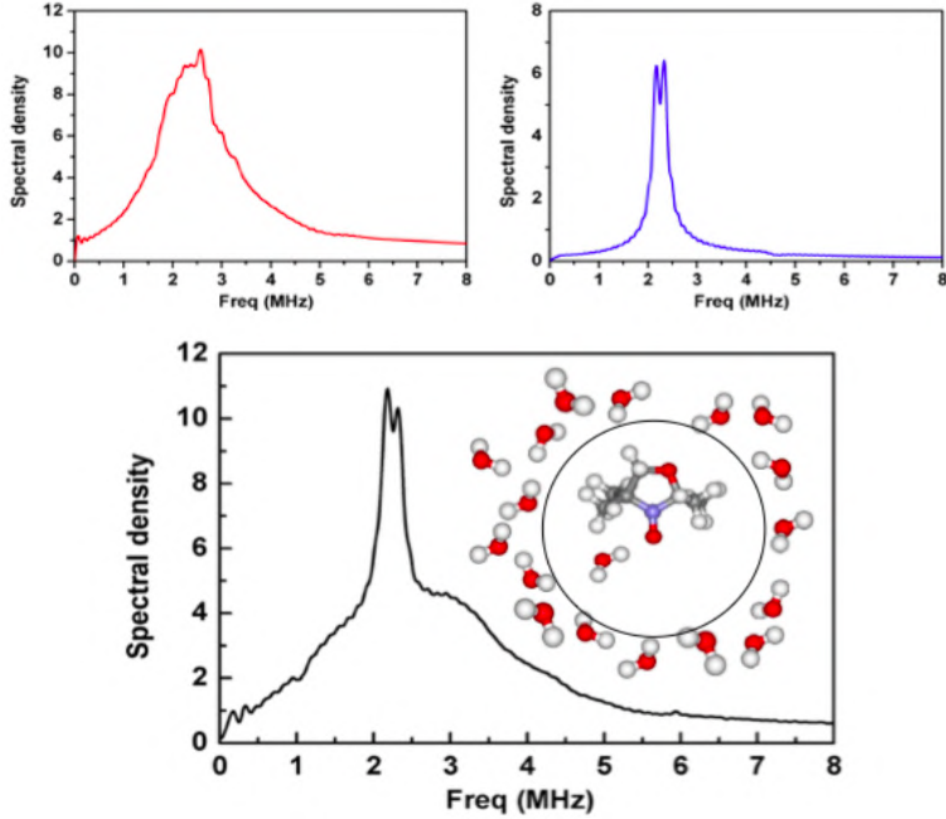


Figure 2.11: *Upper panel:* Simulated lineshapes of the broad component (left) and the narrow component (right) in the D_2O -ESEEM spectrum of a nitroxide spin-label. *Lower panel:* Experimental D_2O -ESEEM spectrum resulting from the superposition of the broad and narrow components; the model of the deuterium molecules in the vicinity of the spin-labels is also given.

binding of W_2 is independent from the binding of W_1 , K_1 and K_2 are related to the intrinsic binding constant K for binding to an isolated single site. Conservation of the number of spin labels requires:

$$[R]_0 = [R] + [W_1R] + [W_2R] \quad (2.36)$$

where $[R]_0$ is the total concentration of spin labels.

The normalized intensity of the broad component under equilibrium is [17]:

$$\frac{I_{broad}}{I_0} = \frac{[W_1R]}{[R]_0} + \frac{2[W_2R]}{[R]_0} \quad (2.37)$$

with $I_0 = 115$ ns the intensity for a single water molecule permanently bound to the nitroxide, the value previously evaluated through DFT calculations [17].

Applying the law of mass action and considering equation (2.36), equation (2.37)

becomes:

$$\frac{I_{broad}}{I_0} = \frac{2K[W]}{1 + K[W]} \quad (2.38)$$

that confirms the dependence of the broad component amplitude on the local water concentration.

It is possible to determine the populations of doubly and singly H-bonded nitroxides to water molecules. The ratio of the two populations is:

$$\frac{[W_2R]}{[W_1R]} = \frac{K[W]}{2} \quad (2.39)$$

The fraction of spin label singly H-bonded, f_{1W} , is the following:

$$f_{1W} = \frac{2}{\left(\frac{1}{K[W]}\right) + 2 + K[W]} \quad (2.40)$$

and the fraction of the doubly H-bonded population, f_{2W} , is:

$$f_{2W} = \frac{1}{2} \left(\frac{I_{broad}}{I_0} - f_{1W} \right) \quad (2.41)$$

All of the above information that can be obtained from a three-pulse D₂O-ESEEM experiment allows the determination, for instance, of the water penetration profile and the transmembrane polarity profile in a lipid membrane or the interaction of water with the transmembrane domains of integral proteins.

3.1 Materials

Synthetic lipids 1-palmitoyl-2-oleoyl-*sn*-glycero-3-phosphocholine (POPC), 1,2-dioleoyl-*sn*-3-glycero-phosphocholine (DOPC) and polymer lipid 1,2-dipalmitoyl-*sn*-glycero-3-phosphoethanolamine-N-poly(ethylene glycol) (PEG:2000-DPPE) were purchased from Avanti Polar Lipids (Alabaster, AL); the spin-labeled lipids 1-palmitoyl-2-(*n*-(4,4-dimethyl-oxazolidine-N-oxyl)stearoyl)-*sn*-glycero-3-phosphocholine (*n*-PCSL) were from Avanti Polar Lipids as well or synthesized as described elsewhere [110]. Synthetic lipids 1,2-dipalmitoyl-*sn*-glycero-3-phosphocholine (DPPC) and 1-palmitoyl-2-lyso-*sn*-glycero-3-phosphocholine (Lyso-PPC), the spin-labeled maleimide 3-maleimido-1-oxyl-2,2,5,5-tetramethylpyrrolidine (5-MSL), proteins Human Serum Albumin (HSA) and bovine β -Lactoglobulin (β -LG), ethanol and deuterium oxide (99.9 atom% ^2H) were purchased from Sigma Aldrich (St. Louis, MO). All materials were used as purchased without further purification.

3.2 Sample preparation

Spin-labelled fully hydrated lipid vesicles were prepared by the thin film hydration method. Appropriate amount of lipids were dissolved in chloroform with 0.5 mol% of *n*-PCSL spin-labeled lipid. The solvent was first evaporated under a nitrogen gas stream and then under vacuum overnight. The dried films were then fully hydrated in D_2O by heating at temperature higher than the main transition temperature of the lipids and periodically vortexing. The hydrated samples (final

lipid concentration 50 mM) were concentrated at room temperature by pelleting in a bench-top centrifuge at 3000 rpm for 20 minutes, the excess of solvent removed and the samples finally loaded in standard 3 mm diameter quartz tubes.

For experiments reported in Chapter 6, lipid bilayers were prepared as described above at full hydration in bi-distilled water at a ratio $n_w/n_L = 25$, with n_w and n_L number of water molecules and of lipid molecules, respectively, ensuring saturation of lipids with water [111]. The low hydrated samples ($n_w/n_L = 3 - 4$) and, then, dehydrated samples were obtained by carefully evaporating the solvent in a desiccator and, finally, checking the sample weight. In particular, the low hydrated samples with less than 12 water molecules per lipid molecule are below the limit of complete hydration for the phosphocholine group, with most of the water molecules hydrogen-bonded to the lipids [112–114]. Proteins were spin-labeled with 5-maleimide spin-labels as described elsewhere [22, 115]. The lyophilized samples were measured and then fully hydrated in bi-distilled water with more than 0.55 mg of water per 1 mg of protein ($h > 0.55$). The low hydration sample contained 0.1 - 0.14 mg of water per 1 mg of protein ($h = 0.10 - 0.14$) and was obtained by careful evaporation of the solvent in the fully hydrated sample.

3.3 EPR measurements

Continuous wave electron paramagnetic resonance spectra were acquired on a Bruker ESP-300 spectrometer operating at 9 GHz, equipped with a Bruker ER 4201 TE₁₀₂ standard rectangular cavity and a Bruker ER 411VT temperature controller. Spectra were recorded at 10 mW microwave power with 2-3 Gauss_{pp} magnetic field modulation amplitude and with 100-kHz field modulation. For measurements at 77 K, samples were rapidly frozen in liquid nitrogen and then introduced into a finger dewar containing liquid nitrogen and positioned in the spectrometer cavity.

Pulsed EPR experiments were executed on a Bruker ELEXSYS E580 FT-EPR spectrometer operating at 9 GHz equipped with a MD5 dielectric resonator and a CF 935P cryostat (Oxford instrument, UK). Tubes containing samples were rapidly frozen in liquid nitrogen and then quickly accommodated into the pre-equilibrated cavity at 77 K.

Primary, two-pulse ($\pi/2 - \tau - \pi - \tau - echo$) echo-detected (ED)-EPR spectra were obtained by recording the integrated spin-echo signal at fixed interpulse delay τ , while sweeping the magnetic field. The microwave pulse widths were 32 and 64 ns, with the microwave power adjusted to provide $\pi/2$ and π pulses, respectively. The magnetic field was set to the EPR absorption maximum, and the integration window was 160 ns. ED-spectra were corrected according to equation (2.26) and

the relaxation rates, W , obtained according to equation (2.27).

For three-pulse D₂O-ESEEM experiments, stimulated echo decays ($\pi/2 - \tau - \pi/2 - T - \pi/2 - \tau - echo$) were recorded by using microwave pulse widths of 12 ns, with the microwave power adjusted to give $\pi/2$ -pulses. The time delay, T , between the second and the third pulses was incremented from 20 ns by 700 steps of 12 ns, whilst the inter-pulse separation, τ , between the first and second pulses was set equal to 168 ns to maximize the deuterium and proton modulations simultaneously. The magnetic field was set to the maximum of the EPR absorption. A four-step phase-cycling program was used to eliminate unwanted echoes. For obtaining Fourier-Transform ESEEM spectra, i.e., standardized ESEEM intensities in the frequency domain, the time-dependent echo amplitudes were processed as reported in Section 2.6. Fourier transformed ESEEM spectra are, finally, multiplied by the dwell time, ΔT , in order to obtain machine-independent spectral densities with the dimensions of time (nanoseconds) [107]. This procedure ensures the validity of comparing measurements among different D₂O-containing systems.

Water penetration in biosystems

The extent of water penetration at selected regions of biosystems is relevant because it gives insight on the permeability and polarity properties in membranes as well as on the stability and function of membrane proteins. This research topic is appropriately studied by continuous-wave electron paramagnetic resonance (cw-EPR) and three-pulse electron spin echo envelope modulation by deuterium (D_2O -ESEEM) combined with site-specific spin-labeling technique. By means of these EPR methods we focused on molecular aggregates formed by binary mixtures of bilayer-forming lipids and micelle-forming lipids fully hydrated in D_2O . Diacyl phosphatidylcholines are used as bilayer-forming lipids, whereas polymer-grafted lipids like phosphatidylethanolamines (PEs) with hydrophilic polymer N-polyethylene glycol (PEG) covalently attached on the polar heads (PEG-lipids) or single-chain Lyso-phosphatidylcholines are used as micelle-forming lipids. In particular, while the PEG-lipids are able to guide the transition from a lamellar to a micellar phase, Lyso-Pcs induce micellization going first through an interdigitated lamellar phase. Another issue that will be studied is the interaction of the Na^+,K^+ -ATPase membrane protein with bufadienolide cardiotonic steroids, which are specific inhibitor of the sodium pump.

Results and discussion, as well as adapted figures, of the present Chapter are from the published articles [116–119].

4.1 Lyotropic phase behavior of bilayer-forming lipids and micelle-forming lipids mixtures

4.1.1 Diacyl- and polymer-lipids mixtures

Polymer-lipids are lipid molecules modified in the headgroup with hydrophilic polymers, thus exhibiting properties of both polymers and lipids. In the case of PEG-lipids, the polymer is composed by a number of repetitive (CH₂-CH₂-O) units, or degree of polymerization, n_p , and it is able to create a biocompatible coating. This particular property raises the interest of researchers for application in biotechnological and pharmacological fields: PEG-lipids are essential components of efficient drug carriers known as long circulating sterically stabilized, or Stealth, liposomes (SLL) [66–69]. Specifically, dipalmitoylphosphatidylethanolamine (DPPE) with poly(ethylene-glycol) of average molecular weight 2000 Da ($n_p = 45$) covalently attached at the polar head (PEG:2000-DPPE) has been used in the present study. The geometry of such a molecule is comparable to a cone with packing parameter close to 1/3, therefore at full hydration PEG:2000-DPPE polymer-lipids self-assemble into micelles [120]. D₂O-ESEEM and cw-EPR experiments were conducted at 77 K on rapidly frozen mixtures made of saturated DPPC mixed with PEG:2000-DPPE over the entire composition range (0 - 100 mol%) spin-labeled at different C_n atom position along the *sn*-2 chain ($n = 4, 5, 7, 8, 9, 10, 11, 12, 14, 16$) (see figure 4.1 for chemical structures).

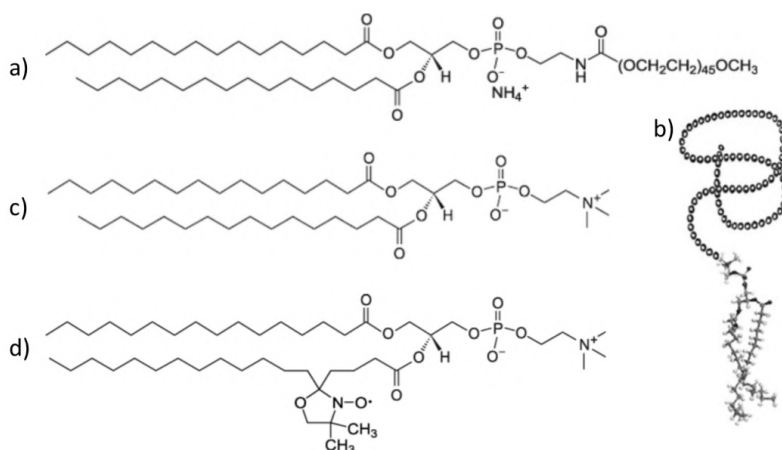


Figure 4.1: Structures of *a*) and *b*) polymer-lipid PEG:2000-DPPE, *c*) saturated lipid DPPC, and *d*) spin-labeled lipid 5-PCSL.

We have investigated the phase behavior of the mixtures and the profiles of water accessibility and polarity across the hydrocarbon region as well as the properties of

the solvent in the different formed lipid aggregates.

Figure 4.2 shows selected three-pulse ESEEM measurements carried out on DPPC mixed with increasing amount of PEG:2000-DPPE, fully co-hydrated in D_2O in the presence of 0.5 mol% of spin-labelled lipid 5-PCSL, which investigates the polar/apolar interface between the lipid environment and the solvent.

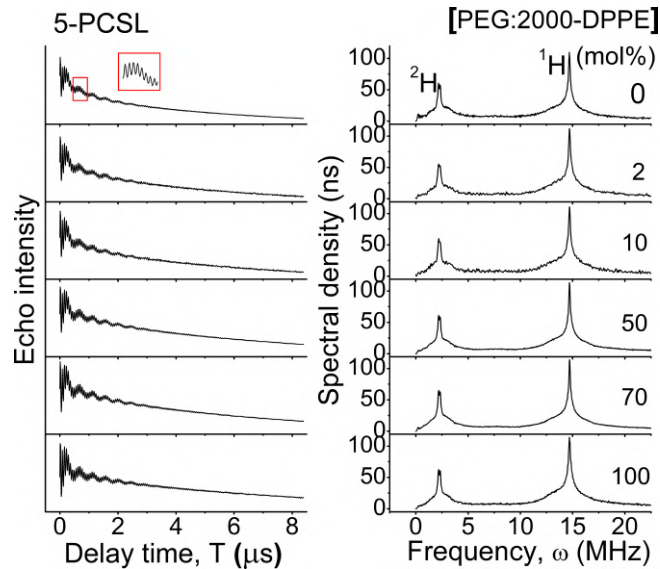


Figure 4.2: *Left:* decay curves at 77 K of the three-pulse electron spin echo intensity as a function of the delay time, T , between the second and the third pulses for 5-PCSL in DPPC/PEG:2000-DPPE mixtures hydrated in D_2O at the polymer-lipid mole fraction indicated on the figure. *Right:* Fourier-Transform ESEEM spectra for samples as in the left panel.

In the left panel decays of the maximum amplitude of the stimulated echo with respect to the interpulse spacing, T , are shown. They present the typical superposition of slow modulations, due to the dipolar interaction of the nitroxide with the surrounding deuterium nuclear spins, and small rapid modulations due to interactions of the nitroxide with the nearby protons. The right panel contains the corresponding absolute-value frequency D_2O -ESEEM spectra. Both the amplitude of the slow D_2O -oscillations in the time domain decays and the corresponding intensity of the deuterium 2H -peaks at the characteristic Larmor frequency 2.5 MHz in the frequency domain spectra show slight variations with increasing concentration of the polymer-lipid incorporated in the DPPC host matrix. In contrast, the 1H signal is sample-independent in both cases.

ESEEM measurements with 16-PCSL (i.e., the other extreme labeling position at the terminal methyl segment of the hydrocarbon chains) exhibit the slow modulations from deuterons showing up at 10 mol% content of PEG:2000-DPPE and the

modulation depth increasing progressively up to 100 mol% of PEG:2000-DPPE (see left panel of figure 4.3).

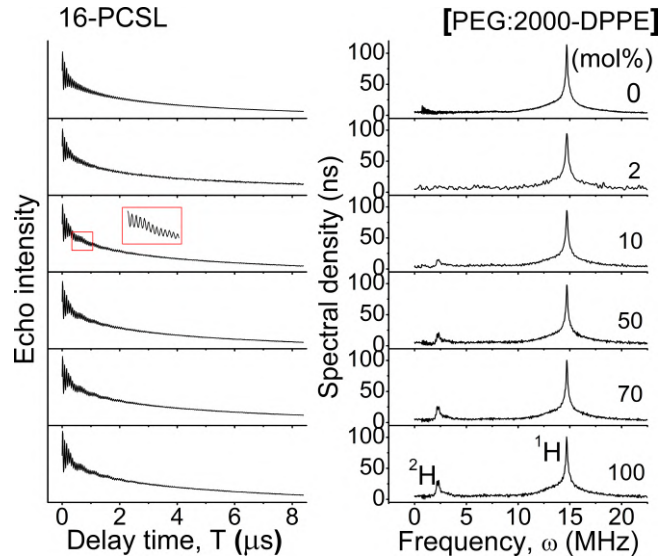


Figure 4.3: *Left:* decay curves at 77 K of the three-pulse electron spin echo intensity as a function of the delay time, T, between the second and the third pulses for 16-PCSL in DPPC/PEG:2000-DPPE mixtures hydrated in D₂O at the polymer-lipid mole fraction indicated on the figure. *Right:* Fourier-Transform ESEEM spectra for samples as in the left panel.

Correspondingly, the ESEEM frequency spectra for 16-PCSL in the right panel of figure 4.3 clearly show that the solvent ²H-peak shows up at 10 mol% of PEG:2000-DPPE and then its intensity progressively and moderately increases with the polymer-lipid concentration up to 100 mol%. Note that the proton ¹H-peak has a constant intensity over the whole polymer-lipid concentration range.

Quantitatively, the total amplitude of the deuterium ESEEM signal, $I(^2\text{H})$, evaluated as the intensity of the Fourier transform of the ESEEM decay at 2.2 MHz and corrected by the background signal [12, 17, 18], gives a direct measure of the solvent (D₂O) accessibility at the nitroxide-labeling site. Figure 4.4 shows the dependence of $I(^2\text{H})$ for 5- and 16-PCSL in DPPC/PEG:2000-DPPE mixtures as a function of the polymer-lipids concentration.

In DPPC bilayers (0 mol% polymer-lipid), there is an intense solvent peak of about 59 ns at the polar/apolar interface probed by 5-PCSL and a null signal at the bilayer midplane probed by 16-PCSL, typical of bilayers in which the midplanes are not accessible to water [17]. In PEG:2000-DPPE micelles (100 mol% polymer-lipid), instead, a solvent peak is evident not only for 5-PCSL ($I(^2\text{H}) \approx 63$ ns) but also for 16-PCSL ($I(^2\text{H}) \approx 29$ ns). Therefore, PEG:2000-DPPE micelles are characterized by higher solvent accessibility at the polar/apolar interface and by solvent permeation

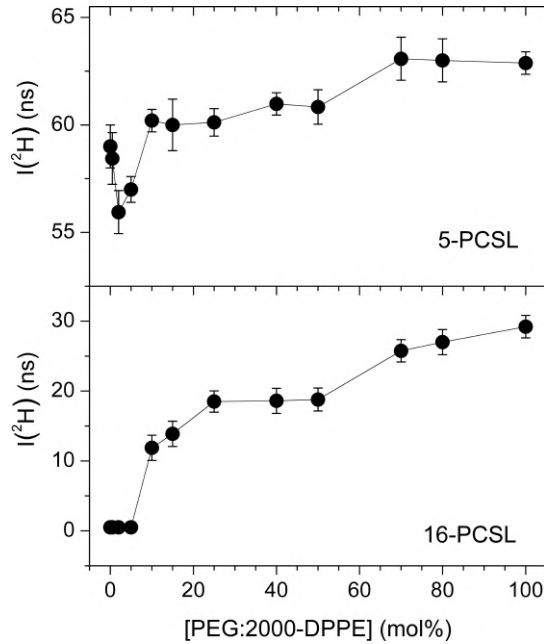


Figure 4.4: Dependence at 77 K on PEG:2000-DPPE concentration of the deuterium spectral amplitudes, $I(^2\text{H})$, for (*upper panel*) 5-PCSL and (*lower panel*) 16-PCSL in DPPC/PEG:2000-DPPE/ D_2O dispersions.

in the terminal region of the hydrocarbon chains. These findings reflect the differences in chain packing between bilayers and micelles: the increased area per polar head allows more water permeation at the polar/apolar interface in micelles than in bilayers and some configurational disorder makes the deep hydrocarbon interior of micelles accessible to water.

Mixtures of DPPC and low content of PEG:2000-DPPE lipids are of interest. It has been found that when the PEG-lipids concentration is increased at low content, the hydrophilic polymer chains attached to the lipid polar heads undergo a transition from a non interacting random coiled (mushroom) configuration to an extended (brush) configuration [69, 121–123]. The mole fraction, X_{PEG} , at which the mushroom-to-brush transition occurs depends on the molecular weight or the degree of polymerization, n_p , of the polymer. In the case of PEG:2000-DPPE ($n_p = 45$) $X_{PEG} \approx 1.2$ mol% [69, 123]. In figure 4.4, the presence of PEG:2000-DPPE at concentrations up to 5 mol% leads to a decrease in the D_2O signal intensity at the polar/apolar interface, while the corresponding intensity at the terminal methyl end maintains zero value. This behavior reflects the steric protection provided to the bilayer surface by the polymer and the formation of sterically stabilized liposomes (SSL) at $X_{PEG} = 2$ mol%. The reduced water content at the 5-PCSL probed region is consistent with previous findings on the dehydration activity of the polymer brush

on the DPPC surface [124] and an increase in the DPPC packing density [122].

For $5 \text{ mol}\% < X_{PEG} < 10 \text{ mol}\%$, the steric lateral pressure of the brush extension is responsible of the expansion in the DPPC area per polar head with the consequent increase in water penetration at the 5-PCSL probed membrane region. Then, for X_{PEG} up to 50 mol%, polymer-grafted bilayers and polymer-grafted micelles coexist at different proportion and the hydrophobic core becomes accessible to the solvent. Finally, for $X_{PEG} > 50 \text{ mol}\%$ the micellization transition is completed and the water accessibility both at the first hydrocarbon segment and at the deepest hydrocarbon interior is augmented with respect to DPPC bilayers (i.e., 0 mol% PEG-lipids).

More specifically, for SLL formed by mixing DPPC and 2 mol% PEG:2000-DPPE in D_2O we have delineated the transmembrane profile of water penetration and polarity by using a variety of chain-labeled lipids, n -PCSL, by evaluating the $I(^2H)$ ESEEM intensity and the A_{ZZ} half hyperfine splitting, respectively.

Figure 4.5 reports the $I(^2H)$ data in the upper panel and the A_{ZZ} data in the lower panel for both DPPC/PEG:2000-DPPE SSL mixture and, for comparison, DPPC bilayers previously studied [17, 125].

The $I(^2H)$ -values in the upper panel of figure 4.5 for SSL decrease with a sigmoidal trend on moving along the chain, from the first water-accessible CH_2 segments to the terminal water-inaccessible chain segments. Interestingly, the depth-dependent changes in A_{ZZ} in the lower panel also show a similar decrease from the first chain positions toward the end of the chains, indicating that the polarity decreases on moving along the chain in SSL. The profiles exhibited by both the parameters in the upper and lower panel of figure 4.5, have been successfully fitted with the following sigmoidal function:

$$P(n) = \frac{P_1 - P_2}{1 + e^{(n-n_0)/\lambda}} + P_2 \quad (4.1)$$

where $P(n)$ is the parameter, $I(^2H)$ or A_{ZZ} , as a function of the labeling position, n , P_1 and P_2 are the limiting values of P at the polar headgroups and terminal methyl ends, respectively, λ is an exponential decay constant, and n_0 is the labeling position where the gradient of the curve is maximum. Equation (4.1) describes a transition from a water-accessible, high-polarity region adjacent to the lipid head groups ($n < n_0$) to a water-inaccessible, low-polarity region at the chain termini ($n > n_0$), occurring at $n = n_0$ and whose width is specified by λ .

The parameters resulting from the plots of figure 4.5 are listed in Table 4.1.

Comparing the solvent accessibility profile between the SSL and the DPPC bilayers, in SLL the limiting values for the $I(^2H)$ intensity are smaller with respect to

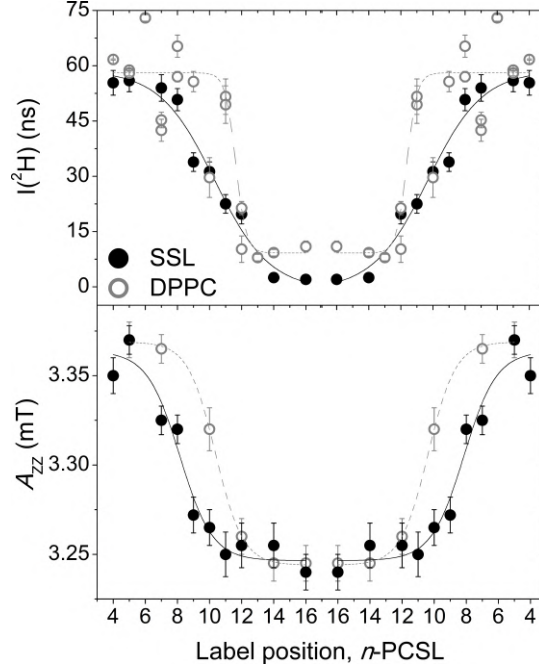


Figure 4.5: *Upper panel:* Profile of D₂O penetration from the deuterium spectral amplitude $I(^2\text{H})$ vs. label position, n , for n -PCSL in SSL (solid symbols) and DPPC liposomes (open symbols, from [17]). *Lower panel:* Polarity profile from outer hyperfine splitting A_{ZZ} vs. n for n -PCSL in SSL (solid symbols) and DPPC liposomes (open symbols, from [125]). Samples are fully hydrated in D₂O. Temperature = 77 K. Full and dashed lines represent nonlinear least-squares fits with equation (4.1). For better visibility of the water penetration and polarity profiles, the experimental data have been mirrored with respect to the bilayer midplane.

Table 4.1: Parameters describing the water accessibility (via $I(^2\text{H})$ -determinations) and polarity (via A_{ZZ} -determinations) profiles in figure 4.5 according to equation (4.1) in SSL of DPPC/PEG:2000-DPPE (2 mol%). For comparison, corresponding parameters for DPPC multibilayers are given in parenthesis.

<i>Water accessibility profile</i>	<i>Polarity profile</i>
$I(^2\text{H})_1 = 57.3 \pm 4.1$ ns	$A_{ZZ,1} = 3.36 \pm 0.01$ mT
(58.1 ± 3.4 ns)	(3.369 ± 0.001 mT)
$I(^2\text{H})_2 = -0.8 \pm 5.1$ ns	$A_{ZZ,2} = 3.25 \pm 0.01$ mT
(9.2 ± 5.1 ns)	(3.244 ± 0.001 mT)
$n_0 = 10.3 \pm 0.4$	$n_0 = 8.1 \pm 0.4$
(11.6 ± 0.3)	(10.37 ± 0.05)
$\lambda = 1.7 \pm 0.5$	$\lambda = 1.0 \pm 0.4$
(0.3 ± 0.2)	(0.85 ± 0.06)

those of DPPC bilayers and the lower extreme positions are less accessible to water in SSL than in DPPC multibilayers. The polarity profile, instead, exhibit A_{ZZ} limit-

ing values comparable between SSL and DPPC both at the first acyl chain segments and at the terminal ones. In addition, by analyzing both the deuterium intensity and the polarity profiles, it is evident that the transition from a water-accessible, high-polarity region at the polar/apolar interface to a water-inaccessible, low-polarity region at the chain termini occurs at a smaller n_0 in SSL than in DPPC, with $\lambda_{SSL} > \lambda_{DPPC}$ for both $I(^2\text{H})$ and A_{ZZ} . This lower cooperativity of the transition for the Stealth liposomes with respect to that of DPPC bilayers may be addressed to the reduced lamellar dimensions for the SSL (likely unilamellar) compared to that of DPPC liposomes (multilamellar) [126, 127].

4.1.2 Diacyl- and Lyso-lipids mixtures

Lyso-phosphocholines are single chain lipids present in mammalian cell membranes and in subcellular organelles. They are involved in various physiological and pathological processes [71–73], and at low content they are essential component of thermosensitive liposomes used in drug-delivery [81, 82]. Moreover, it has been evidenced that they impact on the stability, permeability and molecular properties of lipid membranes [74–80]. We have investigated the entire composition range (0 – 100 mol%) of lyso-palmitoylphosphatidylcholine (Lyso-PPC) (figure 4.6) in DPPC bilayers fully hydrated in D_2O by applying three-pulse D_2O -ESEEM to lipid mixtures spin-labeled with 5- and 16-PCSL.

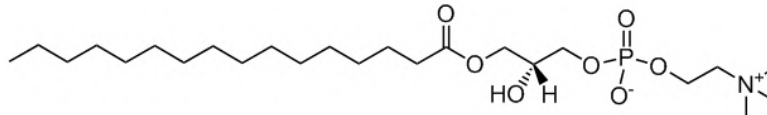


Figure 4.6: Chemical structure of single-chain lipid Lyso-PPC.

Figure 4.7 shows the experimental decays for 5- and 16-PCSL in DPPC/Lyso-PPC mixtures at selected concentration of Lyso-lipids, fully hydrated in D_2O . The D_2O -ESEEM decays for 5-PCSL show the typical superposition of rapid and slow modulations, while in the case of 16-PCSL the slow ^2H -modulations are absent in DPPC bilayers and show up with the lowest Lyso-PPC content.

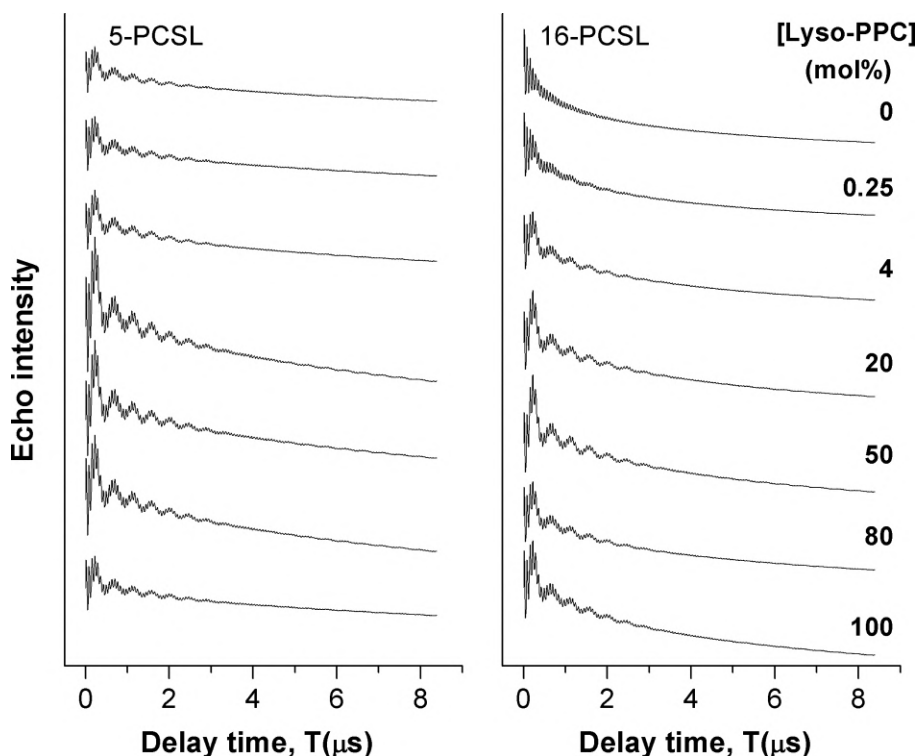


Figure 4.7: Decay curves at 77 K of the three-pulse electron spin echo amplitude with interpulse spacing, T , for (*left panel*) 5-PCSL and (*right panel*) 16-PCSL in mixtures of DPPC and selected concentration of Lyso-PPC hydrated in D_2O .

Figure 4.8 shows frequency ESEEM spectra for the same samples in figure 4.7. For 5-PCSL, both in the absence and in the presence of Lyso-PPC, there is an evident 2H signal at the characteristic Larmor frequency 2.5 MHz. Up to 50 mol% Lyso-PPC the signal intensity increases, then, at the higher concentrations, it decreases slowly but it is always present. For 16-PCSL, the 2H signal is absent in the DPPC sample and appears even with the lowest content of the single chain lipids.

In order to quantify the effects of Lyso-PPC, $I(^2H)$ for 5- and 16-PCSL in DPPC/Lyso-PPC mixtures are reported in figure 4.9. Again, as expected, in DPPC bilayers (0 mol% Lyso-PPC) at the first methyl segments of the hydrocarbon region, probed by 5-PCSL, there is an evident 2H -peak, whereas in the inner hydrocarbon region at the bilayer midplane, probed by 16-PCSL, the deuterium signal is absent, in agreement with previous results [17, 128, 129].

It is evident that the deuterium signal of 5-PCSL increases when the Lyso-PPC content increases from 0.25 mol% up to 7 mol% and then more slowly, reaching a plateau value at 20 mol%. This is due to the expansion in the area per polar head consequent to the insertion of the single chain lipids in DPPC. A value approximately constant is maintained until the Lyso-PPC concentration is of about 70 mol%, then

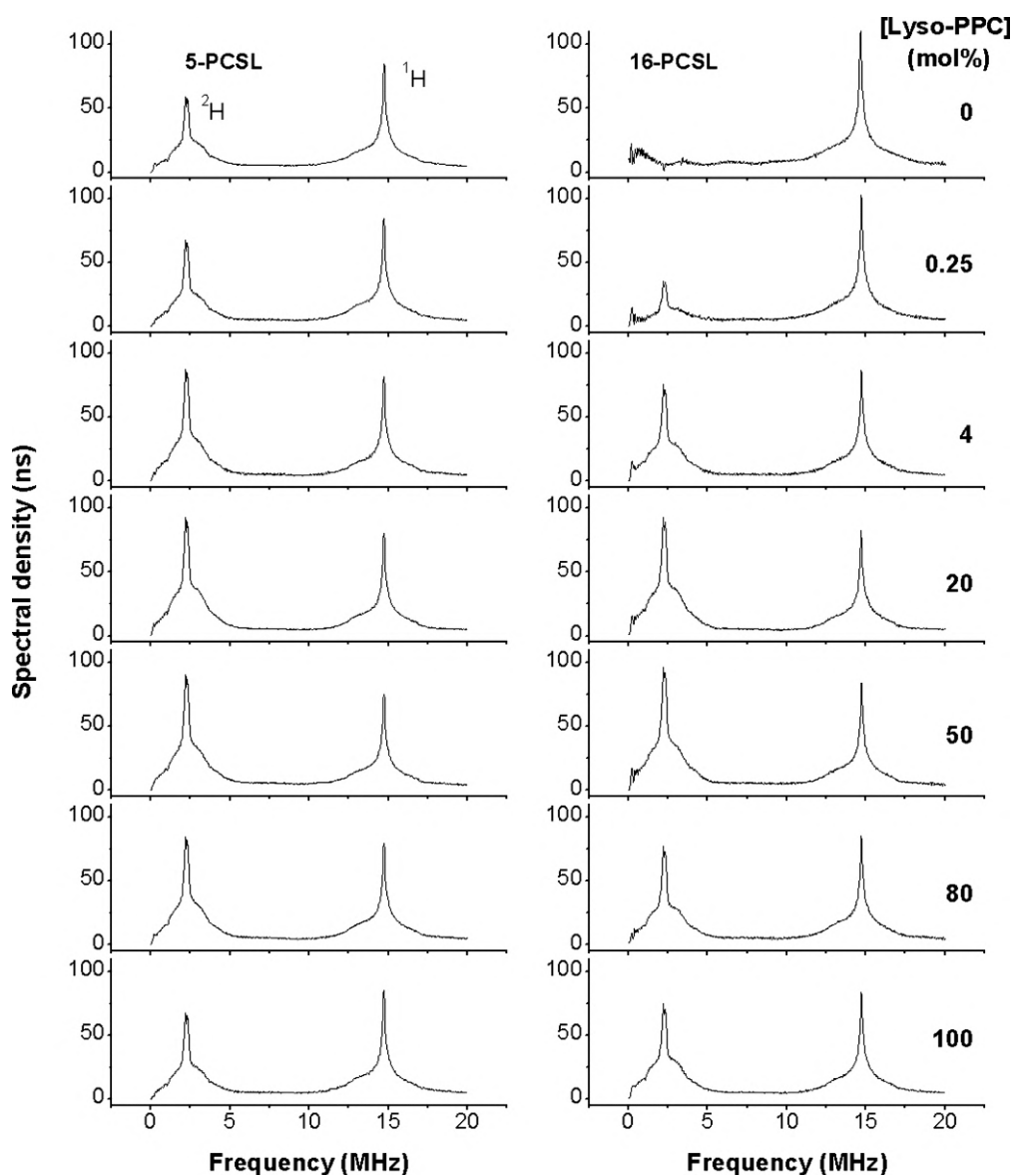


Figure 4.8: Fourier Transform ESEEM spectra at 77 K for (*left panel*) 5-PCSL and (*right panel*) 16-PCSL in mixtures of DPPC and selected concentration of Lyso-PPC hydrated in D_2O .

$I(^2\text{H})$ progressively decreases reaching in micelles of pure Lyso-PPC a value slightly higher than that recorded in DPPC bilayers. An analogous pattern is recorded in the case of 16-PCSL. Indeed, from figure 4.9 it can be seen a rapid increase in $I(^2\text{H})$ intensity up to 20 mol% of Lyso-PPC. Solvent penetration even in the deepest hydrophobic interior of the bilayers indicates that the apolar groups are transferred to the solvent and a change in the chain packing is occurring. Then, a constant value up to 70 mol% of Lyso-PPC content is maintained. For Lyso-PPC content equal to 80 mol% there is just a small decrease and then the reached intensity remains

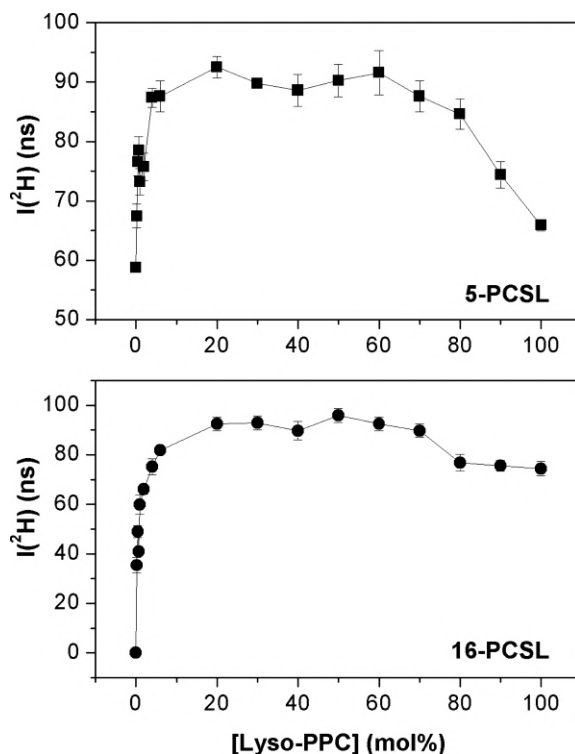


Figure 4.9: Dependence on Lyso-PPC concentration of the deuterium spectral amplitudes, $I(^2\text{H})$, at 77 K for 5-PCSL (squares) and 16-PCSL (circles) in DPPC/Lyso-PPC mixtures hydrated in D_2O .

constant up to the formation of Lyso-PPC micelles. The two labeling positions, therefore, show a similar behavior over a wide concentration range up to about 60 mol% of Lyso-PPC. Instead, they differ at the highest concentrations, where for 5-PCSL samples show deuterium intensity progressively smaller while for 16-PCSL $I(^2\text{H})$ maintains high values.

The constant and similar intensity for both labeling positions at intermediate Lyso-content, between 20 mol% and 60 mol%, indicates that two different lamellar phases coexist: a bilayer organization and an organization with interdigitated chains. A fully interdigitated lamellar phase is reported to occur in mixtures of DPPC and 40 mol% of Lyso-PPC [80]. In the presence of chains interdigitation, the two isomers 5-PCSL and 16-PCSL probe the same hydrocarbon region at the polar/apolar interface and therefore they give a comparable $I(^2\text{H})$ intensity. When Lyso-lipids are at about the 70 mol% of the total lipid composition, micelles begin to appear and the solvent permeates deeper in the hydrocarbon chain region, otherwise inaccessible in DPPC bilayers.

EPR results on interdigitated phases formed by equimolar content of DPPC and Lyso-PPC or by DPPC hydrated in ethanol containing D_2O (60% v/v), and micellar

assemblies of Lyso-PPC or PEG:2000-DPPE are given below.

4.2 Interdigitated lamellar phases

Cw- and D_2O -ESEEM measurements at 77 K have been carried out on a variety of cryogenically frozen chain-labelled samples with interdigitated chains, namely DPPC/Lyso-PPC and DPPC/etOH. X-ray diffraction measurements have evidenced that these systems are interdigitated in the gel phase [77, 78, 83, 130, 131].

We focused our attention on the interdigitated DPPC/Lyso-PPC mixture, labeled at the carbon atom positions $n = 5, 7, 8, 9, 10, 11, 12, 14$ and 16. The cw-EPR spectra in figure 4.10, although exhibiting spin-spin broadening, particularly evident for labeling positions in the middle of the chains, are powder patterns of similar lineshape and outermost peak separation, with a broad first resonance of Voigtian character. The line broadening is likely due to a possible increase of local concentration of nitroxide spin-labels [132, 133].

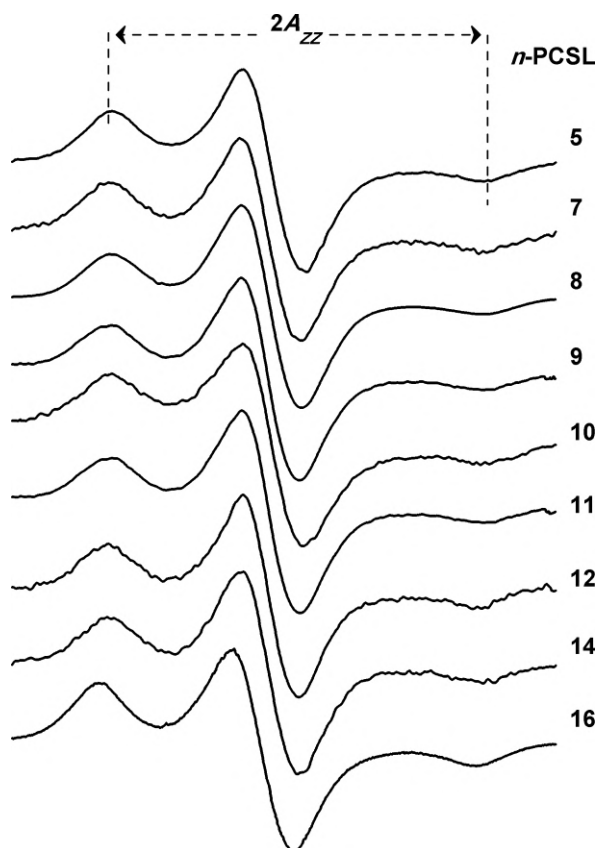


Figure 4.10: Cw-EPR spectra of n -PCSL spin-labels in interdigitated DPPC/Lyso-PPC dispersions fully hydrated in D_2O . Central field = 332.5 mT, spectral width = 10 mT. Temperature = 77 K.

The transmembrane polarity profile in the interdigitated DPPC/Lyso-PPC equimolar mixture delineated by $2A_{ZZ}$ as a function of n in figure 4.11 is uniform and of elevated polarity, with $2A_{ZZ}$ values typical of the polar hydrophobic environment of different lipid lamellae [129, 134, 135]. Moreover, the $2A_{ZZ}$ dependence on n is similar to the one reported for dialkyl-lipid DHPC, which spontaneously interdigitates through the gel phase [136]. Thus, the presence of Lyso-PPC in 1:1 mol/mol ratio with respect to the bilayer-forming lipid DPPC abolishes the DPPC typical sigmoidal polarity profile, favoring the exposure of the entire hydrocarbon chain to a more polar environment.

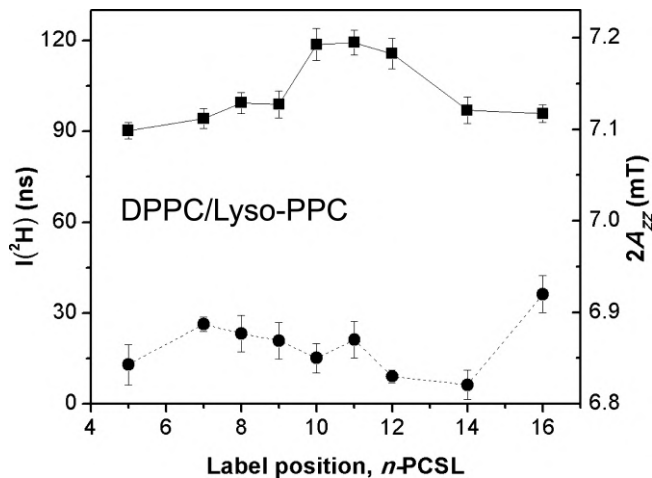


Figure 4.11: Dependence on spin-label position, n , of the deuterium spectral amplitude, $I(^2\text{H})$ (solid line and left-hand scale), and of the outermost peak separation, $2A_{ZZ}$ (dashed line and right-hand scale), for spin-labeled phosphatidylcholine n -PCSL in interdigitated lamellar dispersions of DPPC and 50 mol% Lyso-PPC hydrated in D_2O . Temperature = 77 K.

Figure 4.11 reports also the dependence of the ^2H -ESEEM intensity as a function of the chain labeling position. The profile of solvent access through the hydrocarbon region mirrors the polarity profile, confirming that both the positional isomers at the beginning of the hydrocarbon chains and those at the terminal ends experience a similar polar environment and are all exposed to the solvent in the interdigitated phase. The upper region of the hydrocarbon chains (probed by 5-9-PCSL) and the inner segments (probed by 14- and 16-PCSL) show comparable values, with $I(^2\text{H}) \approx 90$ ns. The intermediate region (probed by 10-12-PCSL) exhibits, instead, a higher solvent penetration. A similar outline of the $I(^2\text{H})$ values is exhibited by the spontaneously interdigitated DHPC [136]. It is worthy to note that the deuterium intensities here reported for the interdigitated samples of DPPC with 50 mol% of Lyso-PPC are greater than those for DPPC bilayers and are comparable to those that have been previously recorded in DPPC bilayers with equimolar content of

cholesterol. The steroid, spacing apart the polar heads as the Lyso-lipids do, allows a considerable solvent penetration in the hydrocarbon region [17].

An interdigitated lamellar phase in DPPC is formed not only with the insertion of micelle-forming lipids with a single hydrocarbon chain (Lyso-PPC) but also for the effect of solvents. For instance, ethanol at the threshold concentration of 50 mg/ml in aqueous buffer is able to induce interdigitation in DPPC [130,131].

Figure 4.12 shows the decay curves (on the left) and the corresponding Fourier transforms (on the right) of the three-pulse D_2O -ESEEM experiment for 5- and 16-PCSL in interdigitated DPPC in the presence of ethanol (60% v/v) in the D_2O hydration buffer. As expected, both positional isomers exhibit decay curves characterized by the superposition of both the rapid modulation due to the proton and the slow modulation due to the presence of deuterons, confirming the exposure to the solvent even of the terminal methyls of the hydrocarbon chains. Indeed, comparing the two signal in the frequency domain on the right side of figure 4.12, the 2H signal presents a high value comparable between the two labeling sites, being 89 ns for 5-PCSL and 101 ns for 16-PCSL. This confirms the transfer of the inner apolar groups to the solvent upon the formation of the interdigitated phase, due to the presence of the external inducer ethanol.

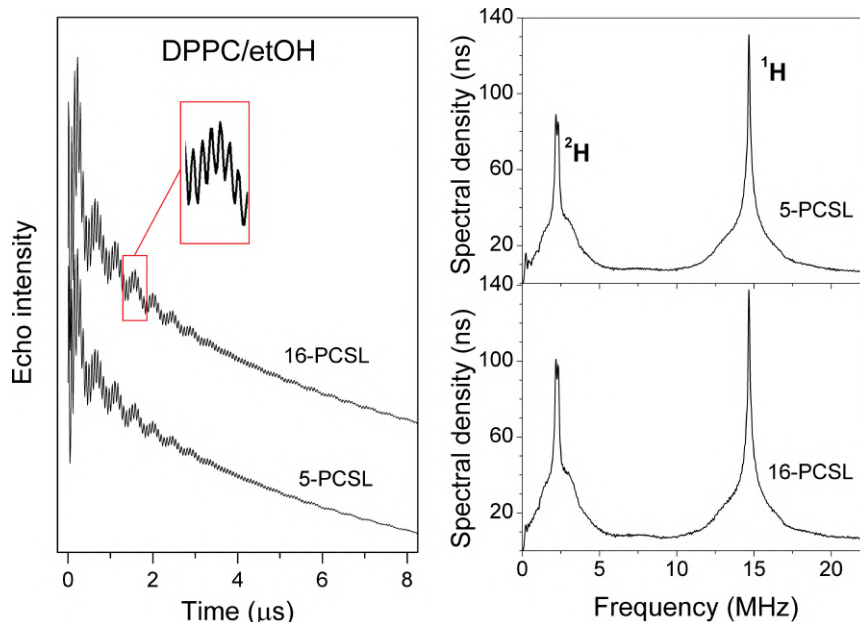


Figure 4.12: *Left panel:* Decay curves of the three-pulse electron spin echo amplitude with interpulse spacing, T , for 5-PCSL and 16-PCSL in DPPC hydrated in $etOH$ and D_2O . *Right panel:* Fourier Transform ESEEM spectra for samples as in the left panel. Temperature = 77 K.

These results are characteristic hallmarks of chain interdigitation and are in

agreement with previous findings of the ^2H -ESEEM intensity dependence on the spin-labeling position along the chain in DPPC/Lyso-PPC (50 mol%), presented in figure 4.8, and in DHPC dispersions in the frozen state [136], which have shown that all the methylene segments are accessible to the solvent to a similar extent and are of elevated polarity. In particular, $I(^2\text{H})$ resulted to be 90 ns (96 ns) in DPPC/Lyso-PPC and 129 ns (144 ns) in DHPC for 5-PCSL (16-PCSL). On the contrary, in the case of DPPC bilayers with and without cholesterol the water extent at the 5-PCSL probed region is, respectively, 121 ns and 59 ns, while the bilayer midplane probed with 16-PCSL is devoid of water in both matrices. Lipid bilayers are characterized by a sigmoidal transmembrane polarity profile that is, instead, suppressed in the interdigitated samples [17, 53, 100, 128].

According to theory presented in Section 2.6.2, by evaluating the intensity of the broad component from the Fourier transformed D_2O -ESEEM signal and by applying equation (2.40) and equation (2.41), the nitroxide moieties singly, f_{1w} , and doubly, f_{2w} , hydrogen bonded to the deuterium molecules can be calculated. Figure 4.13 reports a comparison of the fractions between interdigitated and non interdigitated samples, i.e., DPPC/Lyso-PPC, DPPC/etOH and DHPC, and bilayers of DPPC and DPPC with equimolar content of cholesterol.

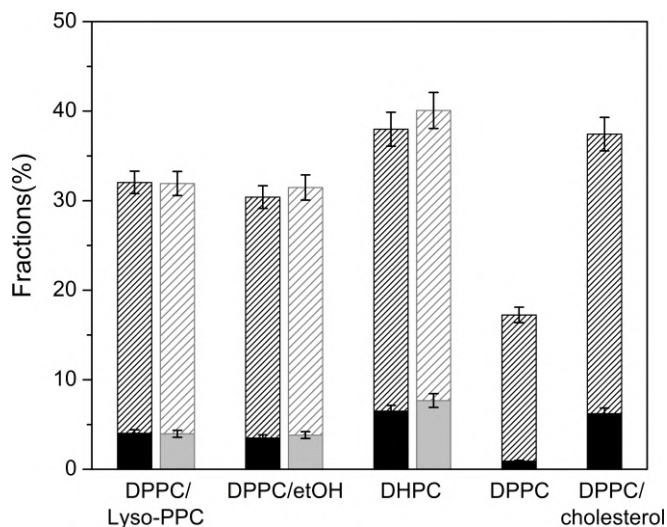


Figure 4.13: Fractions of 5- (black) and 16-PCSL (gray) hydrogen bonded by one, f_{1w} (shaded), or two, f_{2w} (full), water molecules from D_2O -spectra of DPPC/Lyso-PPC, DPPC/etOH interdigitated samples and, for comparison, for DHPC interdigitated dispersions (from [136]) and DPPC and DPPC/cholesterol noninterdigitated bilayer dispersions (from [17]).

In all samples in figure 4.13, the fraction of single H-bonded spin-labels to the D_2O molecules is greater than that of the double H-bonded ones, suggesting heterogeneity in the structure of water surrounding the nitroxides. Moreover, the in-

crease in the area per polar head due to the presence of external components in the DPPC lamellae enhances the solvent penetration at the C5 (black columns in the bar chart) position with respect to pure DPPC bilayers. In particular, for 5-PCSL the presence of cholesterol increases solvent penetration with respect to DPPC and the extent of bounded nitroxides is comparable to the spontaneously interdigitated DHPC. The other two interdigitated samples present almost equal values for f_{1w} and f_{2w} and these values are lower compared to the DHPC and DPPC/cholesterol ones. For 16-PCSL, instead, solvent accessibility occurs only in the three interdigitated samples, while in the noninterdigitated ones the midplane is inaccessible to water. Analogously to 5-PCSL, also for the 16-PCSL samples the order is $f(\text{DHPC}) > f(\text{DPPC/Lyso-PPC}) \approx f(\text{DPPC/etOH})$. Thus, the two interdigitation inducers, ethanol and Lyso-PPC, contribute similarly to the enhancement of the solvent penetration to all chain segments of the hydrocarbon chain, but the extent of solvent accessibility is lower with respect to that in the lamellar phase of the DHPC lipids that spontaneously interdigitate. Moreover, the two inducers confer different properties to the interdigitated phase, with the chains resulting less densely packed in the presence of ethanol than in the presence of Lyso-lipids.

4.3 Micellar phases

Two micelle dispersions, namely those formed by Lyso-PPC or PEG:2000-DPPE hydrated in D₂O, have been also studied and compared.

Cw-EPR spectra recorded at 77 K in spin-labeled micelles of Lyso-PPC or PEG:2000-DPPE at full hydration for various n -PCSL isomers are shown in figure 4.14. Although they present some extent of spin-spin broadening, their lineshapes indicate that the spin-labelled lipids are randomly and well distributed within the host lipid aggregates. All the spectra are powder patterns typical of immobilized nitroxides on the EPR time scale.

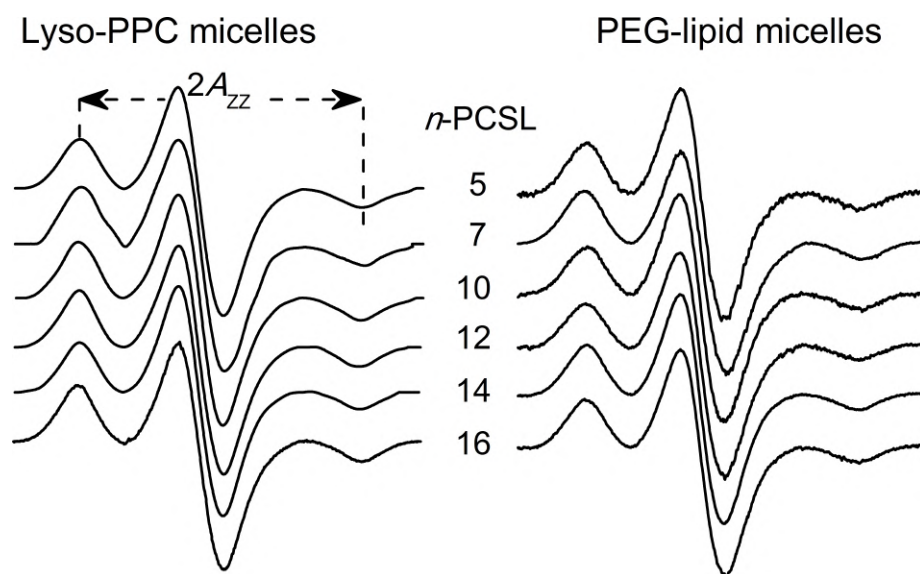


Figure 4.14: Cw-EPR spectra at 77 K of selected n -PCSL spin labels in micelles of (*left*) Lyso-PPC and of (*right*) PEG:2000-DPPE, fully hydrated in D_2O . Central field = 330 mT, spectral width = 10 mT.

Figure 4.15 and figure 4.16 show for Lyso-PPC micelles and PEG:2000-DPPE micelles, respectively, both the $I(^2H)$ signal intensity of the D_2O -ESEEM spectra and the outer hyperfine separation $2A_{ZZ}$ from the cw-spectra as a function of the labeling position.

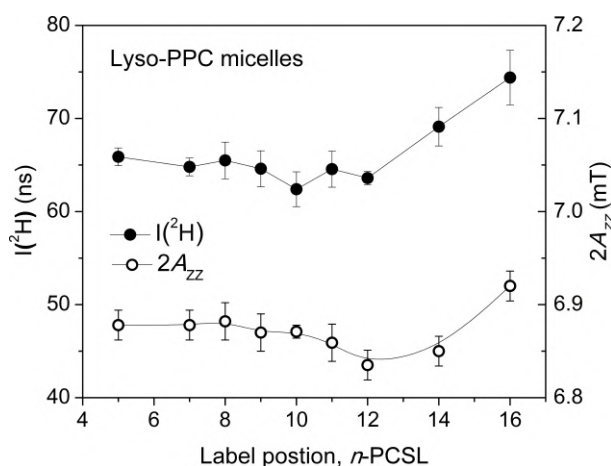


Figure 4.15: Dependence on spin label position, n , of the deuterium spectral amplitude, $I(^2H)$ (full symbols and left-hand scale), and of the outermost hyperfine splitting, $2A_{ZZ}$ (open symbols and right-hand scale), in Lyso-PPC micelles at 77 K.

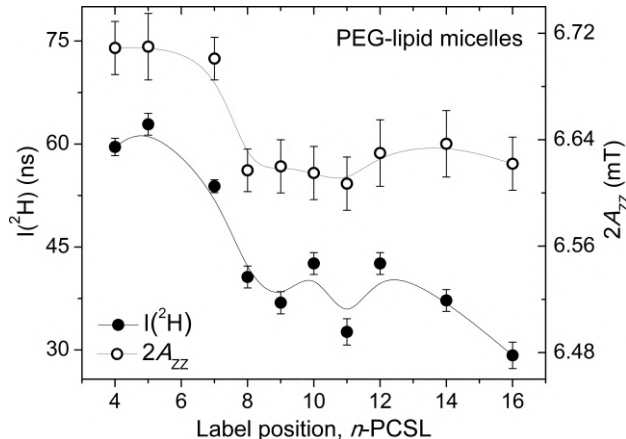


Figure 4.16: Dependence on spin label position, n , of the deuterium spectral amplitude, $I(^2\text{H})$ (full symbols and left-hand scale), and of the outermost hyperfine splitting, $2A_{ZZ}$ (open symbols and right-hand scale), in PEG:2000-DPPE micelles at 77 K.

The $I(^2\text{H})$ values for Lyso-micelles are higher at any labeling position with respect to the values for PEG-micelles. Moreover, while the deuterium intensity maintains a constant value in Lyso-PPC micelles from the first chain segments to the middle of the chain ($n = 12$) and then progressively increases up to $n = 16$, in PEG:2000-DPPE micelles the high value recorded at the beginning of the acyl chain abruptly reduces of about one-third at the $n = 8$ position and then oscillates around this value until the $n = 16$ position, where, again, there is a decrease.

Correspondingly, the $2A_{ZZ}$ values are higher in Lyso-PPC micelles than in PEG:2000-DPPE micelles. In the first sample, the hyperfine separation maintains approximately a constant value in the positional range $n = 5 - 14$ and then a greater value for 16-PCSL. In the second sample, instead, mirroring the $I(^2\text{H})$ profile, the first acyl methylene segments, $n = 4 - 7$, have a high $2A_{ZZ}$ -value, which drops at intermediate chain position, $n = 8 - 11$, and then increases a little from the $n = 12$ to $n = 16$ labeling position.

The results obtained in both types of micelles suggest that each region of the hydrocarbon tails is accessible to water, reflecting the conformational disorder of the chains both in small micelles of single chain lipids and in large pegylated micelles. In particular, the $I(^2\text{H})$ and the $2A_{ZZ}$ -values determined in frozen Lyso-PPC micelles are in the same range of variability of those previously reported for the upper apolar region in frozen DPPC bilayers [17, 129, 134]. Moreover, the polarity profiles established with cw-EPR in frozen Lyso-PPC micelles and in frozen pegylated micelles are also comparable to the profile recorded with cw-EPR in the same lipid matrices in the fluid phase at 323 K [137] and to two-pulse D_2O -ESEEM data in the time

domain for 5-, 7- and 10-doxyl stearic acid in small micelles of dodecyl sulphate, which indicated water penetration at any depth in their hydrophobic zone [138].

Figure 4.17 shows the fractions of nitroxides singly, f_{1w} , and doubly, f_{2w} , bonded to the deuterium molecules for selected n -PCSL inserted in micelles of Lyso-lipids and PEG-lipids, evaluated from equations (2.40) and (2.41).

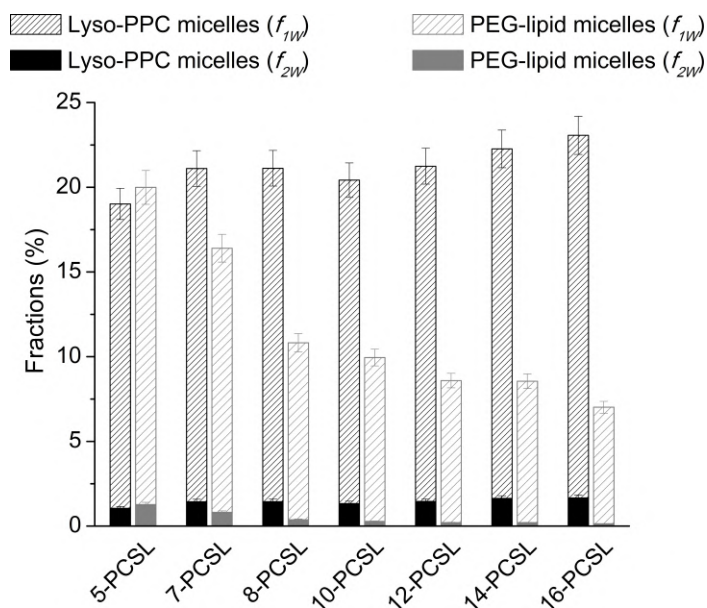


Figure 4.17: Fractions selected n -PCSL hydrogen bonded by one, f_{1w} (shaded), or two, f_{2w} (full), water molecules in micelles of Lyso-PPC (black) and PEG:2000-DPPE (gray).

In any sample, some spin-labels do not have water molecules bonded, other are H-bonded to one water molecule, a small part is H-bonded to two water molecule, with $f_{1w} > f_{2w}$ at each labeling position. Therefore, heterogeneity is present in the structure of the solvent penetrating from the first acyl segments to the terminal ones. Specifically, the fractions of bounded nitroxides are higher in Lyso-PPC micelles than in PEG-micelles almost at every labeling position, maintaining high values close to each other. Instead, in PEG-micelles the fractions of bounded nitroxide moieties are progressively smaller on going down along the chain. The high values at the polar/apolar interface are comparable with the one reported in the bar chart of figure 4.13, but also with the values reported for other type of lipid aggregates, including membranes and model lipid bilayers [17, 139].

4.4 Membrane protein: the case of Na^+, K^+ -ATPase

The Na^+, K^+ -ATPase (figure 4.18), or sodium pump, is a complex of three integral membrane proteins, which plays a central role in the homeostasis of animal cells. The sodium pump is also the primary pharmacologic receptor for cardiotonic steroids (CTS). The binding site of CTS overlaps with that for ions. Here we present EPR results, both cw-EPR and D_2O -ESEEM, aimed to characterize the extracellular binding site in the sodium pump. This is done by using spin-label bufadienolides, a subgroup of cardiotonic steroids with anticancer activity. Specifically, bufalins and cinobufagins with five- (i.e., PROXYL) and six-membered (i.e., TEMPO) nitroxide ring, which are specific inhibitors for the sodium pump, have been used. This work is the result of a fruitful collaboration with a group from Aarhus University in Denmark (professor Natalya U. Fedosova) and a group from Jinan University in China (professor Ren-Wang Jiang).

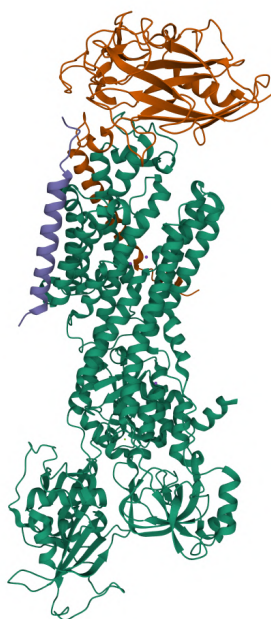


Figure 4.18: Crystal structure of Na^+, K^+ -ATPase (PDB ID 4RES [140]).

Figure 4.19 shows structures of seven synthesized bufalin EPR probes and the corresponding cinobufagin ones for three of them, having different lengths of the spacer arm between the EPR-active nitroxide group and the steroid core, thus determining different positioning of the spin-labels in the binding cavity.

Pairwise samples containing the competitor ouabain discriminates between specific and non-specific interactions [141]. Indeed, ouabain blocks the pump, when it occupies the extracellular binding site a conformational change happens in the pump

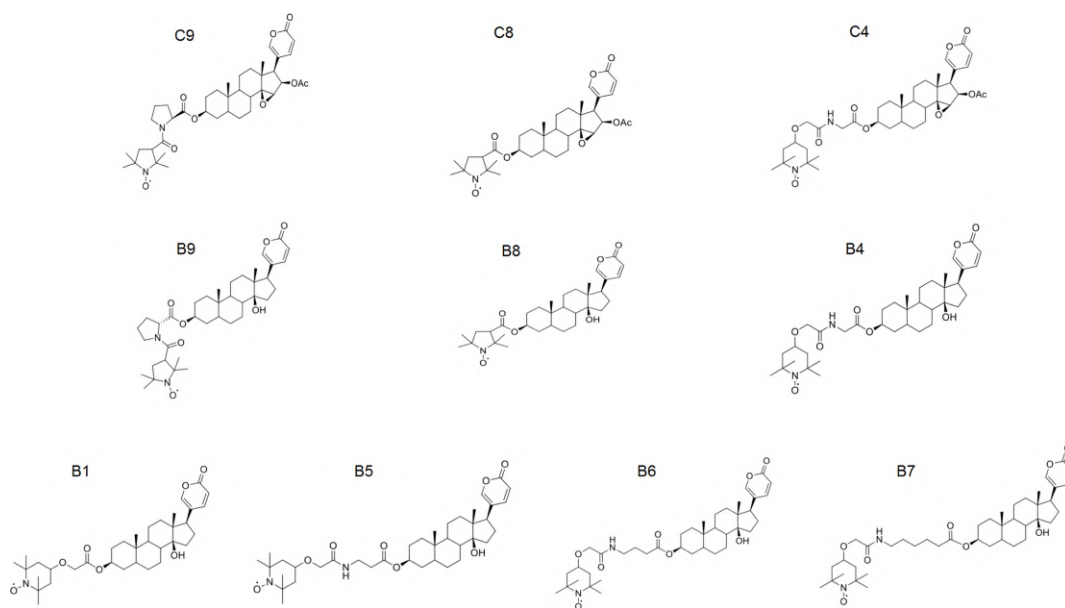


Figure 4.19: Structures of spin-labeled cinobufagins (C) and bufalins (B).

and the pharmacological effect in the treatment of cardiac tissues is stabilized. Thus, the presence of ouabain does not allow the spin-label cardiotonic steroids to access the binding site in Na^+, K^+ -ATPase, remaining, instead, in the membrane environment.

Figure 4.20 shows the outer hyperfine splitting $2A_{ZZ}$ -values evaluated from cw-EPR spectra recorded in the frozen state at 77 K for the various CTS labels.

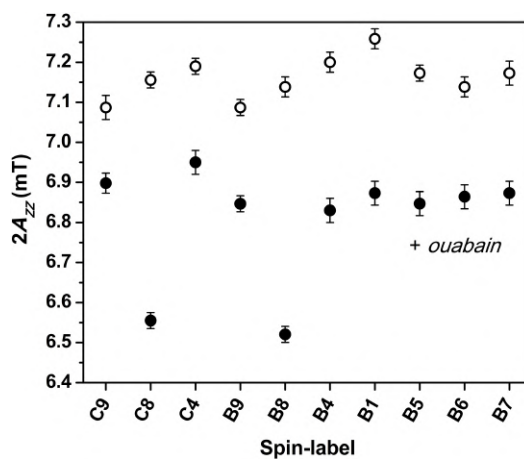


Figure 4.20: Outer hyperfine splitting, $2A_{ZZ}$, in the cw-EPR spectra of different spin-labeled cinobufagins and bufalins in Na^+, K^+ -ATPase membranes in the absence (open symbols) and presence (solid symbols) of ouabain. Temperature = 77 K.

It can be seen that in the absence of ouabain, the spin-labels access the binding site and experience a high polarity environment ($2A_{ZZ} \approx 7.1 - 7.2$ mT). In the presence of excess ouabain, instead, the values are always lower, with the greatest difference presented by the pair C8-B8, the shortest cardiotonic steroids.

By means of three-pulse ($\pi/2 - \tau - \pi/2 - T - \pi/2 - \tau - echo$) D_2O -ESEEM experiment, the water accessibility in the entrance cavity of Na^+,K^+ -ATPase was compared for the different CTS spin-labels. In figure 4.21 are shown representative measurements for the bufalin B7 cardiotonic steroid spin-label in Na^+,K^+ -ATPase without and with the inhibitor ouabain.

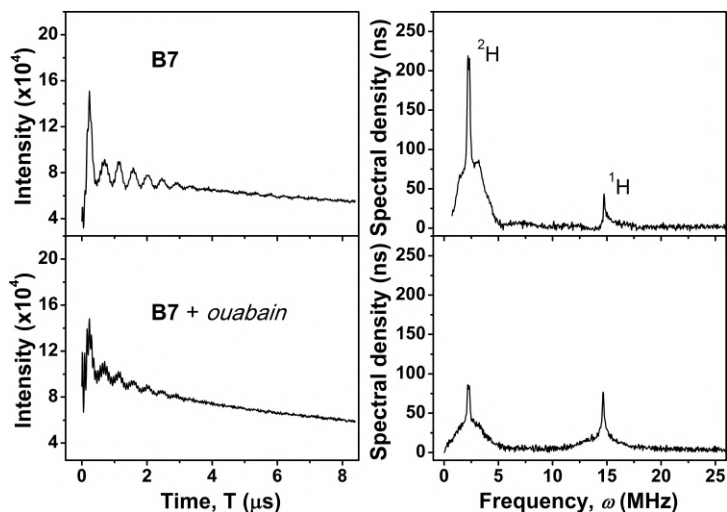


Figure 4.21: *Left-hand side:* decay curves of the three-pulse electron spin echo amplitude with interpulse spacing, T , for spin-labeled bufalin B7 in Na^+,K^+ -ATPase membranes hydrated in D_2O . *Right-hand side:* Fourier-Transform ESEEM spectra for samples as in the left panel. Temperature = 77 K.

The decay curves for B7 and B7 + ouabain exhibit some differences: the first one shows deeper slow modulations with period of $0.4 \mu s$ due to the dipolar interaction of the nitroxide with the surrounding deuterium nuclear spins and small rapid modulations with period $0.07 \mu s$ due to interactions of the nitroxide with the nearby protons; the second one presents a fast decay with deep rapid oscillations occurring during the slowest oscillations. These differences are better seen in the frequency domain spectra where the Fourier transform for the B7 sample exhibits an intense deuterium peak at the Larmor frequency 2.5 MHz of about 220 ns and a smaller proton peak at the Larmor frequency 14.5 MHz of about 50 ns. In the case of its pairwise, B7 + ouabain, a reduced 2H signal of about 90 ns and a 1H intensity peak of about 80 ns are recorded.

Figures 4.22 and 4.23 show the other spin-label cardiotonic steroids decays and Fourier transform without and with ouabain, respectively.

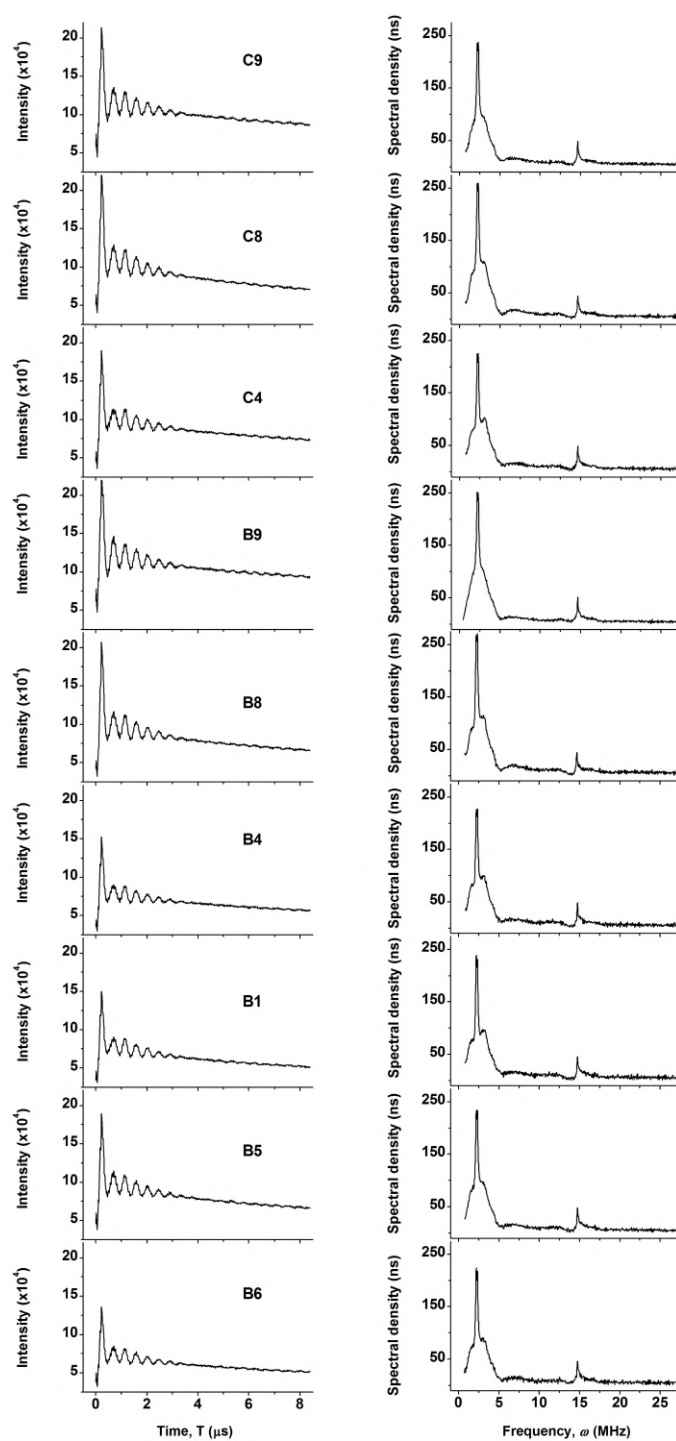


Figure 4.22: *Left-hand side:* decay curves of the three-pulse electron spin echo amplitude with interpulse spacing, T , for spin-labeled bufalins and cinobufagins in the absence of ouabain in Na^+, K^+ -ATPase membranes hydrated in D_2O . *Right-hand side:* Fourier-Transform ESEEM spectra for samples as in the left panel. Temperature = 77 K.

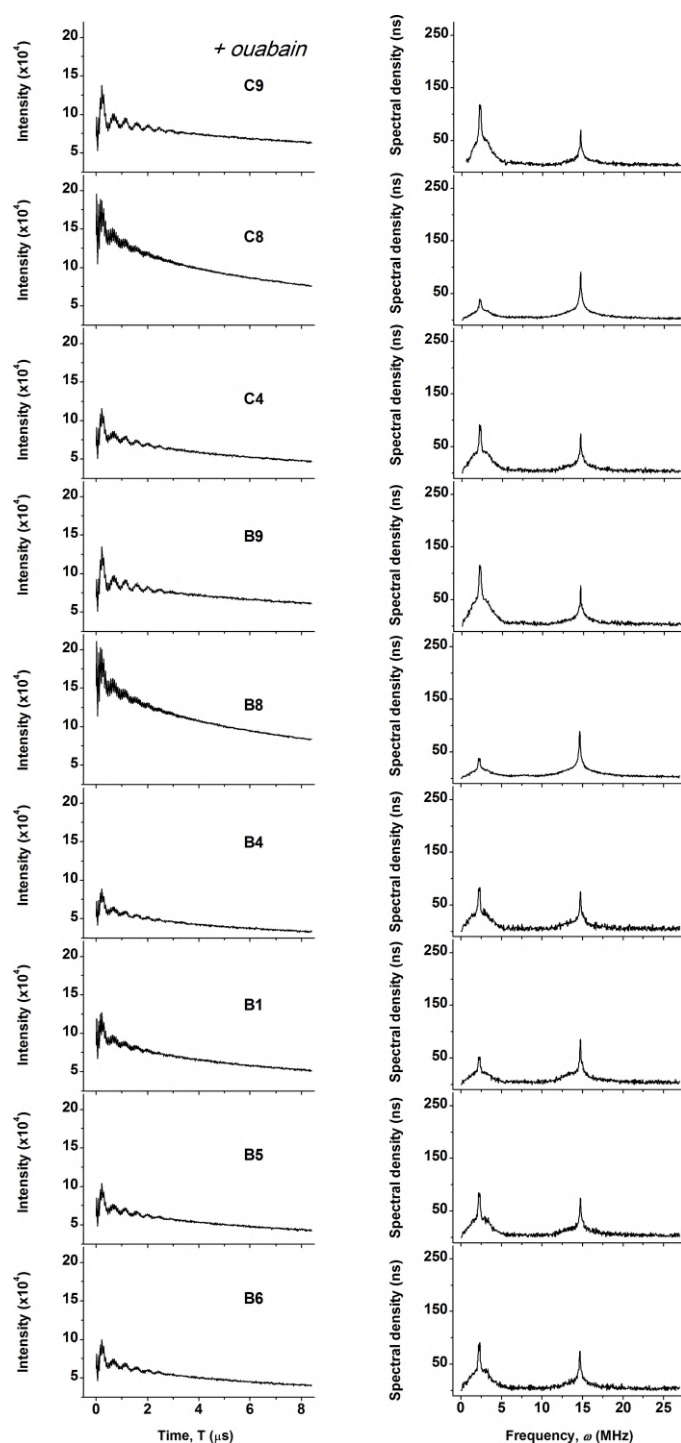


Figure 4.23: *Left-hand side:* decay curves of the three-pulse electron spin echo amplitude with interpulse spacing, T , for spin-labeled bufalins and cinobufagins in the presence of ouabain in Na^+, K^+ -ATPase membranes hydrated in D_2O . *Right-hand side:* Fourier-Transform ESEEM spectra for samples as in the left panel. Temperature = 77 K.

A summary of the ESEEM results collected on all investigated samples is given in figure 4.24. Both the total intensity, I_{tot} , and the broad component due to the spin-label nitroxides H-bonded to deuterium molecule, I_{broad} , of the ^2H signal are shown.

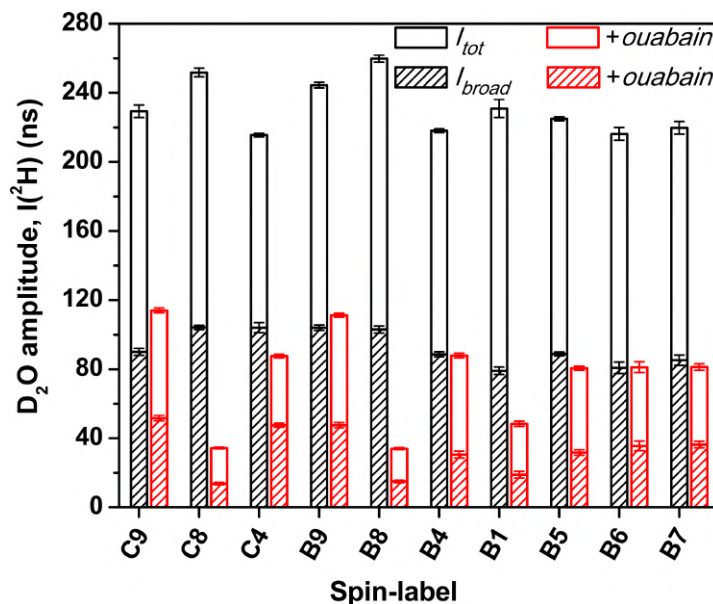


Figure 4.24: Intensity of the total D₂O-peak, I_{tot} (plain), and its broad component, I_{broad} (shaded), in ESEEM spectra of different spin-labeled cinobufagins and bufalins in Na⁺,K⁺-ATPase membranes in the absence (black) and in the presence (red) of ouabain. Temperature = 77 K.

It is evident that all the CTS sampling the channel cavity of the sodium pump experience a water accessible environment, while the spin-labeled steroids whose access to the cavity is blocked by ouabain are located in a membrane environment with less water penetration. Moreover, the ratio of broad to narrow components is similar in the presence and absence of ouabain, reflecting a similar H-bonding equilibrium in the binding site to that in the membrane. There is, also, correspondence in the ratio between the intensity in the presence of ouabain and in its absence for cinobufagins and corresponding bufalins. Indeed, for the pair C8 and B8 there is the highest intensity without ouabain and the lowest intensity with ouabain. That is because this CTS pair has the shortest spacer, thus in the presence of ouabain the location is in the deepest hydrophobic membrane interior.

The high I(²H)-values recorded when the spin-labels access the sodium pump cavity are comparable to those found for spin-labels attached to surface -SH groups on the Na⁺,K⁺-ATPase as well as on other proteins [31, 36, 142]. In the presence of ouabain, instead, the I(²H) intensities for spin-labels in the membrane are compa-

rable to those reported in figure 4.11 for interdigitated DPPC/Lyso-PPC mixtures and for interdigitated DPPC/etOH, and also to those of lipids spin labelled at the $n = 6 - 8$ chain position ($n = 9 - 10$ for the short-linked B8 and C8) [136, 139].

Table 4.2 summarizes the results regarding solvent properties at the entrance of the hydrophilic binding site in Na^+, K^+ -ATPase (for samples in the absence of ouabain) and in the lipid membrane environment (for samples in excess ouabain). Fractions of singly, f_{1w} , and doubly, f_{2w} , H-bonded nitroxides belonging to the cardiotonic steroids to the solvent as well as the product of equilibrium constant for hydrogen bonding, K , and effective concentration of free water, $[W]$, $K[W]$, are listed. They have been calculated by applying equations (2.38), (2.40) and (2.41).

Table 4.2: Product of equilibrium constant for H-bonding, K , with effective free water concentration, $[W]$, from ^2H -ESEEM spectra of cinobufagin and bufalin spin-labels from Na^+, K^+ -ATPase membrane dispersions in D_2O , and fractions of spin-labels that are hydrogen bonded by one (f_{1w}) and two (f_{2w}) water molecules. Data with (+ ou) and without ouabain are given.

Sample	$K[W]$	f_{1w}	f_{2w}	+ ou $K[W]$	+ ou f_{1w}	+ ou f_{2w}
C9	0.652	0.478	0.156	0.293	0.350	0.051
C8	0.841	0.496	0.209	0.064	0.113	0.004
C4	0.625	0.473	0.148	0.182	0.260	0.024
B9	0.839	0.496	0.208	0.263	0.330	0.043
B8	0.823	0.495	0.204	0.070	0.123	0.004
B4	0.635	0.475	0.151	0.154	0.232	0.018
B1	0.531	0.453	0.120	0.090	0.152	0.007
B5	0.638	0.476	0.152	0.161	0.240	0.019
B6	0.548	0.457	0.125	0.185	0.263	0.024
B7	0.597	0.468	0.140	0.190	0.268	0.025

In all sample pairs, values of the $K[W]$ product are in the range 0.5 - 0.8 for spin-labeled cardiotonic steroids in the cavity and are much reduced, in the range 0.2 - 0.4, for those bound to the membrane but displaced from the cavity. Correspondingly, f_{1w} is higher than f_{2w} and both are higher for spin-labeled steroids in the binding site than in Na^+, K^+ -ATPase membrane dispersions.

The above cw and ESEEM data at 77 K combined with conventional EPR measurements carried out as a function of temperature in the interval 5 - 50 °C for the differing spin-labeled CTS allowed to describe the cavity at the extracellular entrance as large and water filled. Overall, the EPR results have also been confirmed by molecular modeling experiments. Details on the high-temperature dependent

cw-EPR and the docking experiments can be found in the recent publication by Aloi, Guo et al. in press for the Biophysical Journal [119].

Dynamics of lipid assemblies at cryogenic temperatures

Cw-EPR and two-pulse ED-spectra are used to characterize the librational dynamics of chain-labelled supramolecular lamellar aggregates in the temperature range 120 - 270 K. Bilayer phases composed of unsaturated lipids and interdigitated phases formed by saturated symmetrical chain lipids in the presence of a threshold concentration of monoacyl lyso-lipids or hydrated in ethanol containing buffer are considered. The motional parameter $\langle\alpha^2\rangle\tau_c$, given by the product of the mean-square angular amplitude of libration, $\langle\alpha^2\rangle$, and the correlation time of motion, τ_c , is detected from the pulse measurements, an independent evaluation of the angular amplitude of the motion is obtained from the conventional EPR measurements, and the rotational correlation time is calculated from a combination of both evaluations. Fast librational oscillations of small angular amplitude are detected in all the investigated samples. At a temperature within the 200 - 240 K interval, the onset of larger diffusive motion is observed in all biosystems and has been associated to the dynamical transition.

Results and discussion of the present Chapter are published in [117] and [143].

5.1 Librational dynamics of unsaturated bilayers

Glycerophospholipids with unsaturated hydrocarbon chains are abundant in animal cell membrane and are naturally present in eukaryotes. Representative lipids are palmitoyl-oleoyl-glycero-phosphocholine (POPC) and di-oleoyl-glycerophosphocholine (DOPC) (figure 5.1).

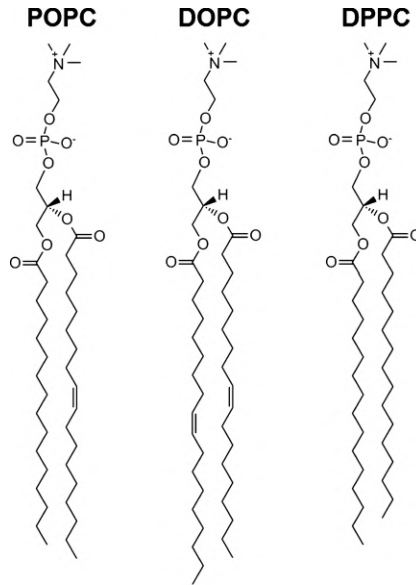


Figure 5.1: Chemical structure of the unsaturated phospholipids POPC and DOPC, and, for comparison, of the saturated phospholipid DPPC.

POPC is an asymmetric mixed-chain lipid composed by one unsaturated acyl chain with 18 carbon atoms at the *sn*-2 position and one saturated chain with 16 carbon atoms at the *sn*-1 position. DOPC consists of two chains with 18 carbon atoms and with one unsaturated bond in each of them. For the presence of double bonds along the chains, bilayers composed of POPC or DOPC are low- T_m bilayers. Indeed, the main phase transition temperature, T_m , occurs at 271 K for the monounsaturated POPC bilayers and at 253 K for the di-unsaturated DOPC [85]. For comparison, DPPC, which presents two saturated symmetrical chains with 16 carbon atoms, has T_m at 314 K.

For their low- T_m values, POPC and DOPC bilayers are fluid over a large temperature range, including the physiological interval, and have been widely used as membrane models mainly studied at temperatures higher than their main phase transition temperature. Less investigated are the unsaturated bilayers in the frozen state, for $T < T_m$. A combination of cw- and ED-spectra of 9 GHz electron spin resonance spectroscopy is resulted to be particularly successful to study the librational dynamics in the low-temperature phases of chain-labelled lipid bilayers [15]. Here we report results on the characteristics, i.e., the mean-square angular amplitude, $\langle \alpha^2 \rangle$, and the correlation time, τ_c , of segmental librational motion in unsaturated POPC and DOPC bilayers spin-labelled with 5- and 16-PCSL.

Two-pulse ($\pi/2 - \tau - \pi - \tau - echo$) echo-detected EPR spectra at 200 K for 5-PCSL and 16-PCSL in POPC, DOPC and DPPC bilayers as a function of the

interpulse delay time, τ , are reported in figure 5.2.

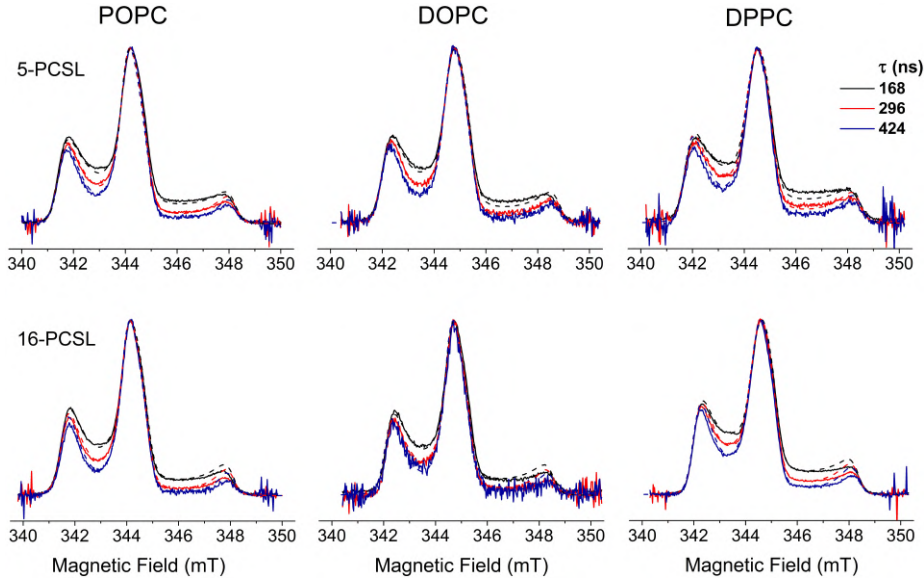


Figure 5.2: Two-pulse echo detected ED-EPR spectra of (*upper row*) 5-PCSL and (*lower row*) 16-PCSL in POPC (*left*), DOPC (*center*) and DPPC (*right*) bilayers at 200 K for interpulse spacings (top to bottom) of $\tau = 168, 296, 424$ ns. Solid lines are the corrected experimental spectra, dashed lines are simulations for isotropic librational motion.

In any sample, the dependence of the ED lineshape on echo delay, τ , reveals preferential spin relaxation in the intermediate spectral regions, at low and high field, that is characteristic of librational dynamics [16, 26, 28].

The occurrence of librational motion in the lipid membranes is also confirmed by spectral simulation. Indeed, by comparing the experimental and simulated spectra in figure 5.2 (solid and dashed lines, respectively), it can be seen that the ED spectra are well described with the *isotropic* model for librations, in which uncorrelated librations take place simultaneously and independently around the three X-, Y-, Z-nitroxide axes [16, 28].

From figure 5.2 it can be noted that spin-labels at the chain termini (see 16-PCSL spectra) relax faster than those at the beginning of the chains (see 5-PCSL spectra) and faster in the unsaturated POPC and DOPC than in saturated DPPC bilayers.

The partially-relaxed ED-spectra can be analyzed via the corresponding relaxation rate, W , evaluated for different pairs of time delay according to equation (2.27). An example is shown in figure 5.3.

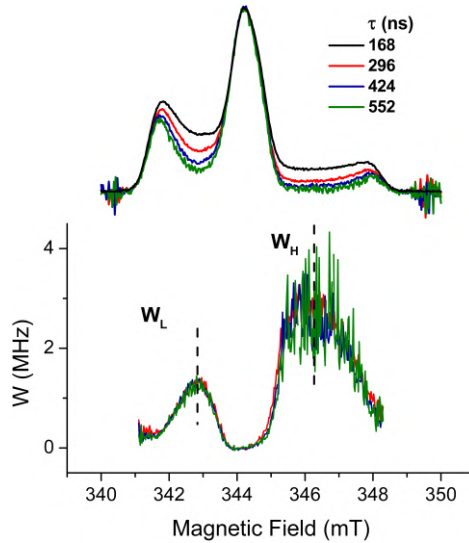


Figure 5.3: *Upper panel:* Two-pulse echo detected ED-EPR spectra of 5-PCSL in POPC bilayers at 200 K for interpulse spacings (top to bottom) of $\tau = 168, 296, 424, 552$ ns. *Lower panel:* Anisotropic part of the relaxation rate, W , obtained according to equation (2.27) from pairs of ED-spectra with interpulse separation of $\tau_1 = 168$ ns and $\tau_2 = 296$ ns, 424 ns or 552 ns.

As it can be seen, W -spectra coincide within the noise level. This shows that relaxation is close to exponential and confirms the validity of the isotropic model for librations. The relaxation rates are characterized by the maximum values, W_L and W_H , determined in the low- and high-field regions, respectively, of the ED-spectra (see figure 5.3). The difference in intensity at the two positions arises simply from the different inherent sensitivities of the low- and high-field spectral regions to spin relaxation.

The W_L -values collected from the ED-spectra of 5- and 16-PCSL in POPC, DOPC and DPPC bilayers at different temperatures are used to determine the motional parameter for librations, $\langle \alpha^2 \rangle \tau_c$, by using the conversion factors relating $\langle \alpha^2 \rangle \tau_c$ to W_L of $1.41 \times 10^{17} \text{ rad}^{-2} \text{ s}^{-2}$ for 5-PCSL and of $1.05 \times 10^{17} \text{ rad}^{-2} \text{ s}^{-2}$ for 16-PCSL, as established previously [16]. The temperature dependence of the motional parameter $\langle \alpha^2 \rangle \tau_c$ for 5- and 16-PCSL in POPC, DOPC and DPPC bilayers are compared in figure 5.4.

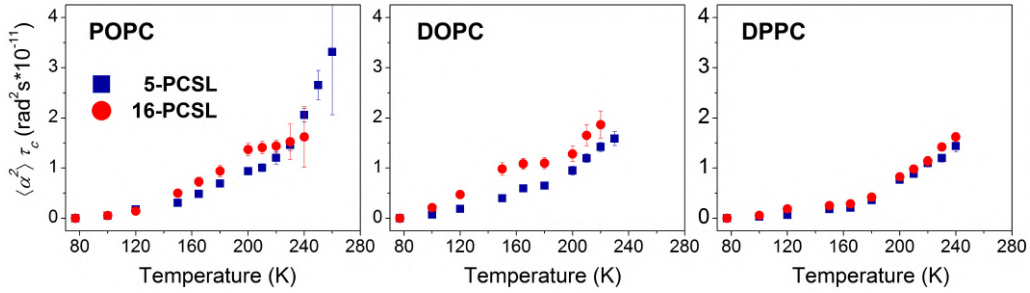


Figure 5.4: Temperature dependence of the amplitude-correlation time product of librations, $\langle \alpha^2 \rangle \tau_c$, for 5- (squares) and 16-PCSL (circles) in POPC (*left*) and DOPC (*center*) unsaturated bilayers and in DPPC (*right*) saturated bilayers.

In both unsaturated bilayers, $\langle \alpha^2 \rangle \tau_c$ for 5-PCSL increases first slowly up to 180 K and then more markedly for $T > 200$ K. The temperature dependence for 16-PCSL in monounsaturated POPC bilayers follows the steps described for 5-PCSL for $T < 200$ K and it becomes temperature independent for $T \geq 200$ K. At any temperature, the values of $\langle \alpha^2 \rangle \tau_c$ for 16-PCSL di-unsaturated DOPC bilayers are higher with respect to those recorded for 5-PCSL, with the motional parameter increasing from 77 to 150 K, being temperature independent up to 180 K and then increasing again for $T > 200$ K. Moreover, at each temperature and for both positional isomers, the values recorded for DOPC are always higher with respect to those recorded for POPC. Further, it is interesting to note that in DOPC echo disappears at lower temperatures for both 5- and 16-PCSL compared to POPC.

From these ED-EPR results it can be highlighted that in both unsaturated bilayers the librational dynamics is activated at lower temperature at variance from what occurs in saturated DPPC bilayers, where for both positional isomers $\langle \alpha^2 \rangle \tau_c$ maintains a low value over a broader temperature range [41]. The most likely explanation of these findings is that the unsaturated bilayers are characterized by a loosened packing density with respect to saturated bilayers that allows larger segmental librations. This is more evident in DOPC bilayers for the presence of unsaturated bonds in both the hydrocarbon chains.

To determine the angular amplitude of the librations, cw-EPR spectra of 5- and 16-PCSL in POPC and DOPC bilayers have been recorded as a function of temperature. Representative cw-EPR spectra are shown in figure 5.5.

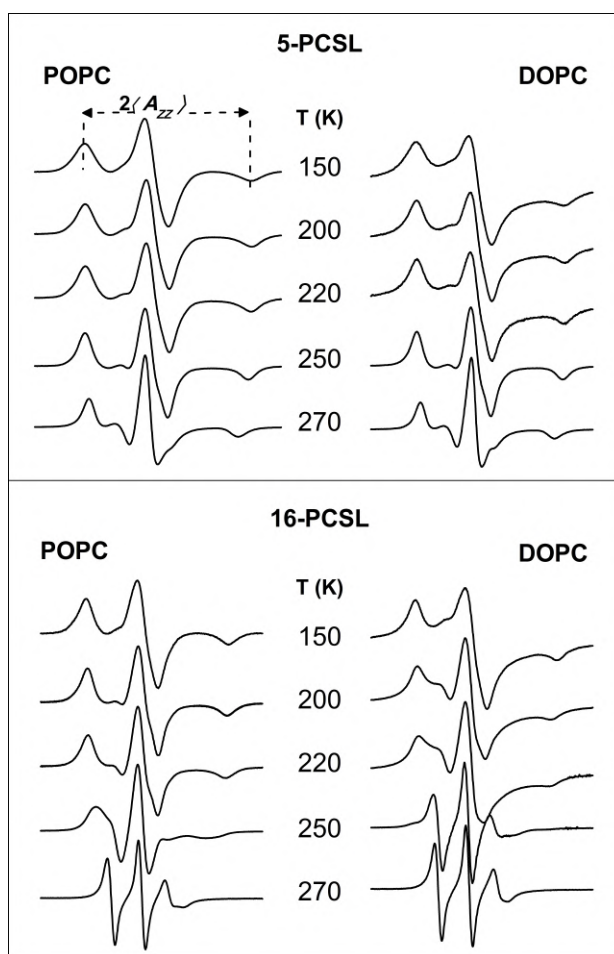


Figure 5.5: Cw-EPR spectra of (*upper panel*) 5- and (*lower panel*) 16-PCSL in monounsaturated bilayers of POPC and di-unsaturated bilayers of DOPC at selected temperatures. Central field = 330 mT, sweep width = 10 mT.

It can be seen that at the lowest temperatures (i.e., $T < T_m$ of the corresponding lipid matrix) the spectra for both labeling positions are powder patterns typical of immobilized nitroxides on the EPR time scale and the resonance lines are inhomogeneously broadened with evident spin-spin broadening in di-unsaturated DOPC. For both 5- and 16-PCSL, the spectral anisotropy reduces on increasing the temperature, first moderately and then more rapidly on approaching the temperature of the main phase transition of the bilayers. This behavior is particularly evident at the chain termini in the deep interior of the bilayers probed by 16-PCSL where, for $T > T_m$, three-line triplets with differential lineheights and linewidths are recorded.

From the collected cw-EPR spectra, the motionally averaged outermost peak separation $2\langle A_{ZZ} \rangle$ have been measured and then the mean-square angular amplitude of librations $\langle \alpha^2 \rangle$ calculated according to equation (2.16). The temperature

dependences of $2\langle A_{ZZ} \rangle$ and $\langle \alpha^2 \rangle$ are shown in figure 5.6.

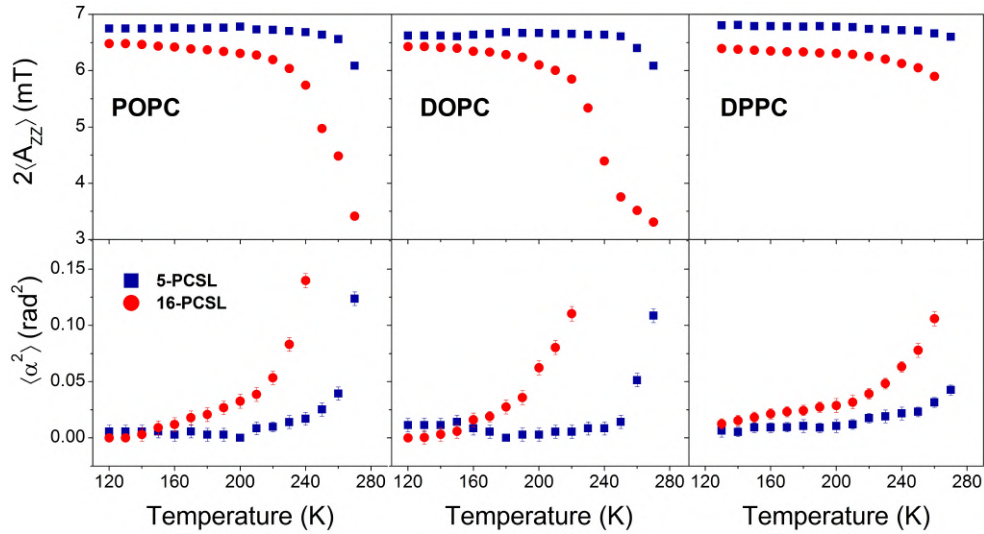


Figure 5.6: Temperature dependence of (*upper panel*) the hyperfine splitting, $2\langle A_{ZZ} \rangle$, and (*lower panel*) mean-square angular amplitude of libration, $\langle \alpha^2 \rangle$, for 5- (squares) and 16-PCSL (circles) in POPC (*left*), DOPC (*center*) and DPPC (*right*) bilayers. Errors for $2\langle A_{ZZ} \rangle$ are within symbols.

For POPC bilayers, $2\langle A_{ZZ} \rangle$ -values for 5-PCSL, i.e., a labeling probing the polar/apolar interface within the membranes, are high and almost constant at about 6.80 mT over a broad temperature range and reduce to 6.10 ± 0.02 mT at the highest temperature 270 K. For 16-PCSL, instead, $2\langle A_{ZZ} \rangle$ -values show a slow temperature decrease from 6.50 ± 0.02 mT to 6.20 ± 0.02 mT on going from 120 K to 220 K, and then a more marked and progressive decrease to 5.01 ± 0.02 mT at 250 K and 3.40 ± 0.02 mT at 270 K. For DOPC bilayers, the dependence on temperature for the two positional isomers is similar to that observed in POPC with an interesting difference: the reduction in $2\langle A_{ZZ} \rangle$ -values occurs at lower temperatures and it is more marked for 16-PCSL than for 5-PCSL. Indeed, from figure 5.6 it can be seen that for DOPC/5-PCSL a high and constant $2\langle A_{ZZ} \rangle$ value of about 6.30-6.50 mT is recorded up to 250 K, it is 6.40 ± 0.02 mT at 260 K and decreases to 6.09 ± 0.02 mT at 270 K; for DOPC/16-PCSL, instead, $2\langle A_{ZZ} \rangle$ is 4.40 ± 0.02 mT at 240 K, 3.70 ± 0.02 mT at 250 K and 3.30 ± 0.02 mT at 270 K, when the bilayers are in the fluid state.

What we have seen above for the temperature dependences of the outer hyperfine splitting is mirrored in the temperature dependences of the mean-square angular amplitude of librations for 5- and 16-PCSL in unsaturated POPC and DOPC bilayers reported in the lower panels of figure 5.6.

For 5-PCSL, $\langle \alpha^2 \rangle$ is first low and constant over a wide temperature range, then

it starts to increase rapidly for $T \geq 240$ K in POPC and for $T \geq 250$ K in DOPC. For 16-PCSL the angular amplitude is low and constant at the lowest temperatures, then it increases progressively, first slowly and then more rapidly for $T > 210$ K in POPC and $T > 190$ K in DOPC.

From the plots in figure 5.6, it can be also observed that the angular amplitudes of libration are higher at the chain termini than at the beginning of the chain and slightly higher in DOPC than in POPC. For monounsaturated POPC bilayers, α for 5-PCSL increases from $5.3^\circ \pm 1.8^\circ$ at 210 K to $7.4^\circ \pm 1.3^\circ$ at 240 K to $11.3^\circ \pm 0.8^\circ$ at 260 K, whereas for 16-PCSL it increases rapidly from $8.2^\circ \pm 1.2^\circ$ at 180 K to $10.3^\circ \pm 1.0^\circ$ at 200 K to $13.2^\circ \pm 0.6^\circ$ at 220 K. For di-unsaturated DOPC bilayers, comparable values to the above listed angles are recorded for 5-PCSL at the polar/apolar interface, while higher values are recorded for 16-PCSL in the inner hydrocarbon region, with α being $9.5^\circ \pm 1.1^\circ$ at 180 K, $14.2^\circ \pm 0.7^\circ$ at 200 K, $18.9^\circ \pm 0.5^\circ$ at 220 K.

Finally, for comparison, it is worthy to note from figure 5.6 that the $\langle \alpha^2 \rangle$ -values for both spin-labels are larger in the unsaturated bilayers than in the compact high- T_m bilayers of DPPC lipids [41]. They are, instead, comparable to those reported for stearic acid spin labels in bilayers of natural lipid extracted from Na,K-ATPase [32].

Characterization of the segmental librational motion is completed by evaluating the correlation time of motion, τ_c (figure 5.7). This is done by dividing the $\langle \alpha^2 \rangle \tau_c$ values by $\langle \alpha^2 \rangle$ at corresponding temperatures.

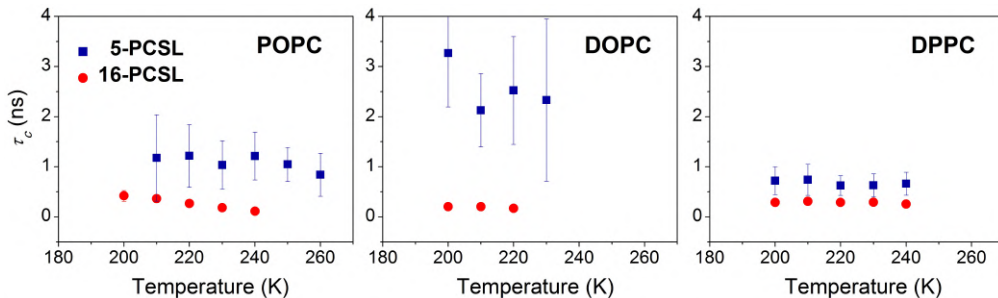


Figure 5.7: Temperature dependence of the librational correlation time, τ_c , for 5- (squares) and 16-PCSL (circles) in POPC (*left*) and DOPC (*center*) unsaturated bilayers and in DPPC (*right*) saturated bilayers.

From figure 5.7 it is evident that in both POPC and DOPC τ_c lies in the nanosecond time scale for 5-PCSL and in the subnanosecond time scale for 16-PCSL. Segmental chain librations lay in the subnanoseconds along the saturated chain of DPPC bilayers. In any sample, data in figure 5.7 give confirmation that librations are rapid and occur on the T_2 nanosecond timescale accessible to cw-EPR and two pulse electron spin echo experiments.

5.2 Angular librational oscillations in interdigitated lamellar phases

Some phosphocholine bilayer-forming lipids are able to self-assemble in a lamellar phase with interdigitated chains in the gel phase, either spontaneously or in the presence of an inducer agent at a threshold concentration that causes the loss of the bilayer midplane [84]. The induction of acyl chain interdigitation affects different bilayer properties, such as the packing density and order of the acyl chains, electrostatic interactions at the surface, structural and mechanical properties. EPR of chain-labelled lipids represent an appropriate tool to investigate lamellar phases with interdigitated chains. The main experimental evidence when lamellar phases with interdigitated chains are studied with EPR spectroscopy is that a positional isomer at the chain termini (viz., 14- or 16-PCSL) is located near the interfacial region on the opposite side of the lamellae, and it is motionally restricted to an extent comparable to that of a positional isomer at the first segments of the lipid chains (viz., 4- or 5-PCSL). So that, in the interdigitated phase two extreme positions of labeling (such as 5- and 16-PCSL) sample the same high-polarity interfacial bilayer regions upon the transfer of the apolar groups to water. Model membranes of the ether-linked lipid DHPC adopt an interdigitated structure in gel phase and have been characterized in-depth at low, cryogenic temperature by applying cw- and pulsed EPR [41, 136]. Here we focus on the librational oscillations of spin-labels in two fully hydrated lamellar assemblies with interdigitated chains, namely mixtures of DPPC and Lyso-PPC lipids at equimolar content and DPPC hydrated in ethanol and D₂O (60% v/v), that have been also studied by D₂O-ESEEM spectroscopy and presented in Section 4.2.

Cw-EPR spectra at selected temperatures for the two interdigitated systems in the frozen state are shown in figure 5.8.

They are powder patterns typical of spin-labeled lipids well incorporated within the host lipid matrix and probing a frozen ordered environment. Up to 220 K, both labeling positions (i.e., 5-PCSL, located at the polar/apolar interface, and 16-PCSL, located at the terminal methyl chain segment) are strongly immobilized and exhibit spectra of comparable large anisotropy and inhomogeneously broadened resonances. The spectral anisotropy reduces and the lines slightly narrow upon progressive temperature increase, and this is more evident at the $n = 16$ position than at the $n = 5$ position.

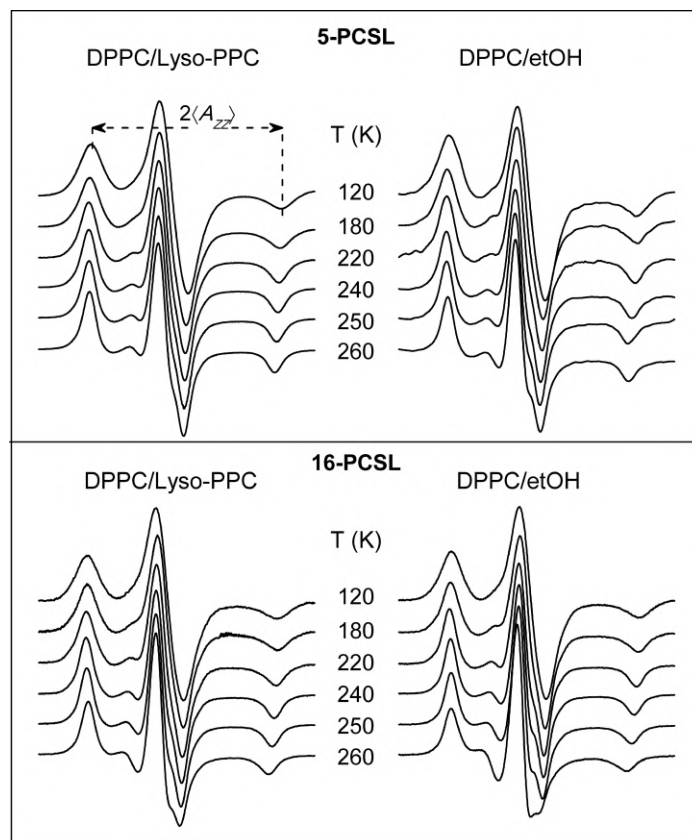


Figure 5.8: Cw-EPR spectra of (*upper panel*) 5- and (*lower panel*) 16-PCSL in interdigitated DPPC/Lyso-PPC (*left*) and DPPC/etOH (*right*) dispersions at selected temperatures. Central field = 332.5 mT, sweep width = 10 mT.

Variations in the spectral anisotropy in the differing samples can be single out in the temperature dependence of the outer hyperfine separation, $2\langle A_{ZZ} \rangle$, for both 5- and 16-PCSL (figure 5.9).

The interdigitated matrix composed by equimolar content of DPPC and Lyso-PPC is characterized by constant high values for the hyperfine separation of about 6.90 mT for both spin-labels. This value is maintained over a broad temperature range, up to 220 K, and then it progressively reduces to 6.72 ± 0.02 mT for 5-PCSL and more rapidly to 6.55 ± 0.02 mT for 16-PCSL. In the case of the interdigitated sample DPPC/etOH, again, for both labels, $2\langle A_{ZZ} \rangle$ maintains high values (that are smaller than those in DPPC/Lyso-PPC) up to 220 K, and it is slightly greater at $n = 5$ (6.85 ± 0.02 mT) than at $n = 16$ (6.80 ± 0.02 mT). For $T > 220$ K, the hyperfine separation reduces rapidly reaching 6.55 ± 0.02 mT for 5-PCSL and 6.38 ± 0.02 mT for 16-PCSL at 260 K.

The coincidence of the $2\langle A_{ZZ} \rangle$ values between the two extreme positions of labeling in both samples (DPPC/Lyso-PPC and DPPC/etOH) is a clear consequence

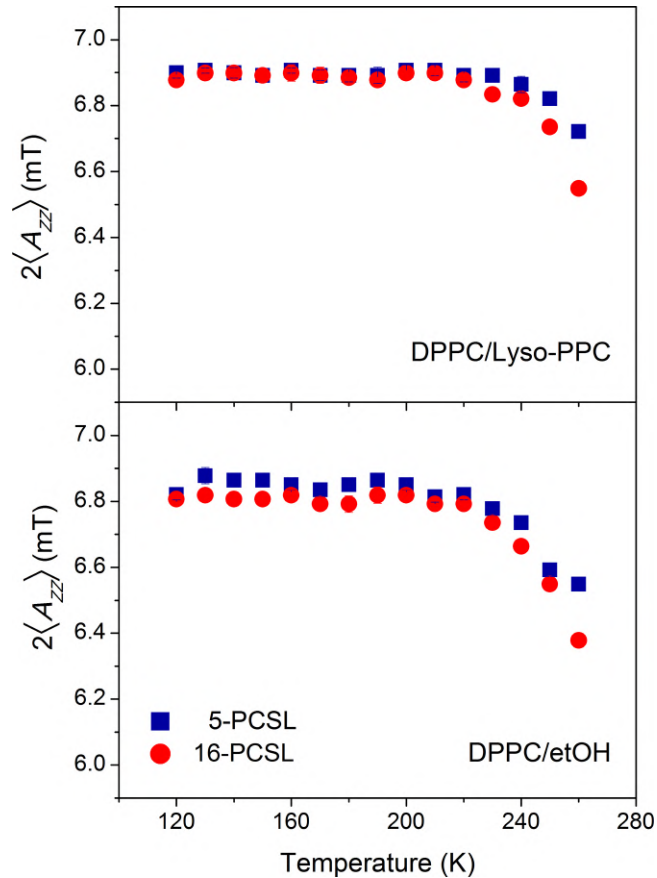


Figure 5.9: Temperature dependence of the hyperfine splitting, $2\langle A_{ZZ} \rangle$, for 5- (squares) and 16-PCSL (circles) in interdigitated (*upper panel*) DPPC/Lyso-PPC and (*lower panel*) DPPC/etOH dispersions. Errors are within symbols.

of chain interdigitation in which both spin-labels experience the same membrane environment and are exposed to the solvent at the polar/apolar interface. The temperature dependences of $2\langle A_{ZZ} \rangle$ for the spin-labeled lipids in both interdigitated samples differ notably from those reported for DPPC bilayers in figure 5.6 [41]. In noninterdigitated DPPC bilayers, $2\langle A_{ZZ} \rangle$ for 5-PCSL keeps high values over almost the entire sampled temperature range, whereas the values for 16-PCSL are lower and decrease on increasing the temperature. This finding accounts for the reduction in polarity (from the $2\langle A_{ZZ} \rangle$ -values at the lowest temperatures) and the increased segmental chain disorder and rotational mobility (from the $2\langle A_{ZZ} \rangle$ -values at the highest temperatures) on going down along the chain in DPPC bilayers [41, 132]. Data in figure 5.9 indicate that DPPC/etOH exhibits a more loose chain packing density with respect to DPPC/Lyso-PPC, evidenced by lower $2\langle A_{ZZ} \rangle$ -values in the high temperature regime. Differences in chain packing properties among various interdigitated samples were previously evidenced. Indeed, the interdigitated state

promoted in DPPC by glycerol is characterized by a uniformly tight packing of the interdigitated chains [132,144]. A loosened packing density was evidenced in DPPC with 80 mg/ml of ethanol [145] and chaotropic ions [146]. Other examples of loosened packed interdigitated bilayers are DHPC [41] and 1,3 DPPC [145], that are known to spontaneously interdigitate in the gel phase.

The slight temperature variation of the spectral anisotropy of the two end labels in the interdigitated matrices (see figure 5.8), the constant temperature dependence of the motionally averaged hyperfine separation in the low-temperature regime and its decrease at $T > 220$ K (see figure 5.9) are indication of librational motion [16,26,34,39,41]. Thus, by applying equation (2.16), the mean-square angular amplitudes of libration, $\langle \alpha^2 \rangle$, for 5- and 16-PCSL in DPPC/Lyso-PPC and DPPC/etOH have been evaluated and their temperature dependences are shown in figure 5.10.

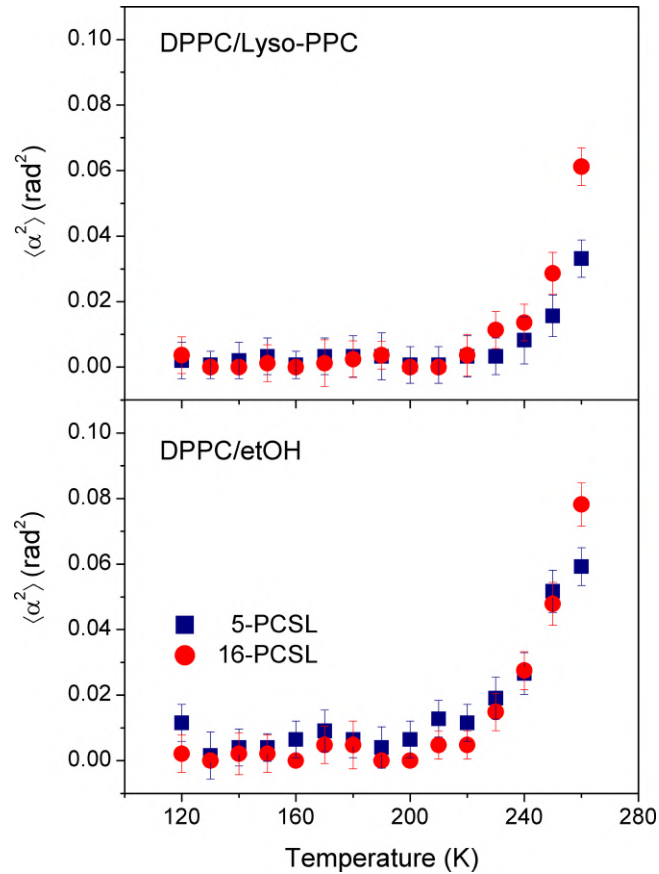


Figure 5.10: Temperature dependence of the mean-square angular amplitude of libration, $\langle \alpha^2 \rangle$, for 5- (squares) and 16-PCSL (circles) in interdigitated (*upper panel*) DPPC/Lyso-PPC and (*lower panel*) DPPC/etOH dispersions.

From the figure, it can be highlighted that *i*) in any sample, similar $\langle \alpha^2 \rangle$ are obtained for the two labeling positions as a result of chain interdigitation; *ii*) in both

samples, $\langle\alpha^2\rangle$ maintains a constant very small value up to 220 K and then it increases more rapidly in DPPC/etOH than in DPPC/Lyso-PPC matrix. The librational angle is $3.3^\circ \pm 2.3^\circ$, $5.2^\circ \pm 2.3^\circ$, $10.4^\circ \pm 0.9^\circ$ for 5-PCSL and $6.0^\circ \pm 1.5^\circ$, $6.7^\circ \pm 1.4^\circ$, $14.1^\circ \pm 0.7^\circ$ for 16-PCSL in DPPC/Lyso-PPC on going from 230 K to 240 K to 260 K, respectively; it is $7.9^\circ \pm 1.3^\circ$, $9.3^\circ \pm 1.1^\circ$, $13.9^\circ \pm 0.7^\circ$ for 5-PCSL and $7.0^\circ \pm 1.3^\circ$, $9.5^\circ \pm 1.0^\circ$, $15.9^\circ \pm 0.7^\circ$ for 16-PCSL in DPPC/etOH on going from 230 K to 240 K to 260 K, respectively. As a consequence of the difference in the chain packing density, the angular amplitude is greater in DPPC/etOH than in DPPC/Lyso-PPC. We note that $\langle\alpha^2\rangle$ temperature dependence in the two interdigitated systems is similar to what has been reported for DPPC with equimolar content of cholesterol [16], for lipids extracted from Na,K-ATPase membranes [32], for small spin-labels in glassy media [26, 147], and for spin-labeled proteins [39, 148].

It is of interest to compare the results obtained in the interdigitated DPPC/Lyso-PPC and DPPC/etOH samples with those for the ether-linked DHPC membranes, which spontaneously interdigitate in the gel state, and with those for the ester-linked saturated DPPC [41] and unsaturated POPC and DOPC [143], which form bilayers with noninterdigitated chains. In the interdigitated DHPC sample, the $\langle\alpha^2\rangle$ -values for both labels are very low and temperature independent up to 230 K and then increase steeply, with $\langle\alpha^2\rangle$ always greater at the chain termini than at the first segments, over the entire temperature range investigated [41]. In the noninterdigitated bilayers, instead, the two positional isomers show a progressive increase in the librational amplitudes on increasing the temperature with $\langle\alpha^2\rangle$ at the last methyl chain segments (16-PCSL) greater than $\langle\alpha^2\rangle$ at the polar/apolar interface (5-PCSL) at any temperature higher than 180 K [41, 143].

5.3 Dynamical transition

The most striking feature of the temperature dependences of the mean-square librational amplitudes reported in figures 5.6 and 5.10 is that they show a steep increase at about 200 K. This behavior has already been observed with EPR methods in a variety of hydrated spin-labeled biosystems, including proteins [35, 39, 142, 148–150], model membranes [40, 41] and natural membranes [31, 32]. Even more interestingly, the same trend is observed in the temperature dependence of the mean-square atomic displacement, $\langle r^2 \rangle$, by neutron scattering and Mössbauer spectroscopy for hydrated macromolecules and membranes [29, 45, 46, 49–52]. The temperature at which the rapid increase of the mean-square displacement parameter or of the mean-square librational amplitude sets in is identified with the dynamical transition temperature, T_d , which denotes the onset of stochastic (diffusive) motions of greater amplitude [29].

According to this definition, a dynamical transition can be identified in POPC and DOPC spin-labeled with 16-PCSL at a temperature of 210 K and 190 K, respectively, and at about 220 K in the interdigitated DPPC/Lyso-PPC and DPPC/etOH membranes spin-labeled with both 5-PCSL and 16-PCSL. These temperature values are comparable with those previously reported in the range 180 - 240 K, by spin-label EPR in ether and ester-linked saturated chain PC membranes [41], by neutron scattering in hydrated purple membranes [43, 47] and in multibilayers of dimyristoylphosphatidylcholine [52] and dipalmitoylphosphatidylcholine [48], and in model membranes by Raman spectroscopy [38, 151, 152] and differential scanning calorimetry [153, 154]. A dynamical transition has been also observed in a nonbiological system composed by hydrated microgels [55, 94].

For temperatures above the dynamical transition temperature, the temperature dependences of the mean-square angular amplitude of librations conform with an Arrhenius law:

$$\langle \alpha^2 \rangle = \langle \alpha^2 \rangle_o \exp(-E_a/RT) \quad (5.1)$$

where E_a is the activation energy of motion that can be derived from linear fits of the data of $\langle \alpha^2 \rangle$ vs $1/T$ as shown in figure 5.11.

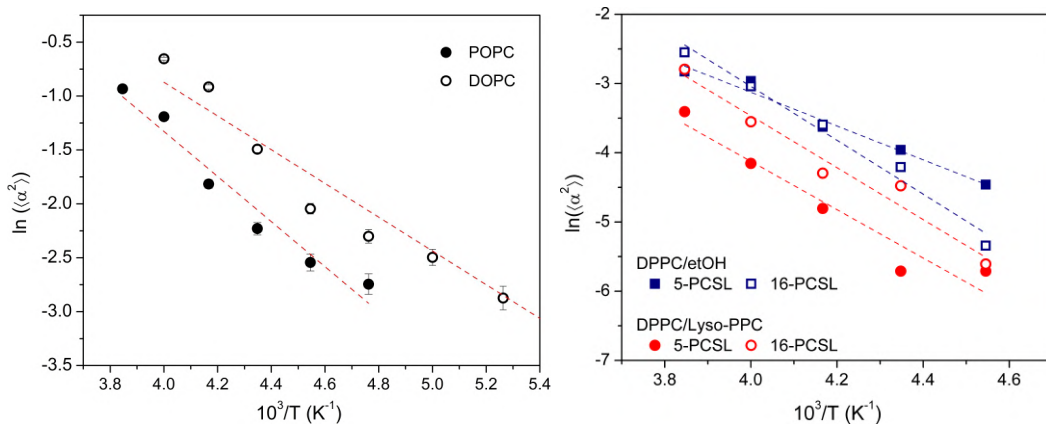


Figure 5.11: Arrhenius plots characterizing the temperature dependence of the librational amplitude, $\langle \alpha^2 \rangle$, in the high temperature regime for (*left*) 16-PCSL in POPC (solid symbols) and in DOPC (open symbols), (*right*) DPPC/etOH (squares) and DPPC/Lyso-PPC (circles) interdigitated samples spin labeled with 5- (solid symbols) and 16-PCSL (open symbols). Dashed lines are linear regressions evaluated by applying equation (5.1) to the data.

The activation energy, E_a , evaluated from the linear regression of figure 5.11 is 17.4 ± 1.8 kJ/mol for POPC and 13.0 ± 1.4 kJ/mol for DOPC, spin-labeled in the inner hydrocarbon region; it is 20.3 ± 1.8 kJ/mol for 5-PCSL and 32.4 ± 2.6 kJ/mol

for 16-PCSL in DPPC/etOH, and 29.0 ± 4.6 kJ/mol for 5-PCSL and 31.2 ± 3.4 kJ/mol for 16-PCSL in DPPC/Lyso-PPC.

These values are, again, comparable with previous estimations for spin-labeled lipid model systems [41, 53, 155] and natural membranes and proteins [39] analyzed with electron spin resonance, as well as for proteins analyzed with other experimental techniques [29, 54] and non-biological samples [94], suggesting that the dynamical transition is a property shared by various hydrated systems investigated with a multiplicity of physical techniques.

Role of hydration water in the dynamical properties of proteins and lipid membranes

The dynamics of biomolecular systems is influenced by the hydration water and both underlie on functioning. In this chapter the effects of hydration on the librational dynamics of bio-aggregates in the low temperature regime 120 - 270 K are investigated. Globular proteins of different structure, namely β -Lactoglobulin (β -LG) and Human Serum Albumin (HSA), and lamellar phases of di-saturated symmetrical chain palmitoyl-phosphatidylcholines (DPPC) are considered. The librational motion is markedly restricted in the lyophilized proteins and is activated in hydrated proteins independently of the hydration level. The segmental librational oscillations in lipid membranes are dependent on chain position of labeling and hydration conditions: they are larger in the deep bilayer interior than in the region close to the polar/apolar interface and larger in hydrated than in de-hydrated lipid membranes. In any hydrated biosystems, proteins or lipid lamellae, the dynamical transition is detected around 220 - 235 K, as it is found for other investigated samples, and is characterized by similar activation energies in the range 16 - 21 kJ mol⁻¹.

6.1 Effect of hydration on librational oscillations of α vs β globular proteins

β -LG and HSA are two globular proteins with different shape and size (18 kDa for β -LG vs 66 kDa for HSA) and structure (mainly α -helical for HSA and β -sheets for β -LG) that serves as paradigms for biophysical studies (see figure 6.1 for proteins structure). For the present work, they have been spin-labeled with maleimide nitroxide derivative (5-MSL) on surface exposed cysteins (Cys121 in β -LG and Cys34 in HSA) and prepared in differing hydration conditions, namely lyophilized, low hydration ($h = 0.10 - 0.14$) and full hydration ($h > 0.55$).

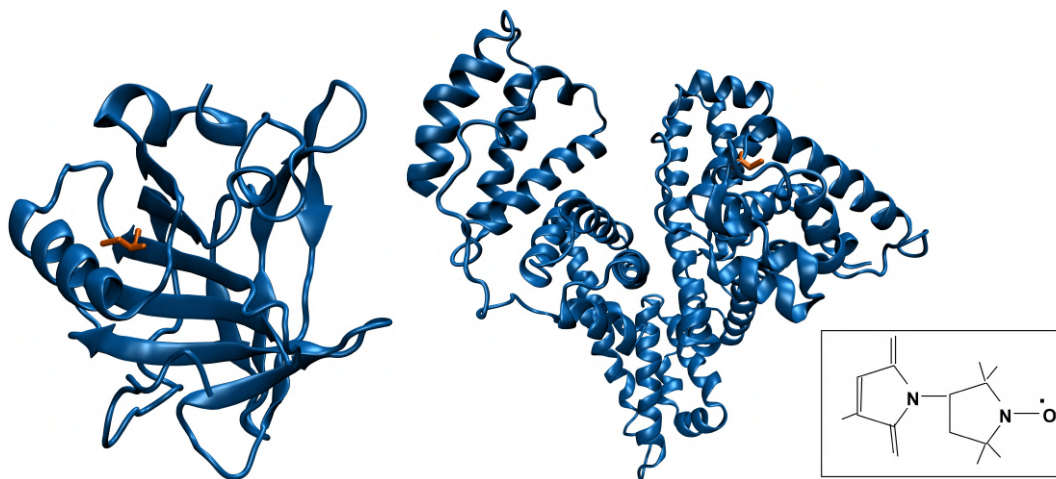


Figure 6.1: Crystal structure of (*left*) β -LG (PDB ID 3NPO [156]) and (*center*) HSA (PDB ID 1AO6 [157]). Cysteins labelled with maleimide spin-label 5-MSL are indicated in orange. 5-MSL structure is also given (*right*).

In figure 6.2 are reported the conventional EPR spectra at selected temperatures of frozen spin-labeled β -LG and HSA in the lyophilized state and at low and full hydration.

From figure 6.2 it can be seen that, independently from protein structure, *a*) powder patterns with large spectral widths and broad lines are obtained at low temperatures; *b*) the spectral anisotropy moderately reduces and the linewidths narrow only at the highest temperatures for proteins in the lyophilized state; *c*) for hydrated proteins, from $T > 200$ K, the spectra progressively narrow and achieve almost sharp lineshapes at the highest temperatures, more in the full than in the low hydration state.

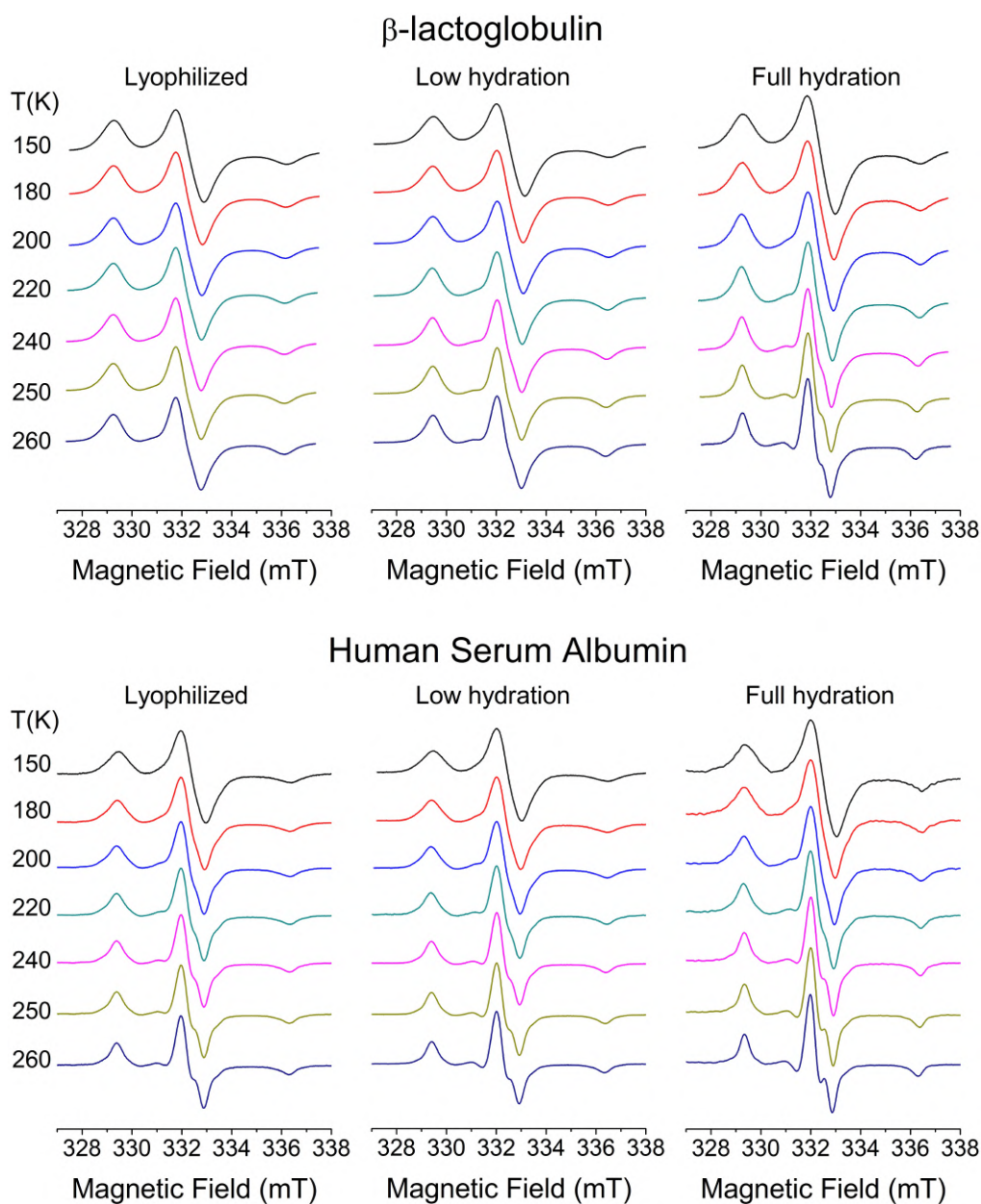


Figure 6.2: Cw-EPR spectra at selected temperatures of (*upper panel*) β -Lactoglobulin/5-MSL and (*lower panel*) Human Serum Albumin/5-MSL at differing hydration conditions.

The two proteins display a rather similar temperature dependence of the motionally averaged hyperfine splitting, $2\langle A_{ZZ} \rangle$, under corresponding experimental conditions. Indeed, as it can be seen by comparing the two panels in figure 6.3, an almost constant value of the hyperfine separation of about 6.90 mT is recorded in both lyophilized proteins, although it slightly decreases in β -LG on increasing the temperature. In contrast, the $2\langle A_{ZZ} \rangle$ temperature dependence in the proteins at

low and full hydration is biphasic: for $T < 200$ K, the $2\langle A_{ZZ} \rangle$ -values increase with temperature, more rapidly in HSA than in β -LG; for $T \geq 200$ K a similar decrease at the same rate is recorded for the $2\langle A_{ZZ} \rangle$ -values as a result of progressive motional narrowing by librations [101].

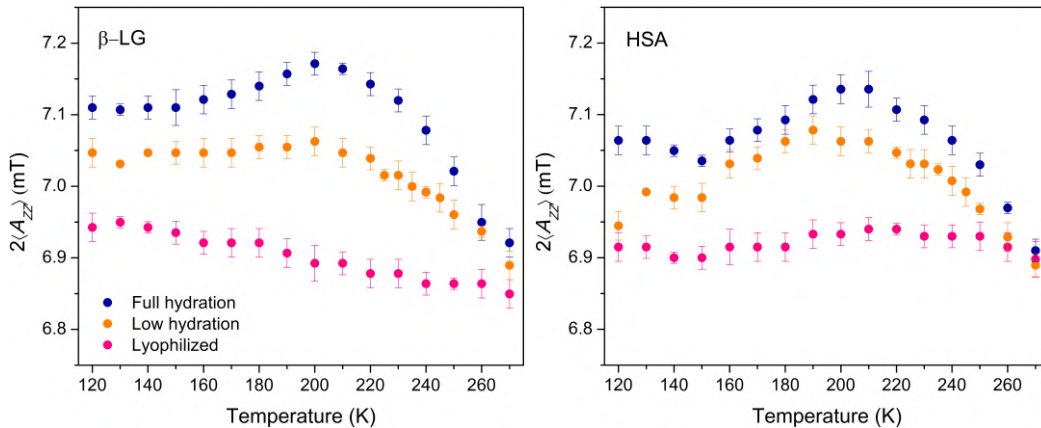


Figure 6.3: Temperature dependence of the outer hyperfine separation, $2\langle A_{ZZ} \rangle$, for (left) β -LG/5-MSL and (right) HSA/5-MSL at differing hydration conditions.

On the whole, the results in figure 6.3 suggest that *i*) the environmental polarity on the surface of the proteins and the ability of the nitroxide maleimide group to form hydrogen-bonds with water molecules change as a function of sample hydration in the order: lyophilized $<$ low hydration $<$ full hydration; *ii*) mobility is markedly restricted in the lyophilized proteins and it intensifies at comparable extent for both proteins in the high temperature regime at low and full hydration conditions. Our results in the first point are in agreement with literature data that evidenced the presence of a *local maximum* in the temperature dependence of $2\langle A_{ZZ} \rangle$ in HSA dispersed in different amount of hydration water molecules [142, 158] and in fully hydrated spin-labelled lipid membranes [16]. To this behavior contributes the temperature dependence of the hydrogen-bonded water [159]. The second point clearly indicate that low-temperature protein dynamics is activated even in the presence of a low number of water molecules. Again, this is in keeping with previous results obtained by using a variety of biophysical techniques relating the level of hydration to the dynamics of proteins [35, 59, 150, 160, 161] and non-biological polymers [94, 162].

The dependence on temperature of the mean-square angular amplitude of librations, $\langle \alpha^2 \rangle$, in figure 6.4 gives results consistent with those of the outer hyperfine splitting, $2\langle A_{ZZ} \rangle$, in figure 6.3.

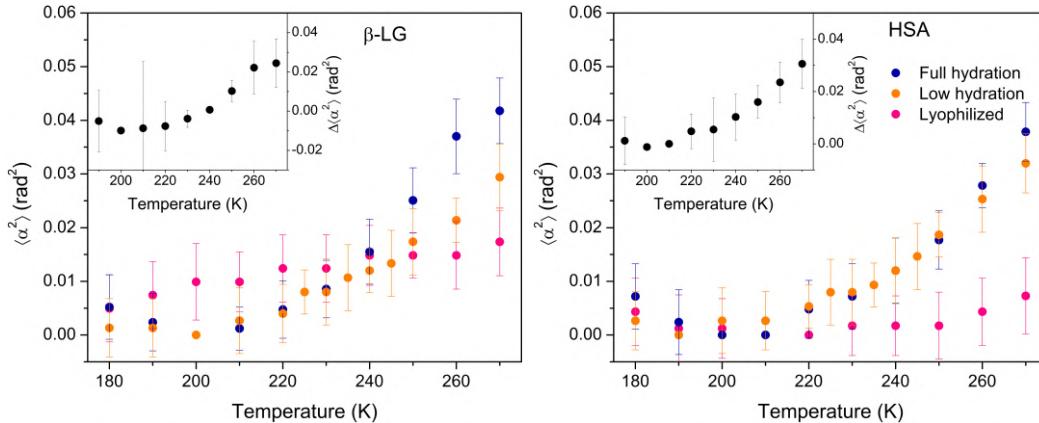


Figure 6.4: Temperature dependences of the mean-square angular amplitude, $\langle\alpha^2\rangle$, for (left) β -LG/5-MSL and (right) HSA/5-MSL at differing hydration conditions. *Insets:* difference among the $\langle\alpha^2\rangle$ values in the hydrated and in the lyophilized samples, $\Delta\langle\alpha^2\rangle = \langle\alpha^2\rangle$ (fully hydrated) $- \langle\alpha^2\rangle$ (lyophilized).

Indeed, in figure 6.4 it can be seen that for $T > 200$ K, the angular librational amplitude increases at the same rate and at the same extent in both proteins under low and full hydration conditions, whereas in the lyophilized samples $\langle\alpha^2\rangle$ maintains small and constant values in accordance with previous findings [29, 35, 92]. In this latter case, the angular amplitude is about $6 - 7^\circ$ in β -LG and about 3° in HSA.

To better discriminate the effect of the solvent on the extent of the librational amplitudes, we plot the difference in the mean-square angular amplitude, $\Delta\langle\alpha^2\rangle$, between the fully hydrated and lyophilized samples. From the insets in figure 6.4 it can be seen that the presence of water molecules intensifies the librational dynamics at a temperature where the protein dynamical transition sets in, with T_d at about 230 K in both proteins. In close agreement with literature [39, 54], at this temperature β -LG and HSA cross low-energy barriers of 21.53 ± 0.53 kJ mol⁻¹ and 21.04 ± 2.10 kJ mol⁻¹, respectively. These activation energies are calculated by applying equation (5.1) to the $\langle\alpha^2\rangle$ -values.

6.2 Effect of hydration on segmental librational oscillations of lipid bilayers

Cw-EPR spectra at selected temperatures in the range 150 - 260 K for 4-PCSL and 14-PCSL in DPPC bilayers at different level of hydration, namely de-hydrated, low hydrated ($n_w/n_L \simeq 3$), and fully hydrated ($n_w/n_L \geq 25$) are shown in figure 6.5 and 6.6, respectively. With 4-PCSL the hydrocarbon region in close proximity at the polar/polar interface of the lipid glycerol backbone is probed, whereas with

14-PCSL the inner hydrocarbon region at the bilayer midplane is investigated.

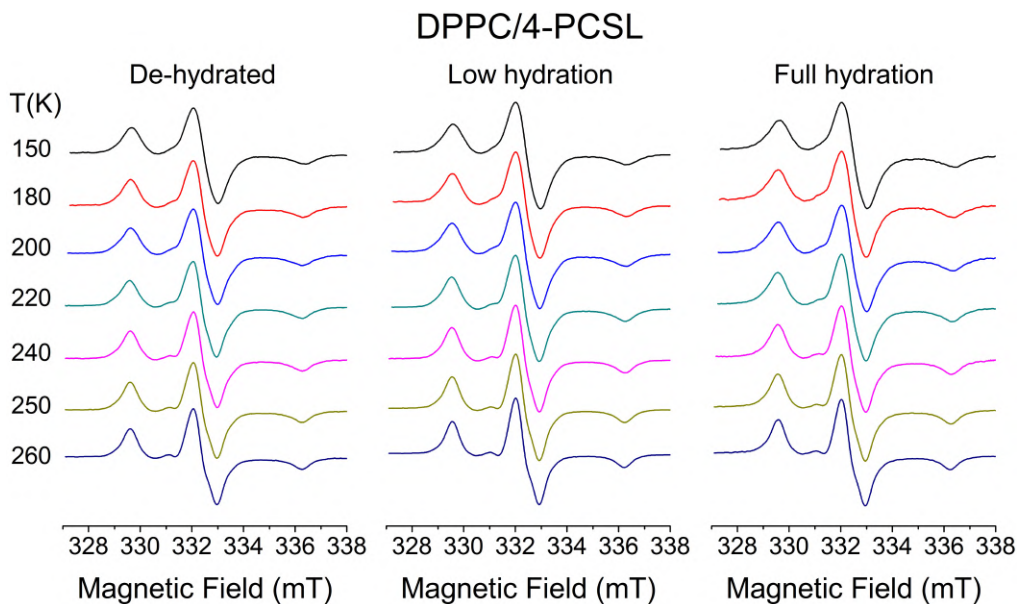


Figure 6.5: Cw-EPR spectra at selected temperatures of 4-PCSL in DPPC bilayers at differing hydration conditions.

For DPPC bilayers in the dehydrated state, the spectra of 4-PCSL are powder patterns of immobilized spin-labels well incorporated in the host matrix and characterized by large anisotropy and linewidths which reduce only a little at the highest temperatures. In contrast, by comparing the spectra of de-hydrated 4-PCSL in DPPC with that of the other two samples at corresponding temperatures, it is evident a slight reduction of the spectral anisotropy of comparable extent at low and full hydration state, particularly in the high temperature regime.

Powder patterns of immobilized spin-labels are also recorded for 14-PCSL in DPPC bilayers in the frozen state at any hydration condition (see figure 6.6). However, a progressive reduction of anisotropy on increasing temperature is evident independently of the hydration condition. In the low and fully hydrated DPPC/14-PCSL samples, in particular, variations proceed at a more rapid rate for $T > 240$ K compared to the de-hydrated sample. In any case, the region of the CH_2 segments at the beginning of the chains is a membrane zone where the lipid mobility is strongly inhibited; in contrast, lipid mobility is favored in the inner membrane region of the terminal CH_3 methyls [16, 132].

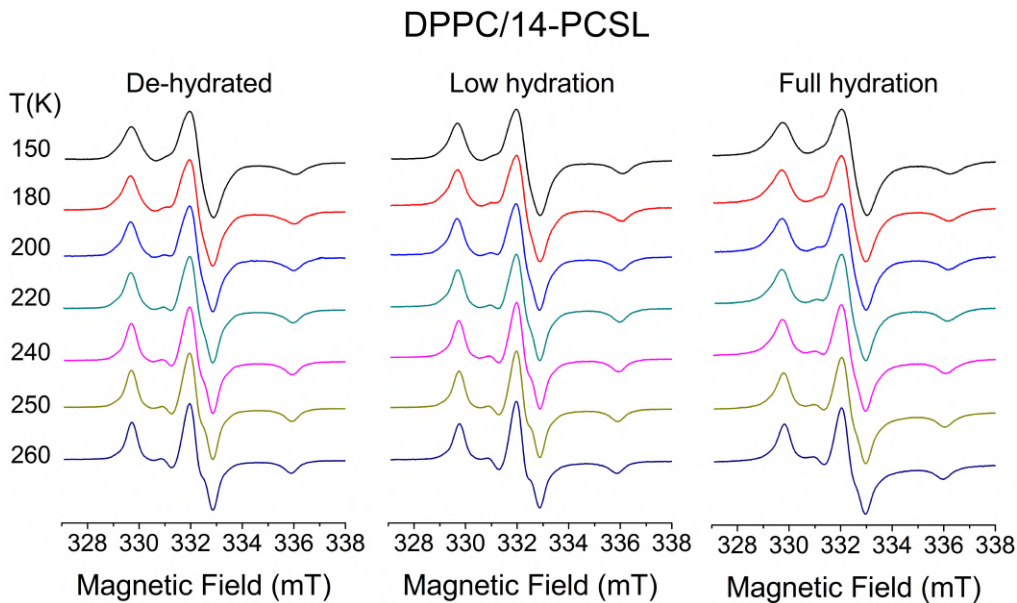


Figure 6.6: Cw-EPR spectra at selected temperatures of 14-PCSL in DPPC bilayers at differing hydration conditions.

Quantitatively, the effects of hydration on the spectral anisotropy of chain labelled lipids in DPPC bilayers can be seen in the temperature dependences of the motionally averaged hyperfine separation, $2\langle A_{ZZ} \rangle$, reported in figure 6.7.

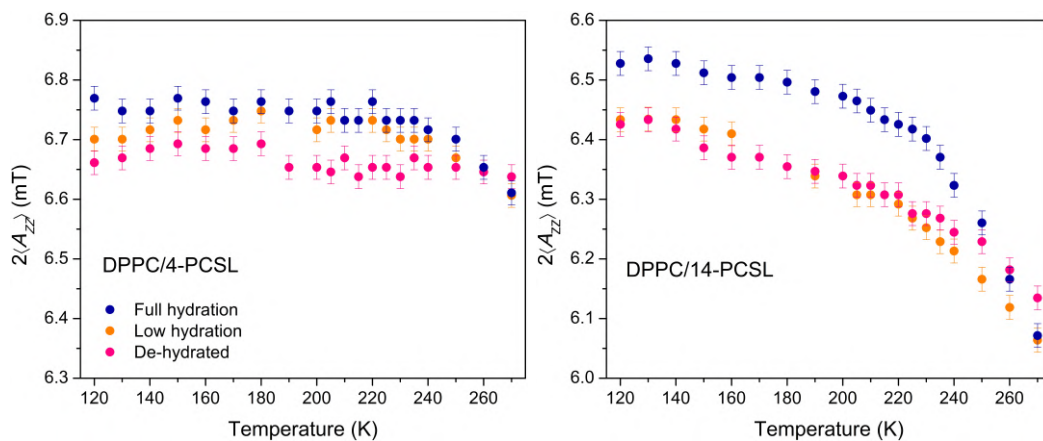


Figure 6.7: Temperature dependence of the outer hyperfine separation, $2\langle A_{ZZ} \rangle$, (*left*) 4-PCSL and (*right*) 14-PCSL in DPPC bilayers at differing hydration conditions.

Higher values of $2\langle A_{ZZ} \rangle$ are reported for 4-PCSL with respect to 14-PCSL over the whole temperature range investigated. This behavior in the low temperature regime reflects the higher environmental polarity at the polar/apolar interface of the bilayers compared to the low one at the bilayer midplane. From figure 6.7 it

comes out that the temperature variation of $2\langle A_{ZZ} \rangle$ is dependent on labeling position and hydration conditions. For 4-PCSL in DPPC, $2\langle A_{ZZ} \rangle$ in the de-hydrated sample maintains a constant value of 6.65 ± 0.02 mT over the entire temperature range investigated and it is also evident that $2\langle A_{ZZ} \rangle$ (de-hydrated) $\leq 2\langle A_{ZZ} \rangle$ (low hydrated) $\leq 2\langle A_{ZZ} \rangle$ (fully hydrated), with a moderate hyperfine separation reduction in the high temperature regime for the hydrated samples.

For 14-PCSL, $2\langle A_{ZZ} \rangle$ (de-hydrated) $\simeq 2\langle A_{ZZ} \rangle$ (low hydrated) $< 2\langle A_{ZZ} \rangle$ (fully hydrated). This trend at the lowest temperatures accounts for the higher environmental polarity in DPPC bilayers at full hydration. For $T > 200$ K, a progressive decrease of $2\langle A_{ZZ} \rangle$ is seen in any DPPC/14-PCSL sample, being more rapid in the hydrated (both low and full) than in the de-hydrated sample. At 200 K, $2\langle A_{ZZ} \rangle$ is 6.35 ± 0.02 mT both in the de-hydrated and low hydrated samples and 6.50 ± 0.02 mT in the fully hydrated one; at 270 K it reduces to 6.15 ± 0.02 mT in the de-hydrated sample and to 6.05 ± 0.02 mT in the low hydrated and fully hydrated samples.

The results in figure 6.7 clearly suggest that the segmental chain dynamics is favored in the hydrated samples and that in the upper bilayer regions is markedly restricted in the de-hydrated state, whereas mobility is observed at the chain termini even in the absence of water. Indeed, it can be noted that for DPPC/14-PCSL at the bilayer midplane the hyperfine separation decreases first slowly from 120 K to 240 K and then more rapidly from this temperature onward.

What is said for the temperature dependences of $2\langle A_{ZZ} \rangle$ is mirrored in the temperature dependences of the angular librational amplitude for both positional isomers in the various DPPC samples reported in figure 6.8.

For de-hydrated DPPC bilayers in the frozen state the librational dynamics at the first acyl segments is highly restricted, maintaining an average angular value of about 5° , whereas librational oscillations of increasing angular amplitude are recorded at the terminal chain segments. Indeed, for 14-PCSL α progressively increases from about 3° to about 13° on going from 120 K to 270 K. For low hydrated and fully hydrated DPPC samples, the angular librational amplitudes intensify with temperature more in the inner hydrocarbon region than at the polar/apolar interface, with α reaching a value of about 10° and 17° for 4-PCSL and 14-PCSL, respectively, at full hydration condition at 270 K.

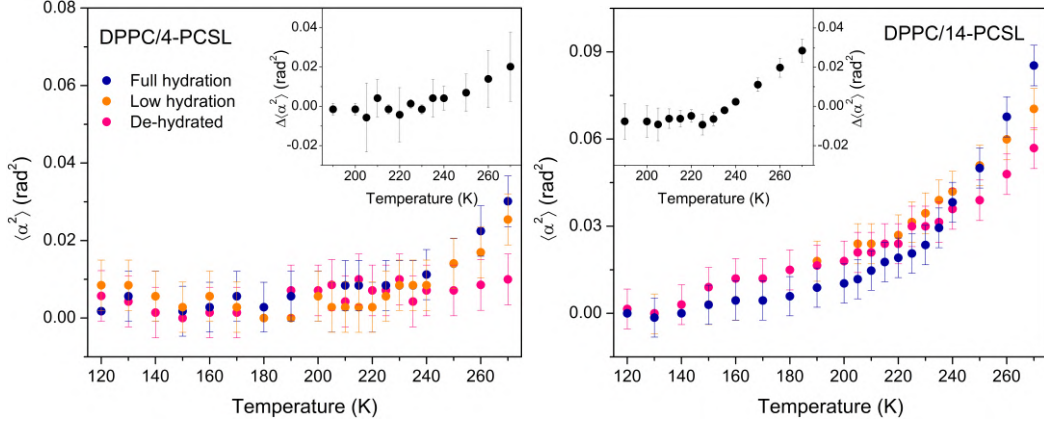


Figure 6.8: Temperature dependence for the mean-square librational amplitude $\langle \alpha^2 \rangle$ for (left) 4-PCSL and (right) 14-PCSL in DPPC bilayers at differing hydration conditions. *Insets:* difference among the $\langle \alpha^2 \rangle$ values in the hydrated and in the de-hydrated samples, $\Delta \langle \alpha^2 \rangle = \langle \alpha^2 \rangle$ (fully hydrated) $- \langle \alpha^2 \rangle$ (de-hydrated).

The insets in figure 6.8, showing the difference between the mean-square angular amplitudes of libration in the hydrated and de-hydrated samples for 4-PCSL and 14-PCSL in DPPC bilayers, clearly indicate that the presence of hydration water intensifies significantly the librational dynamics at a temperature of about 240 K for 4-PCSL and 225 K for 14-PCSL. Therefore, the dynamical transition at $T_d = 240$ K can be attributed for hydrated 4-PCSL sample with an activation energy $E_a = 18.43 \pm 1.93$ kJ mol⁻¹, deduced from the Arrhenius plot (equation (5.1)) for the librational amplitudes. The Arrhenius plots on DPPC spin-labeled with 14-PCSL for the three hydration conditions are shown in figure 6.9.

It can be seen from figure 6.9 that the fully hydrated sample presents a steeper temperature dependence with respect to the low hydrated and the de-hydrated samples. Indeed, the activation energies are: E_a (de-hydrated) = 7.47 ± 0.67 kJ mol⁻¹ < E_a (low hydration) = 9.06 ± 0.11 kJ mol⁻¹ < E_a (full hydration) = 16.39 ± 0.57 kJ mol⁻¹. The spin-label EPR results for hydrated DPPC agree with previous data obtained with 5- and 16-PCSL exhibiting the dynamical transition around 220 K and $E_a = 15.0 \pm 1.5$ and 13.0 ± 0.3 kJ mol⁻¹ at the upper bilayer region and inner hydrocarbon zone, respectively [41]. A gradient of increasing librational amplitudes has been observed on going down the chain at low temperatures in DPPC with equimolar content of cholesterol [16]. These results are also consistent with those recorded in frozen fully hydrated unsaturated bilayers [143]. Moreover, slowed dynamics in the region close to the head groups as a consequence of reduced hydration has been observed in POPC bilayers by applying computational methods [163]. Further, a recent neutron diffraction study highlighted that the dynamics of DMPC

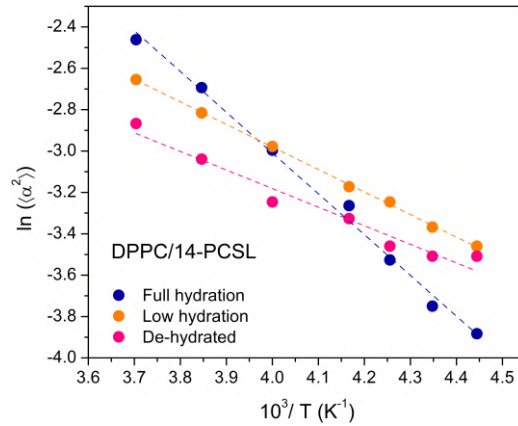


Figure 6.9: Arrhenius plots characterizing the temperature dependence of the librational amplitude, $\langle \alpha^2 \rangle$, in the high temperature regime for 14-PCSL in DPPC bilayers at differing hydration conditions. Dashed lines are linear regressions evaluated by applying equation (5.1) to the data.

bilayers is not significantly affected by the hydration state and the dynamical transition occurs at a lower temperature in the hydrocarbon chains compared to the polar heads [52].

The present EPR results give insights on how water promotes dynamics in proteins and model membranes. Acting as a plasticizer, water could equally affect the functioning in the active state of the macromolecules.

Hydration water dynamics in tau protein from neutron scattering data analysis

The work I am going to present in this chapter is the result of a research period at the Institut de Biologie Structurale (IBS) in Grenoble, where I spent six months in 2019 as a visiting PhD student. I was welcomed in the DYNAMOP group led by Dr. Martin Weik and my research supervised by Dr. Giorgio Schirò. My research is part of a major project aiming to develop a comprehensive model to describe hydration water dynamics from room temperature down to the supercooled regime, analyzing neutron scattering data on the intrinsically disordered human tau protein at different energy resolutions. Here, quasi-elastic neutron scattering data analysis on tau protein collected at the time-of-flight spectrometer TOFTOF will be presented. It drafts of an ongoing work dealing with the development of a code to perform the fitting procedure of TOFTOF data on hydration water in perdeuterated tau.

7.1 Quasi elastic neutron scattering: theoretical background

Neutrons existence, predicted by Rutherford in 1920, was confirmed by Chadwick in 1932 when the irradiation of beryllium with α -particles caused an emission attributed to neutral particles coming from beryllium itself [164]. In 1936 the first Bragg reflection of slow neutrons from MgO single crystal and Fe was performed. Later, in 1946, experiments in a nuclear reactor by Fermi and Zinn demonstrated that neutrons can be reflected if the angle of incidence of the neutron beam is sufficiently small, starting subsequent progresses in the application of neutrons in

science [165]. In late '60s and '70s the majority of all the currently used nuclear facilities were built.

The validity of neutron research relies on the fact that thermal neutrons wavelength corresponds to interatomic distances in solids and liquids, thus the crystalline structure can be investigated as well as shape and volume of macromolecules. Because of its neutral condition, neutron does not disrupt matter and it is able to come close to the nuclei, being a useful tool for the investigation of a variety of samples with only weak interactions [166]. Moreover, the energy of thermal neutrons is of the order of the energies of excitation in condensed matter, giving information on interatomic forces, and neutrons have magnetic moment, thus can interact with unpaired electron giving information on the electron spins and electronic configuration [167].

7.1.1 Principles of neutron scattering

A neutron is scattered by a general scattering system with a probability dependent on the cross section, σ , which is the quantity measured in a scattering experiment (figure 7.1). The cross section is determined by the element, the isotope and the relative spin orientations of neutrons and nuclei. The cross section can be defined as the ratio between the number of neutrons scattered per second and the flux of a neutron beam, Φ .

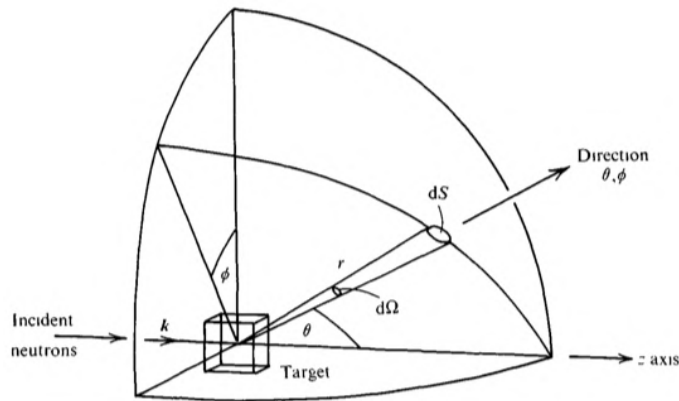


Figure 7.1: Geometry for a scattering experiment (from [167]).

To take into account the angles (θ, ϕ) of the scattering process, the differential cross section can be defined as follows:

$$\frac{d\sigma}{d\Omega} = \frac{N}{\Phi d\Omega} \quad (7.1)$$

with N number of neutrons scattered per second in the solid angle $d\Omega$. Considering the possibility of energy exchange between the scattered neutrons and the nuclei of

the scattering system, the partial differential cross section is defined:

$$\frac{d^2\sigma}{d\Omega dE'} = \frac{N}{\Phi d\Omega dE'} \quad (7.2)$$

with N number of neutrons scattered per second in the solid angle $d\Omega$ with final energy $[E'; E' + dE']$.

In the simple case of an incident beam of neutrons interacting with a single fixed nucleus, the following wavefunctions can be associated:

$$\psi_{incident} = \exp(ikz) \quad (7.3)$$

$$\psi_{scattering} = -\frac{b}{r} \exp(ikr) \quad (7.4)$$

where b is a constant, the so-called scattering length. Its value, depending on the nucleus and the spin-state of the nucleus-neutron system, needs to be determined experimentally [167].

It is useful to apply the Fermi's golden rule to derive a definition of the differential cross section describing the process of a scattering system in an initial state λ defined by the wavevector k which, interacting with a potential V , goes in a final state λ' described by the wavevector k' as follows:

$$\frac{d\sigma}{d\Omega_{\lambda \rightarrow \lambda'}} = \frac{k'}{k} \left(\frac{m}{2\pi\hbar^2} \right)^2 |\langle k'\lambda' | V | k\lambda \rangle|^2 \quad (7.5)$$

where $V(\mathbf{r}) = 2\pi\hbar^2 m^{-1} b \delta(\mathbf{r})$ is the short range Fermi pseudopotential, m is the mass of the neutron and r is the neutron coordinate [167].

The conservation of the energy among the initial and final state of the scattering system, respectively E_λ and $E_{\lambda'}$, and of the scattering neutrons, E and E' , allows the following expression for the partial differential cross section:

$$\left(\frac{d^2\sigma}{d\Omega dE'} \right)_{\lambda \rightarrow \lambda'} = \frac{k'}{k} \left(\frac{m}{2\pi\hbar^2} \right)^2 |\langle k'\lambda' | V | k\lambda \rangle|^2 \delta(E + E_\lambda - E' - E_{\lambda'}) \quad (7.6)$$

with $\delta(E_{initial} - E_{final})$ the energy distribution described by a Dirac function. Inserting the expression for the Fermi pseudopotential, equation (7.6) becomes:

$$\left(\frac{d^2\sigma}{d\Omega dE'} \right)_{\lambda \rightarrow \lambda'} = \frac{k'}{k} \sum_j b_j |\langle \lambda' | \exp(i\mathbf{q} \cdot \mathbf{r}_j) | \lambda \rangle|^2 \delta(E + E_\lambda - E' - E_{\lambda'}) \quad (7.7)$$

being $\mathbf{q} = k - k'$ the scattering vector. Thus, writing the Dirac function in its

integral form it follows:

$$\begin{aligned} \left(\frac{d^2\sigma}{d\Omega dE'} \right)_{\lambda \rightarrow \lambda'} &= \frac{k'}{k} \frac{1}{2\pi\hbar} \sum_{ij} b_j b_i \int_{-\infty}^{+\infty} \langle \lambda | \exp(-i\mathbf{q} \cdot \mathbf{r}_j(0)) | \lambda' \rangle \times \\ &\quad \langle \lambda' | \exp(iHt/\hbar) \exp(i\mathbf{q} \cdot \mathbf{r}_i(0)) \exp(-iHt/\hbar) | \lambda \rangle \exp(-i\omega t) dt \end{aligned} \quad (7.8)$$

and applying the Heisenberg operator:

$$\begin{aligned} \left(\frac{d^2\sigma}{d\Omega dE'} \right)_{\lambda \rightarrow \lambda'} &= \frac{k'}{k} \frac{1}{2\pi\hbar} \sum_{ij} b_j b_i \int_{-\infty}^{+\infty} \langle \lambda | \exp(-i\mathbf{q} \cdot \mathbf{r}_j(0)) | \lambda' \rangle \times \\ &\quad \langle \lambda' | \exp(i\mathbf{q} \cdot \mathbf{r}_i(t)) | \lambda \rangle \exp(-i\omega t) dt \end{aligned} \quad (7.9)$$

with $\mathbf{r}_i(t)$ the position of the nuclei at time t . Summing over λ' and by applying the density operator and averaging over λ , equation (7.9) can be written as [167]:

$$\frac{d^2\sigma}{d\Omega dE'} = \frac{k'}{k} \frac{1}{2\pi\hbar} \sum_{ij} b_j b_i \int_{-\infty}^{+\infty} \langle \exp(-i\mathbf{q} \cdot \mathbf{r}_j(0)) \exp(i\mathbf{q} \cdot \mathbf{r}_i(t)) \rangle \times \exp(-i\omega t) dt \quad (7.10)$$

The scattering length b_i for the i th atom shall be such that:

$$\begin{aligned} \overline{b_i b_j} &= \overline{b^2} & \text{if } i = j \\ \overline{b_i b_j} &= \overline{b^2} & \text{if } i \neq j \end{aligned} \quad (7.11)$$

and thus equation (7.10) can be easily written as follows:

$$\begin{aligned} \frac{d^2\sigma}{d\Omega dE'} &= \frac{k'}{k} \frac{1}{2\pi\hbar} \overline{b^2} \sum_{ij} \int_{-\infty}^{+\infty} \langle \exp(-i\mathbf{q} \cdot \mathbf{r}_j(0)) \exp(i\mathbf{q} \cdot \mathbf{r}_i(t)) \rangle \times \exp(-i\omega t) dt + \\ &\quad + \frac{k'}{k} \frac{1}{2\pi\hbar} (\overline{b^2} - \overline{b^2}) \sum_i \int_{-\infty}^{+\infty} \langle \exp(-i\mathbf{q} \cdot \mathbf{r}_i(0)) \exp(i\mathbf{q} \cdot \mathbf{r}_i(t)) \rangle \times \exp(-i\omega t) dt \end{aligned} \quad (7.12)$$

with the first term of the sum in equation (7.12) being the coherent part and the second term the incoherent part of the total scattering cross section. The cross section is proportional to the scattering length b and the difference in the scattering lengths arises from the different total spin states of the nucleus-neutron system.

Moreover, defining the coherent scattering cross section as $\sigma_{coh} = 4\pi\bar{b}^2$ and the incoherent scattering cross section as $\sigma_{inc} = 4\pi(\bar{b}^2 - \bar{b}^2)$, equation (7.12) is also:

$$\frac{d^2\sigma}{d\Omega dE'} = \frac{\sigma_{coh}}{4\pi} \frac{k'}{k} S_{coh}(\mathbf{q}, \omega) + \frac{\sigma_{inc}}{4\pi} \frac{k'}{k} S_{inc}(\mathbf{q}, \omega) \quad (7.13)$$

where $S_{inc}(\mathbf{q}, \omega)$ and $S_{coh}(\mathbf{q}, \omega)$ are the incoherent and coherent dynamic structure factors, respectively. The first one accounts for the correlation among positions of different nuclei and the second one represents the correlation among positions of a single nucleus at different times [167].

7.1.2 Scattering functions

The dynamic structure factors can be written with the useful intermediate function for the nuclei $I(\mathbf{q}, t)$ as follows:

$$\begin{aligned} S_{coh}(\mathbf{q}, \omega) &= \frac{1}{2\pi} \int_{-\infty}^{+\infty} I_{coh}(\mathbf{q}, t) \exp(-i\omega t) dt \\ S_{inc}(\mathbf{q}, \omega) &= \frac{1}{2\pi} \int_{-\infty}^{+\infty} I_{inc}(\mathbf{q}, t) \exp(-i\omega t) dt \end{aligned} \quad (7.14)$$

with the intermediate functions:

$$\begin{aligned} I_{coh}(\mathbf{q}, t) &= \frac{1}{N} \sum_{ij} \langle \exp(-i\mathbf{q} \cdot \mathbf{r}_j(0)) \exp(i\mathbf{q} \cdot \mathbf{r}_i(t)) \rangle \\ I_{inc}(\mathbf{q}, t) &= \frac{1}{N} \sum_i \langle \exp(-i\mathbf{q} \cdot \mathbf{r}_i(0)) \exp(i\mathbf{q} \cdot \mathbf{r}_i(t)) \rangle \end{aligned} \quad (7.15)$$

where N is the total number of nuclei in the scattering system. The above derivation and the following ones can be found in detail in [167–170].

It is possible to return to the real space taking the Fourier transform of the intermediate scattering function, $G(\mathbf{r}, t)$, which is the time-dependent pair-correlation function:

$$G(\mathbf{r}, t) = \frac{1}{(2\pi)^3} \int_{-\infty}^{+\infty} I(\mathbf{q}, t) \exp(-i\mathbf{q} \cdot \mathbf{r}) d\mathbf{q} \quad (7.16)$$

and therefore:

$$G(\mathbf{r}, t) = \frac{1}{N} \sum_{ij} \int_{-\infty}^{+\infty} \langle \delta(\mathbf{r} - \mathbf{r}' + \mathbf{r}_i(0)) \delta(\mathbf{r}' - \mathbf{r}_j(t)) \rangle d\mathbf{r}' \quad (7.17)$$

If $i = j$, $G(\mathbf{r}, t)$ is known as the self pair-correlation function.

From equation (7.16), it follows:

$$S(\mathbf{q}, \omega) = \frac{1}{N} \frac{1}{2\pi\hbar} \int_{-\infty}^{+\infty} \int_{-\infty}^{+\infty} G(\mathbf{r}, t) \exp(i\mathbf{q} \cdot \mathbf{r}) d\mathbf{r} \exp(-i\omega t) dt \quad (7.18)$$

that can be easily divided in a coherent contribution and an incoherent one to the dynamic structure factor, as it has been done in equation (7.14).

It can be demonstrated that by applying the density operator to the scattering functions and in particular to the dynamic structure factor it results:

$$S(\mathbf{q}, \omega) = \exp\left(\frac{\hbar\omega}{k_B T}\right) S(-\mathbf{q}, -\omega) \quad (7.19)$$

with k_B the Boltzmann constant and T the temperature. This equation is known as the *principle of detailed balance* and reports the relationship between the two opposite processes of energy loss and energy gain by the neutron, following the Boltzmann population distribution among the two energy levels involved in the processes [167, 168].

7.1.3 The incoherent contribution

The scattering length b involved in the calculation of the total scattering cross section differs depending on the chemical element because different are the spin states involved. Hydrogen has an average scattering length, \bar{b} , averaged over its two spin states, which the coherent scattering cross section is proportional to, that is small; on the contrary, \bar{b}^2 is large and the resulting incoherent scattering cross section proportional to $(\bar{b}^2 - \bar{b}^2)$ is large. An opposite example is the case of deuterium, for this element \bar{b}^2 and \bar{b}^2 are similar quantities, thus the incoherent cross section for deuterium is small. Biosystems contain larger amount of hydrogen atoms with respect to the other constituent of biomolecules. Therefore, neutron scattering signal from biological matter is dominated by the incoherent contributions.

Focusing on the incoherent contribution to the intermediate scattering function, it is possible to distinguish a time-dependent contribution and a time-independent one:

$$I_{inc}(\mathbf{q}, t) = I_{inc}(\mathbf{q}, \infty) + I_{inc}^{inel}(\mathbf{q}, t) \quad (7.20)$$

with $I_{inc}^{inel}(\mathbf{q}, t)$ being the inelastic term of the intermediate incoherent scattering function. This term takes into account three separate motions: translational, rotational and vibrational motion [168]:

$$I_{inc}^{inel}(\mathbf{q}, t) = I_{inc}^{tra}(\mathbf{q}, t) \cdot I_{inc}^{rot}(\mathbf{q}, t) \cdot I_{inc}^{vib}(\mathbf{q}, t) \quad (7.21)$$

The incoherent dynamic structure factor consequently becomes:

$$S_{inc}(\mathbf{q}, \omega) = I_{inc}(\mathbf{q}, \infty)\delta(\omega) + S_{inc}^{inel}(\mathbf{q}, \omega) \quad (7.22)$$

with $I_{inc}(\mathbf{q}, \infty)\delta(\omega)$ being an elastic contribution. From equation (7.21):

$$S_{inc}^{inel}(\mathbf{q}, \omega) = S_{inc}^{tra}(\mathbf{q}, \omega) \otimes S_{inc}^{rot}(\mathbf{q}, \omega) \otimes S_{inc}^{vib}(\mathbf{q}, \omega) \quad (7.23)$$

The inelastic term of $S_{inc}(\mathbf{q}, \omega)$ contains small energies contributions addressed in the so-called *quasi-elastic* term, $S_{inc}^{qel}(\mathbf{q}, \omega)$. This term describes the contribution of the translational and the rotational motion, $S_{inc}^{tra}(\mathbf{q}, \omega)$ and $S_{inc}^{rot}(\mathbf{q}, \omega)$ respectively, while the vibrational contribution to motion, $S_{inc}^{vib}(\mathbf{q}, \omega)$, manifests as an inelastic spectra outside the quasi-elastic region; because of the faster scale of motions of vibrations and librations of molecules, this term can generally be considered as an inelastic background in the quasi-elastic energy region [168, 170]. Applying the convolution of equation (7.23) and the consideration on the vibrational motion in the quasi-elastic energy range, the incoherent dynamic structure factor in the quasi-elastic energy range can be written as follows:

$$S_{inc}^{inel}(\mathbf{q}, \omega) = \exp[-\langle u^2 \rangle q^2] [S_{inc}^{tra}(\mathbf{q}, \omega) \otimes S_{inc}^{rot}(\mathbf{q}, \omega) + S_{inc}^I(\mathbf{q}, \omega)] \quad (7.24)$$

with the exponential term, the Debye-Waller factor, considering the attenuation to the intensity of the scattering signal due to vibrations and rapid internal molecular motions, and $S_{inc}^I(\mathbf{q}, \omega)$ being an inelastic background considering the vibrational contribution in the quasi-elastic region [168]. $S_{inc}^{inel}(\mathbf{q}, \omega)$ can also be written as:

$$S_{inc}^{inel}(\mathbf{q}, \omega) = \exp[-\langle u^2 \rangle q^2] \left[I_{inc}^{dif}(\mathbf{q}, \infty) \cdot \delta(\omega) + S_{inc}^{dif}(\mathbf{q}, \omega) + S_{inc}^I(\mathbf{q}, \omega) \right] \quad (7.25)$$

where $I_{inc}^{dif}(\mathbf{q}, \infty)$ is the elastic incoherent structure factor and represent the quasi-elastic intensity contained in the purely elastic peak, and $S_{inc}^{dif}(\mathbf{q}, \omega)$ is the quasi-elastic contribution [170].

7.1.4 Characterization of hydration water dynamics

Quasi-elastic incoherent neutron scattering is appropriate to characterize the diffusive motion of liquids, being suitable for the study of water dynamics in hydrated systems [61,168]. It has been commonly applied a model for the description of water dynamics considering a decoupling between the translational and the rotational motion of water molecules [171]. Albeit a simplification, this approach has proved effective in some cases for fitting the experimental data, giving information on the time scales and properties of the two range of motions.

It has been demonstrated that for most proteins the biological functionality is lost in the absence of water, while the first layer of hydration water is sufficient to activate proteins motion and to create a biologically active complex. [61,172]. Because of the large scattering cross section of hydrogen atoms, using deuterium is an efficient procedure to selectively investigate part of the systems. Various neutron scattering experiments have been performed on biomolecules hydrated in D₂O such as proteins [61,92,173,174], protein aggregates [93,175], biological and lipid membranes [52,176–179], but also nonbiological microgels [55]. Following the same path, using perdeuteration allows to focus on water dynamics. This technique consists in the substitution of hydrogen atoms in the sample with deuterium atoms. The majority of the scattering signal arises now from water hydrogen atoms. The procedure has been used to analyze specific regions of lipid membranes [52,180], to investigate the role of hydration water and membranes [91,177] and the possible coupling between hydration water and protein dynamics [47,61,93,160,181].

7.1.5 The Time-of-Flight spectrometer: TOFTOF at FRM-II

A quasi-elastic neutron scattering (QENS) experiment aims to detect the status of neutrons after their interaction with the scattering system. Knowing the initial condition of the neutron beam, i.e., initial energy and wavevector state, and the scattering angle with respect to the incident beam allows the determination of the final energies of the scattered neutrons and the momentum transfer [168]. Among the various approaches, a time-of-flight measurement is suitable to collect a wide range of momentum and energy transfer of the scattered cold neutrons, measuring their kinetic energies after interacting with the scattering system.

TOFTOF at the neutron source Heinz Maier-Leibnitz (FRM-II) in Garching (Germany) is an example of a time-of-flight spectrometer. It is a multi-chopper time-of-flight spectrometer with direct geometry, which can be used in many applications, thanks to the high rotation speed of the chopper system (up to 22 000 rpm) and the high neutron flux in the wavelength range of 1.4 -14 Å, which can

be adjusted to obtain energy resolutions between 3 meV and 2 μeV [182, 183]. It is particularly suitable to investigate dynamics in disordered materials in hard and soft condensed matter systems (such as polymer melts, glasses, molecular liquids, or liquid metal alloys), properties of new hydrogen storage materials to low-energy magnetic excitations in multiferroic compounds, and molecular magnets. It can be successfully applied to perform energy-resolved quasi-elastic neutron scattering experiments on proteins, vesicles, and biological materials [183]. A schematic overview of the TOFTOF instrument is depicted in figure 7.2.

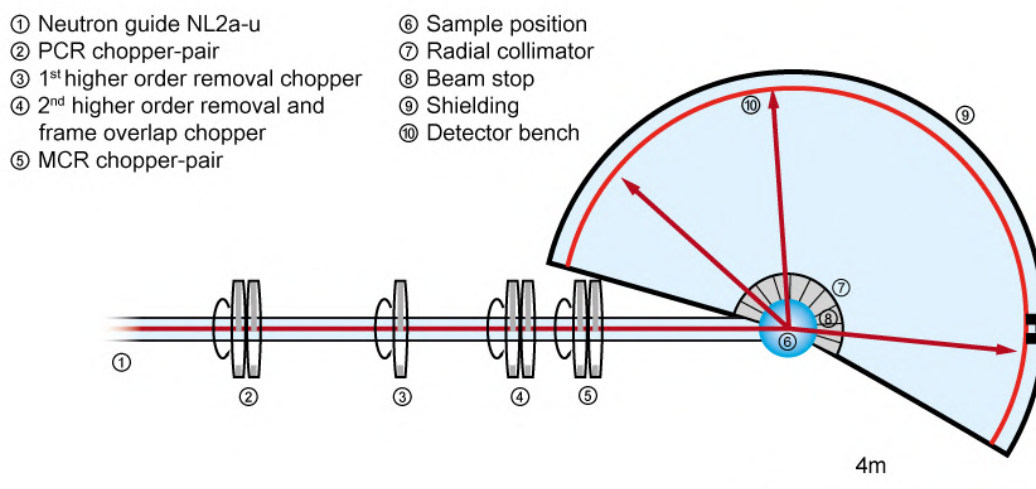


Figure 7.2: Scheme of the TOFTOF instrument configuration at the Heinz Maier-Leibnitz Zentrum from [183].

7.2 A model for water dynamics in perdeuterated tau protein

Human tau is an intrinsically disordered protein which exists in six possible isoforms in brain tissue, it is highly soluble and responsible of the stability of microtubules in the axons in the neuronal cells, where the isoform htau40 is the largest one. Beside this main activity, tau protein is also involved in cellular signaling, neuronal development, neuroprotection and apoptosis. Excessive tau phosphorylation induces the formation of insoluble aggregates responsible of the occurrence of neurodegenerative pathologies, such as Alzheimer's disease [184]. Compared to folded proteins, tau, specifically its isoform htau40, has been shown to have a stronger coupling with its hydration water [92], it proved also enhancement of its hydration water motions in the fiber aggregation configuration, suggesting the possible role played by water in the formation of fibers [93]. Moreover, the relation between

htau40 dynamical transition and the onset of its hydration water translational diffusion has been also addressed by means of QENS data collected at the backscattering spectrometer SPHERES [61].

In this scenario the study here presented collocates. The presented results are fitting procedures on htau40, simply addressed as tau in the following, realized by coding ex-novo Python scripts to analyze data collected at TOFTOF on perdeuterated tau protein hydrated in water, DTAU-H₂O. Data were collected at the resolution temperature of 10 K and in the temperature range from 210 K to 300 K (210 K, 230 K, 240 K, 250 K, 260 K, 280 K, 300 K) for a momentum transfer interval from 0.1 Å⁻¹ to 1.8 Å⁻¹ at 0.1 Å⁻¹ step, an energy transfer from -1 meV to +3 meV and an energy resolution of 30 μeV. The $\mathbf{q} = 0.1, 1.7$ and 1.8 Å⁻¹ set of data were excluded because no valid values were collected. For the other datasets, values with no errors associated were excluded.

The first step in the analysis of these QENS data has been the spectra normalization for the integrated area of the resolution spectra recorded at 10 K, where there is almost a purely elastic contribution to the signal. A heuristic fit \mathbf{q} by \mathbf{q} was performed to determine the contribution to the elastic peak of the resolution spectra, in this way a function fitting the spectra at 10 K has been identified. Then, this resolution function has been used in the heuristic fit \mathbf{q} by \mathbf{q} at each of the other temperatures to take into account the instrument resolution and contribution to the signal. By this fitting procedure, the minimum number of contributions necessary to efficiently reproduce the experimental data is hypothesized. We found the convolution of two Lorentzian-like contributions to be enough to represent our data. The crucial point is now the choice of a complete model to describe water motion behavior. We decided to consider a roto-translational model in which rotations around the center of mass (the oxygen atom) and translations of the center of mass of water molecules are convoluted. A term taking into account the fraction of molecules that appear immobile on TOFTOF time scale is also added, which mainly has an elastic contribution. A constant term for the instrumental background and vibrations occurring too fast for TOFTOF time scale is also considered.

The two-dimensional model in the space (\mathbf{q}, ω) applied to describe our TOFTOF DTAU-H₂O data follows from equations (7.24) and (7.25) and the incoherent dynamic structure factor can be written as [171, 185]:

$$S(\mathbf{q}, \omega) \propto [[S^{elast}(\mathbf{q}, \omega) + (S^{tra}(\mathbf{q}, \omega) \otimes S^{rot}(\mathbf{q}, \omega))]] \otimes R(\mathbf{q}, \omega) + b(\mathbf{q}) \quad (7.26)$$

with $S^{elast}(\mathbf{q}, \omega)$ a purely elastic contribution, $R(\mathbf{q}, \omega)$ is the resolution function to

be convoluted, and $b(\mathbf{q})$ is the background. Resolving the convolution between the translational and the rotational contributions:

$$S(\mathbf{q}, \omega) \propto \left(S^{elast}(\mathbf{q}, \omega) + \frac{j_0^2(\mathbf{q}a)}{\pi} \frac{\Gamma_T}{\omega^2 + \Gamma_T^2} + \frac{1}{\pi} \sum_{l=1}^{\infty} (2l+1) j_l^2(\mathbf{q}a) \frac{l(l+1)D_r + \Gamma_T}{\omega^2 + (l(l+1)D_r + \Gamma_T)^2} \right) \otimes R(\mathbf{q}, \omega) + b(\mathbf{q}) \quad (7.27)$$

where the translational and rotational motions are considered in the translational parameter, Γ_T , that is expected to be \mathbf{q} -dependent, and in the rotational parameter, D_r , which is, instead, expected to be \mathbf{q} -independent; $j_l(\mathbf{q}a)$ is the spherical Bessel function of l -order; a is the H-O distance that is the radius of rotation. Considering that the first two terms of the expansion account for about 90%, the model can be approximated as follows:

$$S(\mathbf{q}, \omega) \propto \left[\left(A_0 \cdot \delta(\omega) + A_1 \frac{\Gamma_T}{\omega^2 + \Gamma_T^2} + A_2 \frac{2D_r + \Gamma_T}{\omega^2 + (2D_r + \Gamma_T)^2} \right) \otimes R(\mathbf{q}, \omega) + b(\mathbf{q}) \right] \quad (7.28)$$

The convolution of the resolution function and the Dirac delta gives information on the immobile fraction of water molecules, manifesting as a purely elastic contribution.

The fitting procedure is performed minimizing the χ^2 function and evaluating the reduced χ^2 , $\tilde{\chi}^2$. The fitting is performed utilizing the Minuit routine for Python 3.6 released by CERN [186].

7.2.1 Spectra normalization

Figure 7.3 shows the experimental dataset at the temperature of 10 K for selected scattering vectors (0.3, 0.7, 1.0, 1.2, 1.4 \AA^{-1}). Spectra recorded at the lowest temperature of 10 K are meant to be used to normalize spectra at higher temperatures, giving information on the resolution of the elastic peak. The experimental data are corrected by applying the detailed balance principle of equation (7.19).

A possible resolution function is detected to fit the resolution data recorded at 10 K:

$$R(x) = \frac{norm}{a_1 + a_2} \cdot (a_1 \cdot Lor(x) + a_2 \cdot Gauss(x)) + b \quad (7.29)$$

with x being the energy. The fitting function contains two contributions, a Gaussian

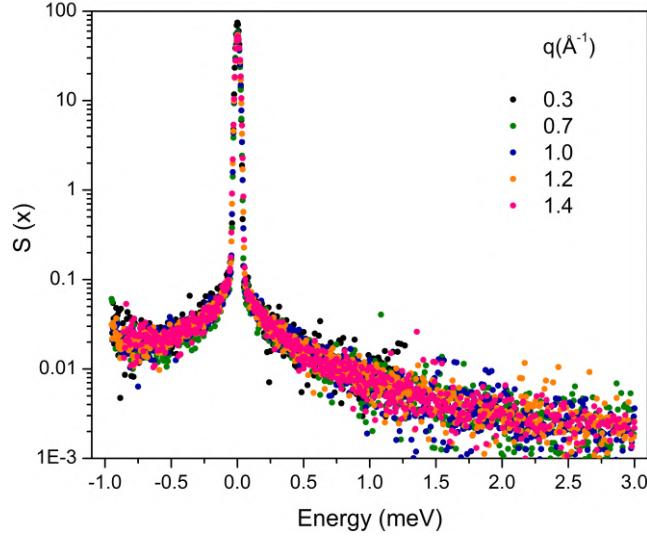


Figure 7.3: Experimental dataset for selected angles at 10 K. Data are reported in logarithmic scale on the y-axis.

and a Lorentzian function, and a flat background, with:

$$Lor(x) = \frac{1}{\pi} \frac{w}{w^2 + (x - (x_0 + \delta x))^2} \quad (7.30)$$

and

$$Gauss(x) = \frac{1}{g^2 \sqrt{2\pi}} \exp\left(-\frac{(x - x_0)^2}{2g^2}\right) \quad (7.31)$$

where $norm$ is a normalization factor, a_1 and a_2 are the weight factor for the Lorentzian function (equation (7.30)) with standard deviation w and energy shift $(x_0 + \delta x)$ and the Gaussian function (equation (7.31)) with standard deviation g and energy shift x_0 , respectively; b is the constant background.

Figure 7.4 shows the fitting procedure results for each \mathbf{q} -vector for the resolution temperature 10 K.

Figure 7.5 reports the residues for each scattering vector as a function of the energy transfer. They show a slight discrepancy around the elastic peak that can be neglected, the resolution function of equation (7.29) can be considered appropriate. Moreover, $\tilde{\chi}^2 \approx 1.5$ as a mean value, evaluated considering the 8 degrees of freedom.

The minimization procedure provides the fitted parameters of the resolution function. They are reported in figure 7.6 for each \mathbf{q} -vector. It can be seen how the values for $\mathbf{q} = 0.2$ and 1.6 \AA^{-1} do not seem to behave consistently with the others, thus they will be excluded from the successive analysis.

7. HYDRATION WATER DYNAMICS IN TAU PROTEIN

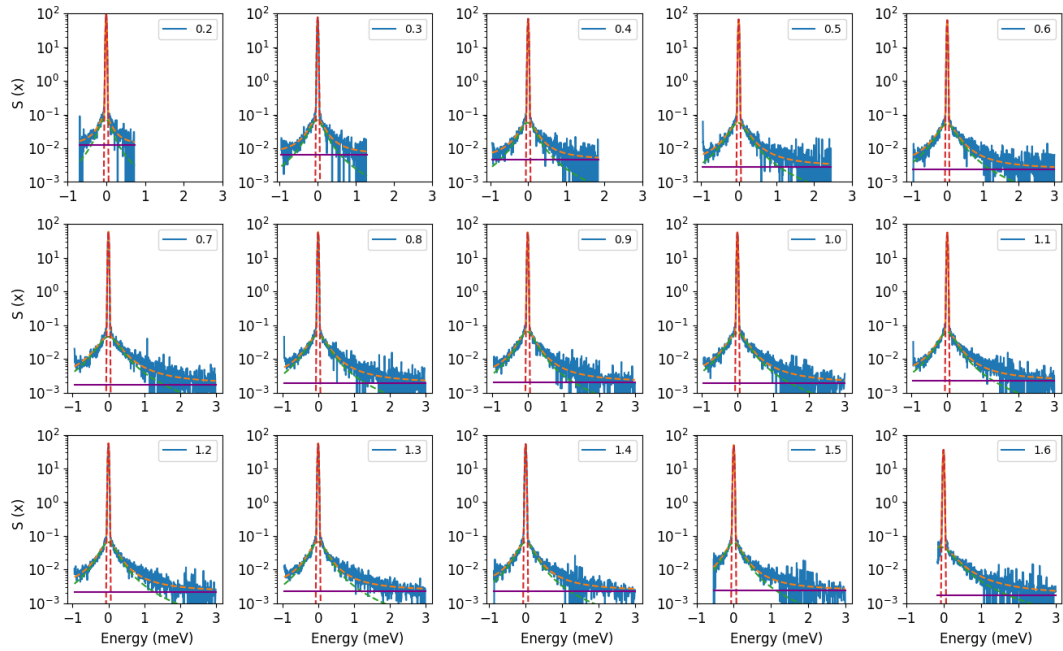


Figure 7.4: Experimental dataset and fitting results for the 15 scattering vectors for the resolution temperature 10 K. *Blue* the experimental dataset, *green* the Lorentzian component, *red* the Gaussian component, *purple* the background, *orange* the fitting function result. Data are reported in semi-logarithmic scale.

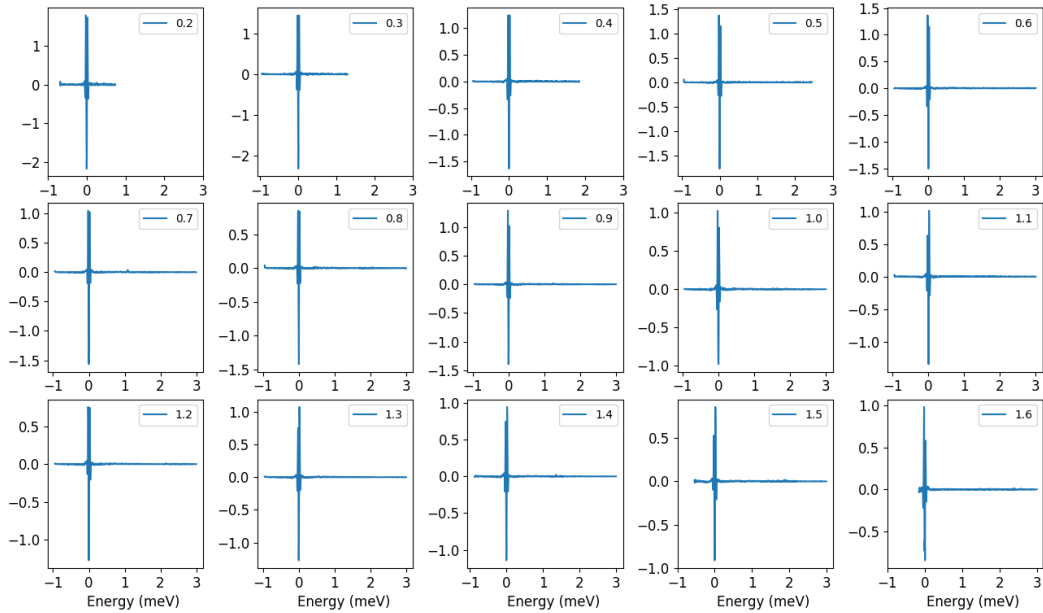


Figure 7.5: Residues for each q -vector of the fitted resolution function at 10 K .

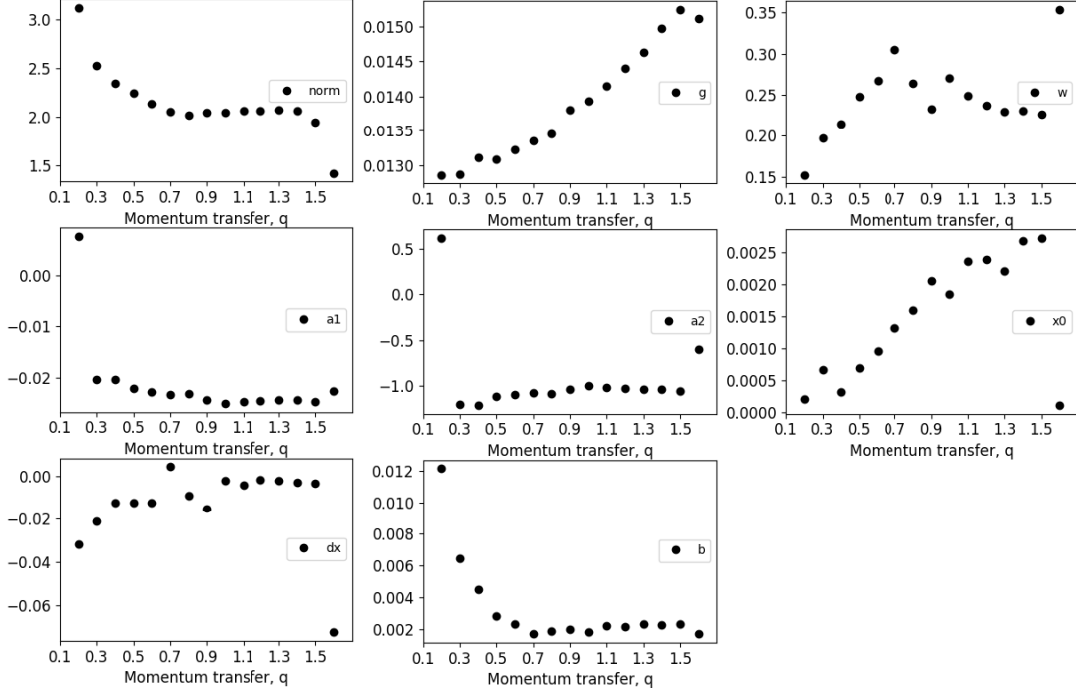


Figure 7.6: Parameters of the fitted resolution function at 10 K as a function of q .

7.2.2 DTAU-H₂O temperature dependence

Figure 7.7 reports the experimental data compared for different temperatures at representative low and high momentum transfer, namely q -vector = 0.6 \AA^{-1} and 1.4 \AA^{-1} . As the temperature increases, the spectra become broader and with a larger quasi-elastic contribution. This is more evident at temperatures greater than 240 K and more at high than low momentum transfer.

The fitting procedure is performed considering as starting parameters for the Minit routine the fitted values of the former temperature for the first q vector. Then, the fitted parameters for one q are used as starting parameters for the following. The heuristic fit q by q confirmed that two Lorentzian-like contributions describe the signal. With this in mind, the model of equation (7.28) can be applied in a one-dimensional q -independent space:

$$S(x) = c \cdot R(x) + \left(a_1 \frac{\Gamma_T}{\pi ((x - x_0)^2 + \Gamma_T^2)} + a_2 \frac{2D_r + \Gamma_T}{\pi ((x - x_0)^2 + (2D_r + \Gamma_T)^2)} \right) \otimes R(x) + b \quad (7.32)$$

The first term, $c \cdot R(x)$, takes into account the immobile fraction of water molecules, moving too slowly for TOFTOF dynamic range and contributing elasti-

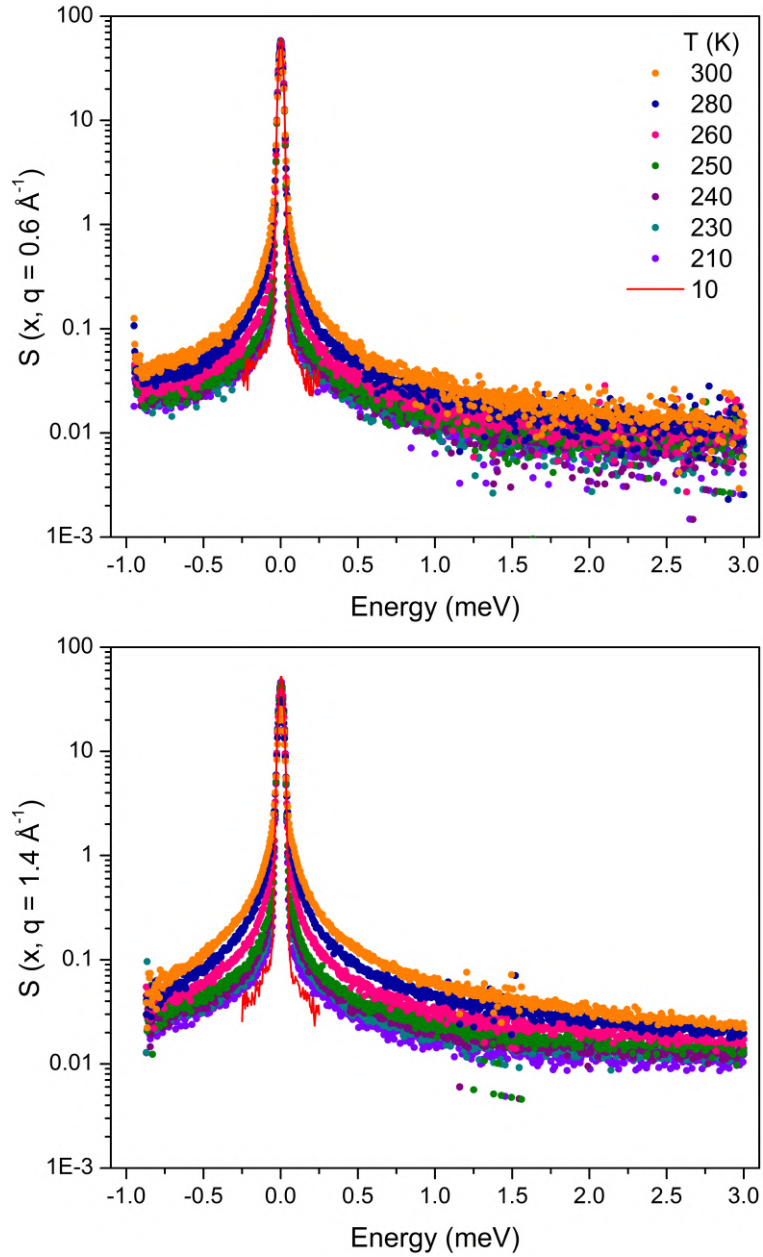


Figure 7.7: Experimental datasets for different temperatures at (*upper panel*) $q = 0.6 \text{ \AA}^{-1}$ and (*lower panel*) $q = 1.4 \text{ \AA}^{-1}$, in semi-logarithmic scale.

cally; the second term account for the translations and rotations of water molecules, considering the correlation of the two motions in the second Lorentzian contribution; b is the flat background, accounting for the instrumental background and motions too fast for TOFTOF time scale.

This fitting approach limited to the energy transfer, x -space, relies on the need- ing of confirming the validity of the suggested model of equation (7.28) for each q

first. The computational time required to perform the fitting is high, mainly because of the convolution operation. Indeed, the shape of these data does not allow us to perform the operation using an optimized routine for Python applying Fast Fourier Transform in the frequency domain. It was, instead, necessary to write a direct convolution function, making the calculation of the integral function and the subsequent minimization computationally expensive. Therefore, optimizing the starting parameters and the validity of the model and performing the fitting procedure for each momentum transfer required a consistent amount of time. Moreover, it is relevant to notice that both translations and rotations have a Lorentzian-like dependence on energy transfer, thus it is not immediate to distinguish and assign the two different dynamical contributions to the QENS spectrum when performing a \mathbf{q} by \mathbf{q} fitting.

Figure 7.8 shows an example of the fitting results at two temperatures, 230 K and 280 K, for $\mathbf{q} = 0.6 \text{ \AA}^{-1}$.

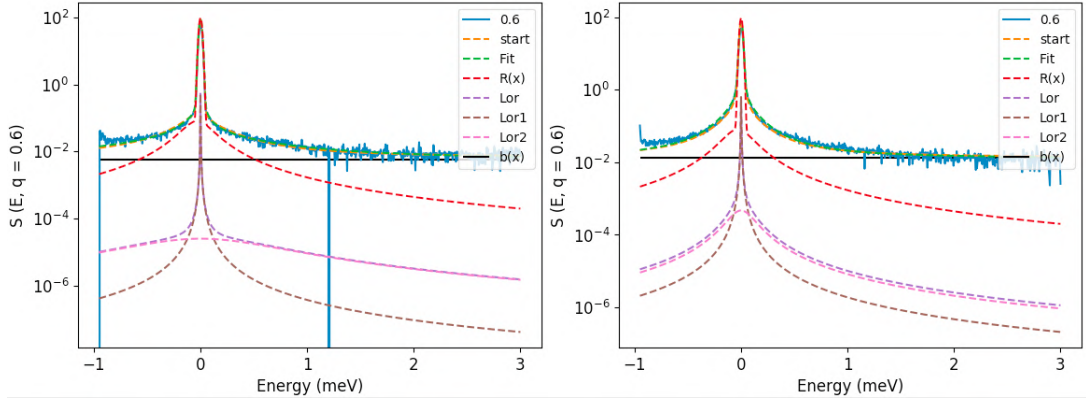


Figure 7.8: Experimental dataset and fitting results for $\mathbf{q} = 0.6 \text{ \AA}^{-1}$ at (*left*) $T = 230 \text{ K}$ and (*right*) $T = 280 \text{ K}$. Data are reported in semi-logarithmic scale.

It can be seen that the model is consistent with our data and the minimization process correctly fits the experimental spectra.

In figure 7.9, the parameters describing the roto-translational contributions resulting from the fitting procedure at $T = 280 \text{ K}$ are reported as a function of \mathbf{q} , representative for the others.

It can be seen that the suggested model is consistent with the data. Γ_T manifests a \mathbf{q} -dependent behavior, as expected, while the opposite holds for D_r . Indeed, Γ_T has an increasing trend as a function of \mathbf{q} , while D_r oscillates around a constant value. The intensities, a_1 and a_2 , resembles correctly the first two spherical Bessel functions, of order $0th$ and $1st$ respectively, with a_1 starting from a non-zero value and maintaining a constant value over a broad \mathbf{q} -range and then decreasing, and a_2

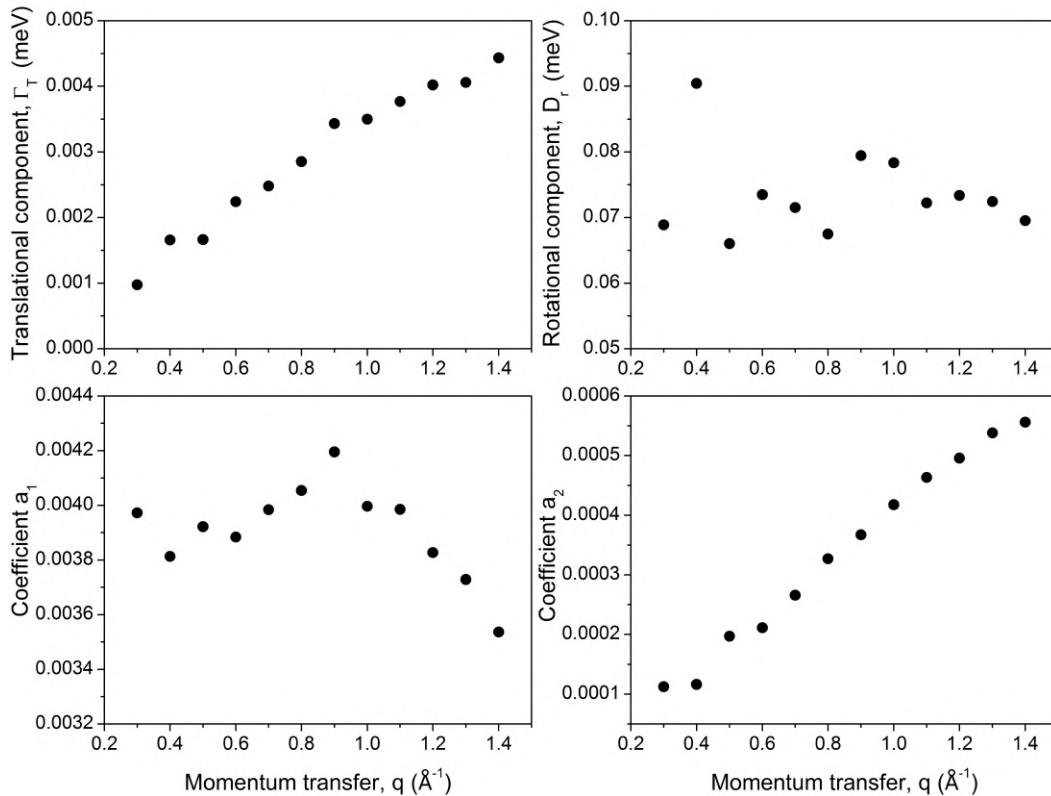


Figure 7.9: Parameters resulting from the fitting procedure for the translational and rotational motions at $T = 280$ K as a function of q .

starting from zero and increasing at increasing momentum transfer.

These dependencies on the q -vector are a confirmation of the validity of our model to describe hydration water dynamics in tau protein at the energies of TOTOF resolution and sustain the component assignment to the Lorentzian contributions, although some adjustments are needed to ensure better stability to the fitting procedure. As expected, rotational motions around the center of mass, accounted by D_r , do not depend on the momentum transfer. That is because rotations are a confined motion depending just on the nature of the water molecule H-O bond. Translations of the center of mass, instead, increase with increasing momentum transfer.

More interesting it is the analysis of hydration water dynamics in tau protein as a function of temperature. Focusing on the dynamical parameters describing translational motion, Γ_T , and purely elastic contribution of the water molecules that appear immobile, c , figure 7.10 and figure 7.11 show the fitted parameters at increasing temperature at two selected q -vectors, one at low and one at high scattering angle, respectively.

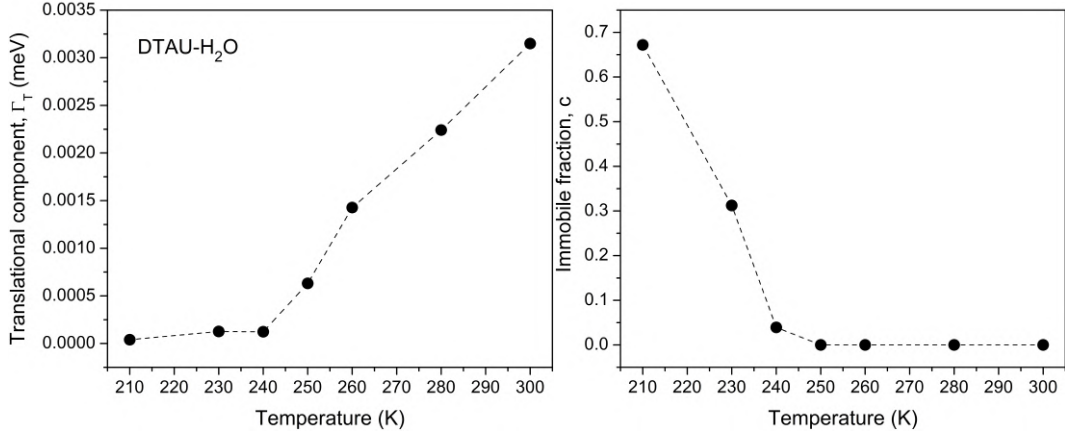


Figure 7.10: Fitted parameters (*left*) Γ_T for the translational motion and (*right*) c for the immobile fraction of hydration water molecules in perdeuterated tau for $\mathbf{q} = 0.6 \text{ \AA}^{-1}$ as a function of the temperature.

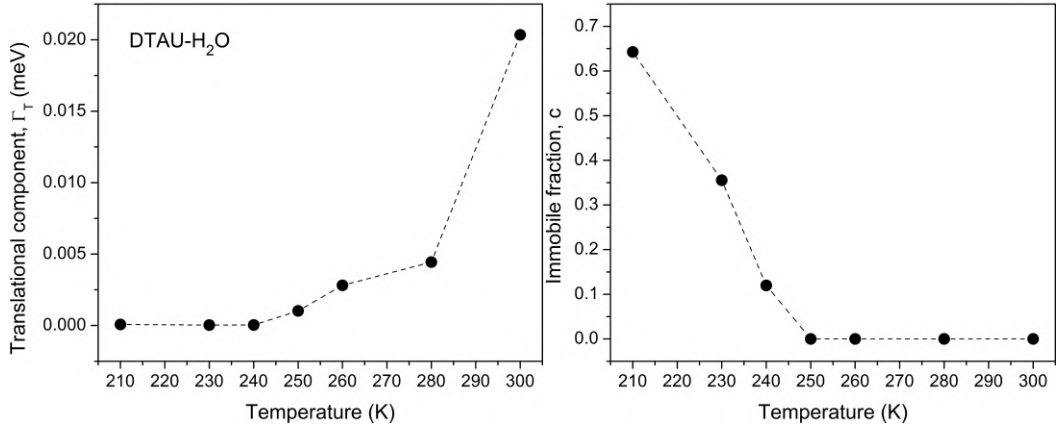


Figure 7.11: Fitted parameters (*left*) Γ_T for the translational motion and (*right*) c for the immobile fraction of hydration water molecules in perdeuterated tau for $\mathbf{q} = 1.4 \text{ \AA}^{-1}$ as a function of the temperature.

In both cases the translational parameter Γ_T presents an increasing trend at increasing temperature, with a specific slope change at temperature greater than 240 K. On the contrary, the fraction of molecules that appear immobile on the TOFTOF time scale is high at the lowest temperatures and approaches zero from 250 K onward, consistently with the onset of faster translational dynamics.

The complete characterization of hydration water dynamics in DTAU should now be persecuted ensuring the stability of the model and applying it in the two-dimensional (\mathbf{q}, ω) -space, explicitly introducing in the fitting function of equation (7.32) the \mathbf{q} -dependencies of the parameters, as supposed in the model of equation (7.28).

7.2.3 Discussion and perspective

The results here presented are in keeping with previous findings on protein dynamical transition and onset of larger anharmonic motions for a temperature $T_d \approx 240$ K. To better focus on this comparison, figure 7.12 from Schirò et al. [61] shows the low-temperature behavior of the mean-square displacements of tau protein in the presence and in the absence of water.

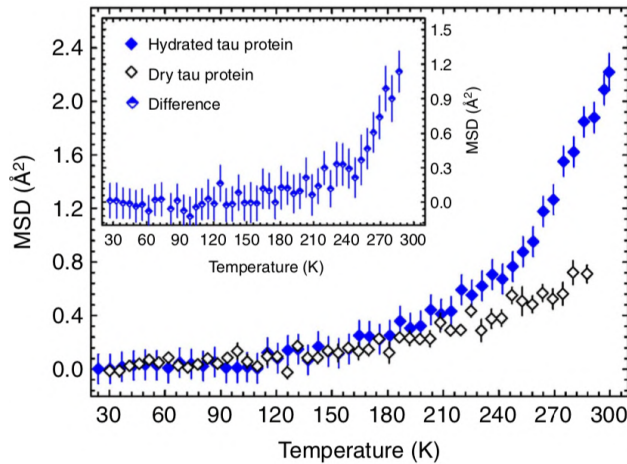


Figure 7.12: MSDs of htau40 hydrated in D_2O (full blue diamonds) and dry (open black diamonds), measured by elastic incoherent neutron scattering at the backscattering spectrometer IN16 (ILL, Grenoble). *Inset:* the MSD difference between the hydrated and the dry protein highlights an onset of large-amplitude protein motions at around 240 K. Figure adapted from [61].

It can be highlighted comparing the tau protein behavior in figure 7.12 and water behavior presented in figures 7.10 and 7.11 that the onset of water translational motion and the onset of dynamical transition in tau protein are related. The behavior exhibited by the elastic contribution, c , the analogous of the mean-square displacements, gives us the information that at temperatures greater than 240 K nothing appear immobile anymore, on the time scale probed by TOFTOF. Moreover, by comparing the dry and the hydrated tau samples previously measured [61], it can be seen how the presence of hydration water enhances the protein motion.

The results obtained for the hydration water in tau protein at the energy resolution of TOFTOF and presented here are comparable to what has been seen for the hydration water dynamics in the intrinsically disordered tau and in the folded maltose binding protein (MBP) at the backscattering spectrometer SPHERES, characterized by an energy resolution of $0.7 \mu\text{eV}$ (see figure 7.13).

Comparing these results on data collected at SPHERES with our results presented in figures 7.10 and 7.11 and having in mind that the backscattering spec-

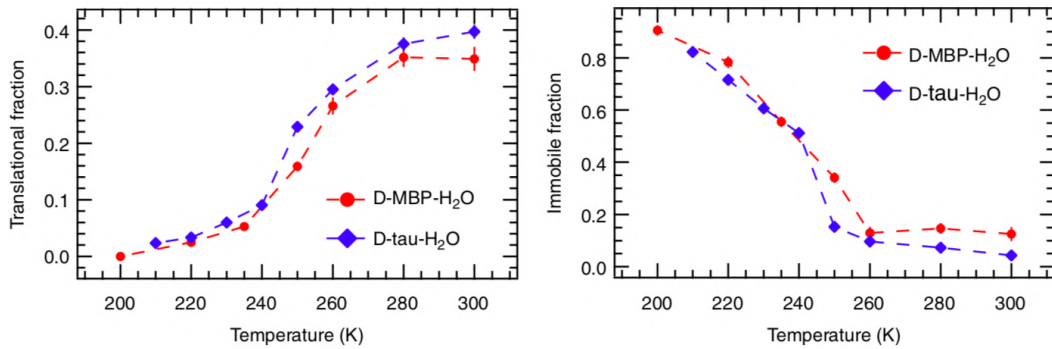


Figure 7.13: Fractions of different dynamic contributions to the quasi-elastic spectra as a function of temperature: (*left*) center of mass translation of water molecules; (*right*) water molecules not moving in the dynamic window investigated. Data recorded at the backscattering spectrometer SPHERES (MLZ, Garching). Figure adapted from [61].

trometer has higher resolution with respect to the time-of-flight spectrometer, it can be pointed out that the temperature behavior of both the translational component and the immobile fraction follows the same path. At the onset of faster translations corresponds the zero-value of molecules that do not seem to move on the probed time scale and this happens at a temperature of about 240 K. It is peculiar that water translational motion starts to occur at the same temperature at which the dynamical transition sets in in the protein sample and correspondingly the elastic contribution reaches zero-value, being an indication of the influence of hydration water dynamics on the onset of larger diffusive motions in the protein.

Interestingly, the mean-square displacements have been reported to increase at $T \approx 240$ K also in water hydrating perdeuterated tau in its aggregate fiber form [93] and in water hydrating both disordered tau and folded MBP (data collected at the backscattering spectrometer IN16), where it was highlighted a tighter coupling with hydration-water dynamics for an intrinsically disordered than for a folded protein [92].

To complete this analogy and have a comprehensive view of the hydration water - protein complex and their relation, and to better understand their dynamic coupling, it is necessary to complete this analysis by performing a global fitting in the two-dimensional (\mathbf{q}, E) -space, to consider explicitly the \mathbf{q} -dependence of the parameters representing the roto-translational motions. This will be the future goal of this work.

Conclusions

The overall results presented in this doctoral thesis show that methods of spin-label cw- and FT-EPR are particularly suitable to get insights in differing molecular properties of cryogenically frozen biosystems. Nucleic acids, proteins, carbohydrates and lipids, together with water, are fundamental components of living matter. We focused on interesting examples of macromolecules and lipid aggregates, such as model membranes and micelles of characteristic lipid composition (single lipid species of saturated and unsaturated PCs, PEG-grafted lipid dispersions, mixtures of Lyso-PPC and DPPC, PEG-grafted lipid micelles and Lyso-PPC micelles), natural membranes (Na⁺-K⁺-ATPase), and proteins (HSA, β -LG, htau40). The use of low, cryogenic temperatures highlights dynamic features and solvent properties as well as the solvent-biosystem mutual influence.

D₂O-ESEEM and cw-EPR at 77 K have been employed to study the phase behavior of chain-labelled DPPC/PEG:2000-DPPE and DPPC/Lyso-PPC dispersions over the whole range of relative composition (0 - 100 mol%). By detecting the variation of solvent accessibility and environmental polarity at different depth along the hydrocarbon chain, micelles formation has been studied on increasing the concentration of the micelle-forming lipids (polymer-lipids or Lyso-lipids) incorporated in DPPC bilayers. Emphasis was given to the description of solvent permeation and polarity profiles in SSL composed by DPPC and 2 mol% of PEG:2000-DPPC, in interdigitated lamellae formed by DPPC and equimolar content of Lyso-PPC, and in micelles of Lyso-PPC or PEG:2000-DPPE.

Compared to those in DPPC bilayers, the sigmoidal profiles in SSL showed increased hydrophobicity at both the polar/apolar interface and the chain termini, and a broader transition that is shifted toward the interface. In both polymer-lipid and Lyso-PPC micelles, solvent exposure and polarity decreased on going down the

chain, and the chain termini were accessible to water. However, PEG-micelles exhibited lower solvent accessibility and polarity at any labeling position with respect to the smaller Lyso-micelles. The results obtained at low temperature by means of ESEEM and cw-EPR in lipid aggregates containing PEG-lipids can be relevant for biotechnological applications, for the interaction of biomacromolecules (peptides and proteins) with optimized lipid aggregates and for the interaction (binding, encapsulation, transport and release) of ligands and active compounds with smart drug-carriers. Indeed, PEG-lipids impart steric protection to biomaterials and both SSL and PEG-lipid micelles are successfully used in drug-delivery.

As said, at intermediate content Lyso-lipids are able to induce chain interdigitation in DPPC membranes. Similarly, a lamellar phase with interdigitated chains is also formed in DPPC in the presence of ethanol (60% v/v). At a variance with the sigmoidal transmembrane water penetration and polarity profiles delineated in DPPC bilayers and in SSL, almost uniform profiles of high solvent accessibility and polarity across the hydrocarbon zone were recorded in the interdigitated phases. Moreover, the two types of interdigitated phases manifested differences in the packing density as the chains resulted to be less densely packed in the presence of ethanol than in the presence of the Lyso-lipids.

The interaction of spin-labeled bufadienolides with Na^+, K^+ -ATPase membranes has also been addressed by using D_2O -ESEEM and cw-EPR at 77 K. These are cardiotonic steroids and specific inhibitors of the sodium pump, with their binding site overlapping with the extracellular access channel for cations. By employing steroids with different lengths of the spacer arm between the EPR-active nitroxide group and the steroid core, and with five- as well as six-membered nitroxide rings, it was found that the vestibule leading to the ligands binding site is of high polarity, exposed to water and allows various degrees of mobility of the ligands.

Another issue discussed in this thesis is the dynamics at low temperatures (77 - 270 K) of self-assembled lipid aggregates and proteins and the influence of the hydration degree. Cw-EPR and two-pulse ED-EPR spectra indicated that segmental librational motion occurs in the low-temperature phases of the investigated samples. Rapid torsional oscillations of small amplitudes have been characterized in fully hydrated high- T_m saturated DPPC bilayers and low- T_m unsaturated POPC and DOPC bilayers, as well as in interdigitated lipid aggregates composed by DPPC/Lyso-PPC mixtures or DPPC/etOH.

Hydration affected differently the characteristics of the librational motion in proteins and in lipid bilayers. Librations were of very small amplitudes and temperature independent in lyophilized β -LG and HSA, whereas they were of larger amplitudes which increased with temperature in proteins even at low-water content. In DPPC

bilayers, the polar/apolar region showed restricted librational dynamics in the dehydrated state and it became progressively more rapid upon increasing the water content. In contrast, librations of considerable amplitudes occurred in the DPPC hydrocarbon interior almost independently from the hydration condition. This is a new and interesting EPR result: the membrane midplane regions that are of low polarity and inaccessible to water, exhibit segmental librations even in the dehydrated state.

Another remarkable feature observed in all the investigated hydrated biosystems (lipid bilayers, interdigitated lamellae and proteins) at cryogenic temperatures is that the mean-square librational amplitudes started to increase more rapidly for temperatures around 200 K (190 – 240 K). This behavior is similar to the temperature dependence of the mean-square displacement measured in diffraction studies. It has been associated with the onset of dynamical transition and the crossing of low energy barriers of about 20 kJ/mol (13 – 32 kJ/mol). The most striking feature evidenced by the present EPR results is that a dynamical transition occurs also in membrane model systems in the absence of water.

Water dynamics affects at different extent various biomacromolecules. In the last chapter of this thesis, the analysis as a function of temperature of the hydration water in ht40 from quasi-elastic neutron scattering data collected at TOFTOF has been reported. Hydration water manifested the onset of translational motion at the temperature of about 240 K, which coincides with the protein dynamical transition temperature. This strongly suggests that water dynamics is coupled with protein dynamics.

Biophysical studies at cryogenic temperatures allow an in-depth characterization of lipid membranes and macromolecules, that are generally studied at higher temperatures. The obtained results on the structure, dynamics and molecular properties contribute to clarify still open aspects on the structure/dynamics/function relationships in biosystems and on the role played by water in activating physiologically important processes.

References

- [1] Tycko R., *NMR at low and ultra-low temperatures*, Accounts of Chemical Research 46:9 (2013) 1923-1932
- [2] Lengyel J., Hnath E., Storms M., Wohlfarth T., *Towards an integrative structural biology approach: combining Cryo-TEM, X-ray crystallography, and NMR*, Journal of Structural and Functional Genomics 15 (2014) 117-124
- [3] Kwon H., Langan P.S., Coates L., Raven E.L., Moody P.C.E., *The rise of neutron cryo-crystallography*, Acta Crystallographica Section D D74 (2018) 792-799
- [4] Fan Y., Wang Y., *Applications of small-angle X-ray scattering/small angle neutron scattering and cryogenic transmission electron microscopy to understand self-assembly of surfactants*, Current Opinion in Colloid & Interface Science 42 (2019) 1-16
- [5] Oslan S.N.H., Halim M., Ramle N.A., Saad M.Z., Tan J.S., Kapri M.R., Ariff A.B., *Improved stability of live attenuated vaccine *gdhA* derivative *Pasteurella multocida B:2* by freeze drying method for use as animal vaccine*, Cryobiology 79 (2017) 1-8
- [6] Taylor M.J., Weegman B.P., Baicu S.C., Giwa S.E., *New approaches to cryopreservation of cells, tissues, and organs*, Transfusion Medicine and Hemotherapy 46 (2019) 197-215
- [7] Xin Y., Kielar C., Zhu S., Sikeler C., Xu X., Möser C., Grundmeier G., Liedl T., Heuer-Jungemann A., Smith D.M., Keller A., *Cryopreservation of DNA origami nanostructures*, Small 16 (2020) 1905959

REFERENCES

- [8] Wolkers W.F., Oldenhof H. (eds.), *Cryopreservation and Freeze-Drying Protocols*, Springer, New York, Heidelberg, Dordrecht, London (2021)
- [9] Taouzinet L., Fatmi S., Lahiani-Skiba M., Skiba M., Iguer-Ouada M., *Encapsulation nanotechnology in sperm cryopreservation: systems preparation methods and antioxidants enhanced delivery*, *Cryoletters* 42:1 (2021) 1-12
- [10] Kar L., Ney-Igner E., Freed J.H., *Electron spin resonance and electron spin-echo study of oriented multilayers of L_{α} -dipalmitoylphosphatidylcholine water systems* *Biophysical Journal* 48 (1985) 569-595
- [11] Berliner L.J., Reuben J. (eds.), *Spin labeling theory and applications*, Plenum Press, New York (1989)
- [12] Schweiger A., Jeschke G., *Principles of pulse electron paramagnetic resonance*, Oxford University Press, New York (2001)
- [13] Klare J.P., Steinhoff H.J., *Spin labeling EPR*, *Photosynthesis Research* 102:2-3 (2009) 377-390
- [14] Marsh D., *Spin-Label Electron Paramagnetic Resonance Spectroscopy* (1st ed.), CRC Press, Boca Raton (2019)
- [15] Bartucci R., Erilov D.A., Guzzi R., Sportelli L., Dzuba S.A., Marsh D., *Time-resolved electron spin resonance studies of spin-labelled lipids in membranes*, *Chemistry and Physics of Lipids* 141 (2006) 142-157
- [16] Erilov D.A., Bartucci R., Guzzi R., Marsh D., Dzuba S.A., Sportelli L., *Librational motion of spin-labeled lipids in high-cholesterol containing membranes from echo-detected EPR spectra*, *Biophysical Journal* 87 (2004) 3873-3881
- [17] Erilov D.A., Bartucci R., Guzzi R., Shubin A.A., Maryasov A.G., Marsh D., Dzuba S.A., Sportelli L., *Water concentration profiles in membranes measured by ESEEM of spin-labeled lipids*, *The Journal of Physical Chemistry B* 109 (2005) 12003-12013
- [18] Carmieli R., Papo N., Zimmermann H., Potapov A., Shai Y., Goldfarb D., *Utilizing ESEEM spectroscopy to locate the position of specific regions of membrane-active peptides within model membranes*, *Biophysical Journal* 90 (2006) 492-505
- [19] Volkov A., Dockter C., Bund T., Paulsen H., Jeschke G., *Pulsed EPR determination of water accessibility to spin-labeled amino acid residues in LHCIIB*, *Biophysical Journal* 96 (2009) 1124-1141

REFERENCES

- [20] Cieslak J.A., Focia P.J., Gross A., *Electron Spin-Echo Envelope Modulation (ESEEM) reveals water and phosphate interactions with the KcsA potassium channel*, *Biochemistry* 49 (2010) 1486-1494
- [21] Urban L., Steinhoff H.J., *Hydrogen bonding to the nitroxide of protein bound spin labels*, *Molecular Physics* 111 (2013) 2873-2881
- [22] Guzzi R., Bartucci R., Marsh D., *Heterogeneity of protein substates visualized by spin-label EPR*, *Biophysical Journal* 106:3 (2014) 716-722
- [23] Dzuba S.A., Marsh D., *ESEEM of spin labels to study intermolecular interactions, molecular assembly and conformation* in: *Electron Paramagnetic Resonance: Volume 24*, The Royal Society of Chemistry (2015)
- [24] Cevc G., Marsh D., *Phospholipid Bilayers. Physical Principles and Models*, Wiley-Interscience, New York (1987)
- [25] Calero C., Franzese G., *Membranes with different hydration levels: the interface between bound and unbound hydration water*, *Journal of Molecular Liquids* 273 (2019) 488-496
- [26] Dzuba S.A., *Libration motion of guest spin probe molecules in organic glasses: CW-EPR and electron spin echo study*, *Spectrochimica Acta A* 56 (2000) 227-234
- [27] Kirilina E.P., Dzuba S.A., Maryasov A.G., Tsvetkov Yu.D., *Librational dynamics of nitroxide molecules in a molecular glass studied by echo-detected EPR*, *Applied Magnetic Resonance* 21 (2001) 203-221
- [28] Erilov D.A., Bartucci R., Guzzi R., Marsh D., Dzuba S.A., Sportelli L., *Echo-detected electron paramagnetic resonance spectra of spin-labeled lipids in membrane model systems*, *The Journal of Physical Chemistry B* 108 (2004) 4501-4507
- [29] Fenimore P.W., Frauenfelder H., McMahon B.H., Young R.D., *Bulk-solvent and hydration-shell fluctuations, similar to alpha- and beta-fluctuations in glasses, control protein motions and functions*, *Proceedings of the National Academy of Sciences USA* 101 (2004) 14408-14413
- [30] Bartucci R., Guzzi R., De Zotti M., Toniolo C., Sportelli L., Marsh D., *Backbone dynamics of alamethicin bound to lipid membranes: spin-echo electron paramagnetic resonance of TOAC-spin labels*, *Biophysical Journal* 94 (2008) 2698-2705

REFERENCES

- [31] Guzzi R., Bartucci R., Sportelli L., Esmann M., Marsh D., *Conformational heterogeneity and spin-labeled -SH groups: pulsed EPR of Na,K-ATPase*, *Biochemistry* 48:35 (2009) 8343-8354
- [32] Guzzi R., Bartucci R., Esmann M., Marsh D., *Lipid librations at the interface with the Na,K-ATPase*, *Biophysical Journal* 108 (2015) 2825-2832
- [33] Konov K.B., Isaev N.P., Dzuba S.A., *Low-temperature molecular motions in lipid bilayers in the presence of sugars: insights into cryoprotective mechanisms*, *The Journal of Physical Chemistry B* 118 (2014) 12478-12485
- [34] Dzuba S.A., Kirilina E.P., Salnikov E.S., *On the possible manifestation of harmonic-anharmonic dynamical transition in glassy media in electron paramagnetic resonance of nitroxide spin probes*, *The Journal of Chemical Physics* 125:5 (2006) 054502
- [35] Scarpelli F., Bartucci R., Sportelli L., Guzzi R., *Solvent effect on librational dynamics of spin-labelled haemoglobin by ED- and CW-EPR*, *European Biophysical Journal* 40 (2011) 273-279
- [36] Guzzi R., Babavali M., Bartucci R., Sportelli L., Esmann M., Marsh D., *Spin-echo EPR of Na⁺,K⁺-ATPase unfolding by urea*, *Biochimica et Biophysica Acta* 1808 (2011) 1618-1628
- [37] Guzzi R., Rizzuti B., Bartucci R., *Dynamics and binding affinity of spin-labeled stearic acids in β -Lactoglobulin: evidences from EPR spectroscopy and molecular dynamics simulation*, *The Journal of Physical Chemistry B* 116 (2012) 11608-11615
- [38] Surovtsev N.V., Ivanisenko N.V., Kirillov K.Y., Dzuba S.A., *Low-temperature dynamical and structural properties of saturated and monounsaturated phospholipid bilayers revealed by Raman and spin-label EPR spectroscopy*, *The Journal of Physical Chemistry B* 116 (2012) 8139-8144
- [39] Marsh D., Bartucci R., Guzzi R., Sportelli L., Esmann M., *Librational fluctuations in protein glasses*, *Biochimica et Biophysica Acta: Proteins Proteomics* 1834 (2013) 1591-1595
- [40] Syryamina V.N., Dzuba S.A., *Dynamical transitions at low temperatures in the nearest hydration shell of phospholipid bilayers*, *The Journal of Physical Chemistry B* 121:5 (2017) 1026-1032

REFERENCES

- [41] Aloï E., Oranges M., Guzzi R., Bartucci R., *Low-temperature dynamics of chain-labeled lipids in ester- and ether-linked phosphatidylcholine membranes*, The Journal of Physical Chemistry B 121 (2017) 9239-9246
- [42] Doster W., Cusack S., Petry W., *Dynamical transition of myoglobin revealed by inelastic neutron scattering*, Nature 337 (1989) 54-756
- [43] Ferrand M., Petry W., Dianoux A.J., Zaccai G., *Dynamical transition of bacteriorhodopsin in purple membranes revealed by neutron scattering: a relation between structure, dynamics and function*, Physica A: Statistical Mechanics and its Applications, 201 (1993) 425-429
- [44] Gabel F., Bicout D., Lehnert U., Tehei M., Weik M., Zaccai G., *Protein dynamics studied by neutron scattering* Quarterly Reviews of Biophysics 35:4 (2002) 327-367
- [45] Fitter J., Lechner R.E., Dencher N.A., *Interactions of hydration water and biological membranes studied by neutron scattering*, The Journal of Physical Chemistry B 103 (1999) 8036-8050
- [46] Ringe D., Petsko G.A., *The 'glass transition' in protein dynamics: what it is, why it occurs, and how to exploit it* Biophysical Chemistry 105 (2003) 667-680
- [47] Wood K., Plazanet M., Gabel F., Kessler B., Oesterhelt D., Tobias D.J., Zaccai G., Weik M., *Coupling of protein and hydration-water dynamics in biological membranes*, Proceedings of the National Academy of Sciences USA 104:46 (2007) 18049-18054
- [48] Doxastakis M., Garcia Sakai V., Ohtake S., Maranas J.K., de Pablo J.J., *A molecular view of melting in anhydrous phospholipidic membranes*, Biophysical Journal 92 (2007) 147-161
- [49] Frauenfelder H., Chen G., Berendzen J., Fenimore P.W., Jansson H., McMahon B.H., Stroer I.R., Swenson J., Young R.D., *A unified model of protein dynamics*, Proceedings of the National Academy of Sciences USA 106 (2009) 5129-5134
- [50] Doster W., *The protein-solvent glass transition*, Biochimica et Biophysica Acta: Proteins Proteomics 1804 (2010) 3-14
- [51] Schirò G., Natali F., Cupane A., *Physical origin of anharmonic dynamics in proteins: new insights from resolution-dependent neutron scattering on homomeric polypeptides*, Physical Review Letters 109 (2012) 128102

REFERENCES

- [52] Peters J., Marion J., Natali F., Kats E., Bicout D.J., *The dynamical transition of lipid multi-lamellar bilayers as a matter of cooperativity*, The Journal of Physical Chemistry B 121 (2017) 6860-6868
- [53] Bartucci R., Guzzi R., Marsh D., Sportelli L., *Chain dynamics in the low-temperature phases of lipid membranes by electron spin-echo spectroscopy*, Journal of Magnetic Resonance 162:2 (2003) 371-379
- [54] Lewandowski J.R., Halse M.E., Blackledge M., Emsley L., *Direct observation of hierarchical protein dynamics*, Science 348 (2015) 578-581
- [55] Zanatta M., Tavagnacco L., Buratti E., Bertoldo M., Natali F., Chiessi E., Orecchini A., Zaccarelli E., *Evidence of a low-temperature dynamical transition in concentrated microgels*, Science Advances 4 (2018) eaat5895
- [56] Bizzarri A.R., Cannistraro S., *Molecular dynamics simulation evidence of anomalous diffusion of protein hydration water*, Physical Review E 53:4 (1996) 3040-3043
- [57] Tournier A.L., Xu J., Smith J.C., *Translational hydration water dynamics drives the protein glass transition*, Biophysical Journal 85:3 (2003) 1871-1875
- [58] Ball P., *Water as an active constituent in cell biology*, Chemical Reviews 108:1 (2008) 74-108
- [59] Schirò G., Caronna C., Natali F., Cupane A., *Molecular origin and hydration dependence of protein anharmonicity: an elastic neutron scattering study*, Physical Chemistry Chemical Physics 12 (2010) 10215-10220
- [60] Bellissent-Funel M.-C., Hassanali A., Havenith M., Henschman R., Pohl P., Sterpone F., van der Spoel D., Xu Y., Garcia A.E., *Water determines the structure and dynamics of proteins*, Chemical Reviews 116:13 (2016) 7673-7697
- [61] Schirò G., Fichou Y., Gallat F.-X., Wood K., Gabel F., Moulin M., Härtlein M., Heyden M., Colletier J.-P., Orecchini A., Paciaroni A., Wuttke J., Tobias D.J., Weik M., *Translational diffusion of hydration water correlates with functional motions in folded and intrinsically disordered proteins*, Nature Communications 6 (2015) 6490
- [62] König S., Bayerl T.M., Coddens G., Richter D., Sackmann E., *Hydration dependence of chain dynamics and local diffusion in L_{α} -dipalmitoylphosphatidylcholine multilayers studied by incoherent quasi-elastic neutron scattering*, Biophysical Journal 68:5 (1995) 1871-1880

REFERENCES

- [63] Magazù S., Migliardo F., *Dynamics of biological macromolecules by neutron scattering*, Bentham Science Publishers: University of Messina, Italy (2011)
- [64] van Meer G., Voelker D.R., Feigenson G.W., *Membrane lipids: where they are and how they behave*, *Nature Reviews Molecular Cell Biology* 9 (2008) 112-124
- [65] Lasic D.D., *Liposomes: from physics to applications*, Elsevier, Amsterdam (1993)
- [66] Nag O.K., Awasthi V., *Surface engineering of liposomes for stealth behavior*, *Pharmaceutics* 5 (2013) 542-569
- [67] Suk J.S., Xu Q., Kim N., Hanes J., Ensign L.M., *PEGylation as a strategy for improving nanoparticle-based drug and gene delivery*, *Advanced Drug Delivery Reviews* 99 (2016) 28-51
- [68] Mastrotto F., Brazzale C., Bellato F., De Martin S., Grange G., Mahmoudzadeh M., Magarkar A., Bunker A., Salmaso S., Caliceti P., *In vitro and in vivo behavior of liposomes decorated with PEGs with different chemical features*, *Molecular Pharmaceutics* 17 (2020) 472-487
- [69] Lasic D.D., Martin L., *Stealth Liposomes*, CRC Press, Boca Raton (1995)
- [70] Gill K.K., Kaddoumi A., Nazzal A., *PEG-lipid micelles as drug carriers: physio-chemical attributes, formulation principles and biological implication*, *Journal of Drug Targeting* 23 (2015) 222-231
- [71] Fuller N., Rand R., *The influence of lysolipids on the spontaneous curvature and bending elasticity of phospholipid membranes*, *Biophysical Journal* 81 (2001) 243-254
- [72] Ohata H., Tanaka K., Maeyama N., Ikeuchi T., Kamada A., Yamamoto M., Momose K., *Physiological and pharmacological role of lysophosphatidic acid as modulator in mechanotransduction*, *Japanese Journal of Pharmacology* 87 (2001) 171-176
- [73] Luquain C., Sciorra V., Morris A., *Lysophosphatidic acid signaling: how a small lipid does big things*, *Trends in Biochemical Sciences* 28 (2003) 377-383
- [74] Lee Y., Chan S.I., *Effect of lysolecithin on the structure and permeability of lecithin bilayer vesicles*, *Biochemistry* 16 (1977) 1303-1309

REFERENCES

- [75] van Echteld C.J.A., De Kruijff B., Mandersloot J.G., De Gier J., *Effects of lyso- phosphatidylcholines on phosphatidylcholine and phosphatidylcholine/cholesterol liposome systems as revealed by ^{31}P -NMR, electron microscopy and permeability studies*, *Biochimica et Biophysica Acta* 649 (1981) 211-220
- [76] Bhamidipati S.P., Hamilton J.A., *Interactions of Lyso 1- Palmitoylphosphatidylcholine with phospholipids: a ^{13}C and ^{31}P -NMR study*, *Biochemistry* 34 (1995) 5666-5677
- [77] McIntosh T.J., Advani S., Burton R.E., Zhelev D.V., Needham D., Simon S.A., *Experimental tests for protrusion and undulation pressures in phospholipid bilayers*, *Biochemistry* 34 (1995) 8520-8532
- [78] Lu J.Z., Xu Y.M., Chen J.W., Huang F., *Effect of lysophosphatidylcholine on behaviour and structure of phosphatidylcholine liposomes*, *Science in China Series C-Life Sciences* 40 (1997) 622-629
- [79] Mishima K., Nakajima M., Ogihara T., *Effects of lysophospholipids on membrane order of phosphatidylcholine*, *Colloids and Surfaces B: Biointerfaces* 33 (2004) 185-189
- [80] Pantusa M., Sportelli L., Bartucci R., *Phase behaviour of DPPC/Lyso-PPC mixtures by spin-label ESR and spectrophotometry*, *Spectroscopy* 22 (2008) 153-163
- [81] Anyarambhatla G., Needham D., *Enhancement of the phase transition permeability of DPPC liposomes by incorporation of MPPC: a new temperature-sensitive liposome for use with mild hyperthermia*, *Journal of Liposome Research* 9:4 (1999) 491-506
- [82] Needham D., Anyarambhatla G., Kong G., Dewhirst M.W., *A new temperature-sensitive liposome for use with mild hyperthermia: characterization and testing in a human tumor xenograft model*, *Cancer Research* 60 (2000) 1197-1201
- [83] Lu J.Z., Hao Y.H., Chen J.W., *Effect of cholesterol on the formation of an interdigitated gel phase in lysophosphatidylcholine and phosphatidylcholine binary mixtures*, *The Journal of Biochemistry* 129 (2001) 891-898
- [84] Slater J.L., Huang C.H., *Interdigitated bilayer membranes*, *Progress in Lipid Research* 27 (1988) 325-359

REFERENCES

- [85] Marsh D., *Handbook of Lipid Bilayers*, 2nd ed., Taylor and Francis, New York (2012)
- [86] Picas L., Rico F., Scheuring S., *Direct measurement of the mechanical properties of lipid phases in supported bilayers*, Biophysical Journal 102:1 (2012) L01-L03
- [87] Korshavn K.J., Satriano C., Lin Y., Zhang R., Dulchavsky M., Bhunia A., Ivanova M.I., Lee Y.-H., La Rosa C., Lim M.H., Ramamoorthy A., *Reduced lipid bilayer thickness regulates the aggregation and cytotoxicity of amyloid- β* , Journal of Biological Chemistry 292:11 (2017) 4638-4650
- [88] Beece D., Eisenstein L., Frauenfelder H., Good D., Marden M.C., Reinisch L., Reynolds A.H., Sørensen L.B., Yue K.T., *Solvent viscosity and protein dynamics*, Biochemistry 19 (1980) 5147-5157
- [89] Frauenfelder H., Fenimore P.W., McMahon B.H., *Hydration, slaving and protein function*, Biophysical Chemistry 98 (2002) 35-48
- [90] Peters T., *All about albumin: biochemistry, genetics and medical applications*, Academic Press, San Diego (1997)
- [91] Wood K., Plazanet M., Gabel F., Kessler B., Oesterhelt D., Zaccai G., Weik M., *Dynamics of hydration water in deuterated purple membranes explored by neutron scattering*, European Biophysical Journal 37 (2008) 619-626
- [92] Gallat F.-X., Laganowsky A., Wood K., Gabel F., van Eijck L., Wuttke J., Moulin M., Härtlein M., Eisenberg D., Colletier J.-P., Zaccai G., Weik M., *Dynamical coupling of intrinsically disordered proteins and their hydration water: comparison with folded soluble and membrane proteins*, Biophysical Journal 103:1 (2012) 129-136
- [93] Fichou Y., Schirò G., Gallat F.-X., Laguri C., Moulin M., Combet J., Zamponi M., Härtlein M., Picart C., Mossou E., Lortat-Jacob H., Colletier J.-P., Tobias D.J., Weik M., *Hydration water mobility is enhanced around tau amyloid fibers*, Proceedings of the National Academy of Sciences USA 112:20 (2015) 6365-6370
- [94] Tavagnacco L., Chiessi E., Zanatta M., Orecchini A., Zaccarelli E., *Water-polymer coupling induces a dynamical transition in microgels*, The Journal of Physical Chemistry Letters 10 (2019) 870-876
- [95] Zavoisky E.K., *Paramagnetic relaxation of liquid solutions for perpendicular fields*, Journal of Physics 9 (1945) 211-216

REFERENCES

- [96] Zavoisky E.K., *Paramagnetic absorption in some salts in perpendicular magnetic fields*, Journal of Physics 10 (1946) 170-173
- [97] Zhidomirov G.M., Salikhov K.M., Tsvetkov Yu.D., Yudanov V.F., Raitsimring A.M., *A study of the interaction between paramagnetic species and the magnetic nuclei of the surrounding molecules by electron spin echo spectroscopy*, Zhurnal Strukturnoi Khimii 9:5 (1968) 807-812
- [98] Stine T.J., Buckman T., Nordio P.L., McConnell H.M., *Spin-labeled biomolecules*, Proceedings of the National Academy of Sciences USA 54:4 (1965) 1010-1017
- [99] Marsh D., *Electron spin resonance: spin labels*, in: E. Grell (Ed.), Membrane Spectroscopy, Springer Verlag, Berliner-Heidelberg-New York (1981) 51-143
- [100] Marsh D., *Spin-label EPR for determining polarity and proticity in biomolecular assemblies: transmembrane profiles*, Applied Magnetic Resonance 37 (2010) 435-454
- [101] Van S.P., Birrel G.B., Griffith O.H., *Rapid anisotropic motion of spin labels models for motion averaging of the EPR parameters*, Journal of Magnetic Resonance 15 (1974) 444-459
- [102] Weber R.T., *Elexsys E580 Pulse EPR spectrometer: User's manual*, Bruker BioSpin Corporation, Billerica, MA USA (2001)
- [103] Toropov Yu.V., Dzuba S.A., Tsvetov Yu.D., Monaco V., Formaggio F., Crisma M., Toniolo C., Raap J., *Molecular dynamics and spatial distribution of TOAC spin-labelled peptaibols studied in glassy liquid by echo-detected EPR spectroscopy*, Applied Magnetic Resonance 15 (1998) 237-246
- [104] Dzuba S.A., *Librational motion of guest spin probe molecules in glassy media*, Physics Letters A 213 (1996) 77-84
- [105] Kevan L., Bowman M.K., (eds.), *Modern Pulsed and Continuous-Wave Electron Spin Resonance*, John Wiley & Sons, New York, Chichester (1990)
- [106] Dikanov S.A., Tsvetkov Yu.D., *Electron Spin Echo Envelope Modulation (ESEEM) Spectroscopy*, CRC Press, Boca Raton, FL (1992)
- [107] Bartucci R., Guzzi R., Sportelli L., Marsh D., *Intramembrane water associated with TOAC spin-labeled alamethicin: electron spin-echo envelope modulation by D₂O*, Biophysical Journal 96:3 (2009) 997-1007

REFERENCES

- [108] Milov A.D., Samoilova R.I., Shubin A.A., Grishin Yu.A., Dzuba S.A., *ESEEM measurements of local Water concentration in D₂O-containing spin-labeled systems*, Applied Magnetic Resonance 35 (2008) 73-94
- [109] Kurshev V., Kevan L., *Electron spin echo modulation studies of doxylstearic acid spin probes in frozen vesicle solutions: interaction of the spin probe with 31P in the surfactant headgroups*, The Journal of Physical Chemistry 99:26 (1995) 10616-10620
- [110] Marsh D., Watts A., *Spin-labeling and lipid-protein interactions in membranes*. In: Jost P.C.G., Hayes O. (eds.), *Lipid-Protein Interactions* vol. 2, Wiley-Interscience, New York (1982)
- [111] Volke F., Eisenblätter S., Galle J., Klose G., *Dynamic properties of water at phosphatidylcholine lipid-bilayer surfaces as seen by deuterium and pulsed field gradient proton NMR*, Chemistry and Physics of Lipids 70 (1994) 121-131
- [112] Hristova K., White, S.H., *Determination of the hydrocarbon core structure of fluid DOPC bilayers by x-ray diffraction using specific bromination of the double-bonds: effect of hydration*, Biophysical Journal 74 (1998) 2419-2433
- [113] Zhang Z., Berkowitz M.L., *Orientational dynamics of water in phospholipid bilayers with different hydration levels*, The Journal of Physical Chemistry B, 113 (2009) 7676-7680
- [114] Tristram-Nagle S., *Use of X-ray and neutron scattering methods with volume measurements to determine lipid bilayer structure and number of water molecules/lipid*. In: Disalvo E.A. (eds.), *Membrane hydration: the role of water in the structure and function of biological membranes*, Springer, Switzerland (2015)
- [115] Pantusa M., Sportelli L., Bartucci R., *Spectroscopic and calorimetric studies on the interaction of human serum albumin with DPPC/PEG:2000-DPPE membranes*, European Biophysical Journal 37 (2008) 961-973
- [116] Aloï E., Bartucci R., *Solvent accessibility in interdigitated and micellar phases formed by DPPC/Lyso-PPC mixtures: D₂O-ESEEM of chain labeled lipids*, Chemistry and Physics of Lipids 221 (2019) 39-45
- [117] Aloï E., Bartucci R., *Interdigitated lamellar phases in the frozen state: spin-label CW- and FT- EPR*, Biophysical Chemistry 253 (2019) 106229

REFERENCES

- [118] Aloï E., Bartucci R., *Cryogenically frozen PEGylated liposomes and micelles: water penetration and polarity profiles*, *Biophysical Chemistry* 266 (2020) 106463
- [119] Aloï E., Guo J.-H., Guzzi R., Jiang R.-W., Ladefoged L.K., Marsh D., Es-
mann M., Bartucci R., Fedosova N.U., *Geometry and water accessibility of the
inhibitor binding site of Na⁺-pump: pulse- and CW-EPR study*, *Biophysical
Journal* (2021) <https://doi.org/10.1016/j.bpj.2021.05.018>
- [120] Israelachvili J.N., *Intermolecular and surface forces - Third edition*, Academic
Press, London (2011)
- [121] Belsito S., Bartucci R., Montesano G., Marsh D., Sportelli L., *Molecu-
lar and mesoscopic properties of hydrophilic polymer-grafted phospholipids
mixed with phosphatidylcholine in aqueous dispersion: interaction of dipalmito-
yl N-poly(ethylene-glycol)phosphatidylethanolamine with dipalmitoylphos-
phatidylcholine studied by spectrophotometry and spin-label Electron spin res-
onance*, *Biophysical Journal* 78 (2000) 1420-1430
- [122] Montesano G., Bartucci R., Belsito S., Marsh D., Sportelli L., *Lipid membrane
expansion and micelle formation by polymer-grafted lipids: scaling with poly-
mer length studied by spin-label Electron spin resonance*, *Biophysical Journal*
80 (2001) 1372-1383
- [123] Bartucci R., Pantusa M., Marsh D., Sportelli L., *Interaction of human serum
albumin with membranes containing polymer-grafted lipids: spin-label ESR
studies in the mushroom and brush regimes*, *Biochimica et Biophysica Acta*
1564 (2002) 237-242
- [124] Tirosh O., Barenholz Y., Katzhendler J., Prieval A., *Hydration of poly(ethylene
glycol)-grafted liposomes*, *Biophysical Journal* 74 (1998) 1371-1379
- [125] Stirpe A., Pantusa M., Guzzi R., Bartucci R., Sportelli L., *Chain interdigitation
in DPPC bilayers induced by HgCl₂: evidences from continuous wave and
pulsed EPR*, *Chemistry and Physics of Lipids* 183 (2014) 176-183
- [126] Kenworthy A.K., Simon S.A., McIntosh T.J., *Structure and phase behav-
ior of lipid suspensions containing phospholipids with covalently attached
poly(ethyleneglycol)*, *Biophysical Journal* 68 (1995) 1903-1920
- [127] Johnsson M., Edwards K., *Liposomes, disks, and spherical micelles: aggre-
gate structure in mixtures of gel phase phosphatidylcholines and poly(ethylene
glycol)-phospholipids*, *Biophysical Journal* 85 (2003) 3839-3847

REFERENCES

- [128] Marsh D., *Polarity and permeation profiles in lipid membranes*, Proceedings of the National Academy of Sciences USA 98 (2001) 7777-7782
- [129] Bartucci R., Guzzi R., Marsh D., Sportelli L., *Intramembrane polarity by electron spin echo spectroscopy of labeled lipids*, Biophysical Journal 84 (2003) 1025-1030
- [130] Simon S.A., McIntosh T.J., *Interdigitated hydrocarbon chain packing causes the biphasic transition behavior in lipid/alcohol suspensions*, Biochimica et Biophysica Acta 773 (1984) 169-172
- [131] Lobbecke L., Cevc G., *Effects of short-chain alcohols on the phase behavior and interdigitation of phosphatidylcholine bilayer membranes*, Biochimica et Biophysica Acta 1237 (1995) 59-69
- [132] Bartucci R., Pali T., Marsh D., *Lipid chain motion in an interdigitated gel phase: conventional and saturation transfer ESR of spin-labeled lipids in dipalmitoylphosphatidylcholine-glycerol dispersions*, Biochemistry 32 (1993) 274-281
- [133] Pali T., Bartucci R., Horv ath L.I., Marsh D., *Kinetics and dynamics of annealing during sub-gel phase formation in phospholipid bilayers: A saturation transfer electron spin resonance study*, Biophysical Journal 64 (1993) 1781-1788
- [134] Subczynski W.K., Wisniewska A., Yin J.J., Hyde J.S., Kusumi A., *Hydrophobic barriers of lipid bilayer membranes formed by reduction of water penetration by alkyl chain unsaturation and cholesterol*, Biochemistry 33 (1994) 7670-7681
- [135] Kurad D., Jeschke G., Marsh D., *Lipid membrane polarity profiles by high-field EPR*, Biophysical Journal 85 (2003) 1025-1033
- [136] Oranges M., Guzzi R., Marsh D., Bartucci R., *Ether-linked lipids: spin-label EPR and spin echoes*, Chemistry and Physics of Lipids 212 (2018) 130-137
- [137] Bartucci R., Belsito S., Sportelli L., *Spin-label electron spin resonance studies of micellar dispersions of Pegs-Pes polymer-lipids*, Chemistry and Physics of Lipids 124 (2003) 11-122
- [138] Szajdzinska-Pietek E., Maldonado R., Kevan L., Jones R.R.M., *Electron spin resonance and electron spin echo modulation studies of N,N,N',N'-tetramethylbenzidine photoionization in anionic micelles: structural effects of tetramethylammonium cation counterion substitution for sodium cation in dodecyl*

REFERENCES

- sulphate micelles*, Journal of the American Chemical Society 106 (1984) 4675-4678
- [139] Bartucci R., Guzzi R., Esmann M., Marsh D., *Water penetration profile at the protein-lipid interface in Na,K-ATPase membranes*, Biophysical Journal 107 (2014) 1375-1382
- [140] Laursen M., Gregersen J.L., Yatime L., Nissen P., Fedosova N.U., *Structures and characterization of digoxin- and bufalin-bound Na⁺,K⁺-ATPase compared with the ouabain-bound complex*, Proceedings of the National Academy of Sciences USA 112 (2015) 1755-1760
- [141] Guo J.H., Jiang R.W., Andersen J.L., Esmann M., Fedosova N.U., *Spin-labeled derivatives of cardiotonic steroids as tools for characterization of the extracellular entrance to the binding site on Na⁺,K⁺-ATPase*, The FEBS Journal 285 (2018) 2292-2305
- [142] De Simone F., Guzzi R., Sportelli L., Marsh D., Bartucci R., *Electron spin-echo studies of spin-labeled lipid membranes and free fatty acids interacting with human serum albumin*, Biochimica et Biophysica Acta 1768 (2007) 1541-1549
- [143] Aloï E., Guzzi R., Bartucci R., *Unsaturated lipid bilayers at cryogenic temperature: librational dynamics of chain-labeled lipids from pulsed and CW-EPR*, Physical Chemistry Chemical Physics 21 (2019) 18699-18705
- [144] O'Leary T., Levin I., *Raman spectroscopic study of an interdigitated lipid bilayer dipalmitoylphosphatidylcholine dispersed in glycerol*, Biochimica et Biophysica Acta 776 (1984) 185-189
- [145] Boggs J.M., Rangaraj G., Watts A., *Behavior of spin labels in a variety of interdigitated lipid bilayers*, Biochimica et Biophysica Acta 981 (1989) 243-253
- [146] Bartucci R., Belsito S., Sportelli L., *Neutral lipid bilayers interacting with chaotropic anions*, Chemistry and Physics of Lipids 79 (1996) 171-180
- [147] Paschenko S.V., Toropov Y.V., *Temperature dependence of amplitudes of libration motion of guest spin-probe molecules in organic glasses*, The Journal of Chemical Physics 110 (1999) 8150-8154
- [148] Poluektov O.G., Utschig L.M., Dalosto S., Thurnauer M.C., *Probing local dynamics of the photosynthetic bacterial reaction center with a cysteine specific spin label*, The Journal of Physical Chemistry B 107 (2003) 6239-6244

REFERENCES

- [149] Borovykh I.V., Gast P., Dzuba S.A., *The dynamical transition in proteins of bacterial photosynthetic reaction centers observed by echo-detected EPR of specific spin labels*, Applied Magnetic Resonance 31 (2007) 159-166
- [150] Golysheva E.A., Shevelev G.Y., Dzuba S.A., *Dynamical transition in molecular glasses and proteins observed by spin relaxation of nitroxide spin probes and labels*, The Journal of Chemical Physics 147 (2017) 064501
- [151] Surovtsev N.V., Dzuba S.A., *Conformational changes of lipids in bilayers at the dynamical transition near 200 K seen by Raman scattering*, The Journal of Physical Chemistry B 113 (2009) 15558-15562
- [152] Surovtsev N.V., Dzuba S.A., *Flexibility of phospholipids with saturated and unsaturated chains studied by Raman scattering: the effect of cholesterol on dynamical and phase transitions*, The Journal of Chemical Physics 140 (2014) 235103
- [153] Blocher D., Six L., Gutermann R., Henkel B., Ring K., *Physicochemical characterization of tetraether lipids from thermoplasma-acidophilum: calorimetric studies on miscibility with diether model lipids carrying branched or unbranched alkyl chains*, Biochimica et Biophysica Acta: Biomembranes 818 (1985) 333-342
- [154] Shalaev E.Y., Zografi G., Steponkus P.L., *Occurrence of glass transitions in long-chain phosphatidylcholine mesophases*, The Journal of Physical Chemistry B 114 (2010) 3526-3533
- [155] Golysheva E.A., De Zotti M., Toniolo C., Formaggio F., Dzuba S.A., *Low-temperature dynamical transition in lipid bilayers detected by spin-label ESE spectroscopy*, Applied Magnetic Resonance 49 (2018) 1369-1383
- [156] Loch J., Polit A., Gorecki A., Bonarek P., Kurpiewska K., Dziejzicka-Wasylewska M., Lewinski K., *Two modes of fatty acid binding to bovine beta-lactoglobulin: crystallographic and spectroscopic studies*, Journal of Molecular Recognition 24 (2011) 341-349
- [157] Sugio S., Kashima A., Mochizuki S., Noda M., Kobayashi K., *Crystal structure of human serum albumin at 2.5 Å resolution*, Protein Engineering, Design and Selection 12:6 (1999) 439-446
- [158] Marzola P., Cannistraro S., *Hydration and protein dynamics: an ESR and ST-ESR spin labelling study of Human Serum Albumin*, Applied Magnetic Resonance 3 (1992) 1045-1060

REFERENCES

- [159] Johnson M.E., *Apparent hydrogen bonding by strongly immobilized spin-labels*, *Biochemistry* 20 (1981) 3319-3328
- [160] Orecchini A., Paciaroni A., Bizzarri A.R., Cannistraro S., *Dynamics of different hydrogen classes in β -lactoglobulin: a quasielastic neutron scattering investigation*, *The Journal of Physical Chemistry B* 106 (2002) 7348-7354
- [161] Miyatou T., Araya T., Ohashi R., Ida T., Mizuno M., *Hydration water dynamics in bovine serum albumin at low temperatures as studied by deuterium solid-state NMR*, *Journal of Molecular Structure* 1121 (2016) 80-85
- [162] Combarro Palacios I., Olsson C., Kamma-Lorger C.S., Swenson J., Cervený S., *Motions of water and solutes: slaving versus plasticization phenomena*, *Journal of Chemical Physics* 150 (2019) 124902
- [163] Pinnick E.R., Erramilli S., Wang F., *Computational investigation of lipid hydration water of $L\alpha$ 1-palmitoyl-2-oleoyl-sn-glycero-3-phosphocholine at three hydration levels*, *Molecular Physics* 108:15 (2010) 2027-2036
- [164] Chadwick J., *Possible existence of a neutron*, *Nature* 129 (1932) 312
- [165] Fermi E., Zinn W.H., *Reflection of neutrons on mirrors*, *Physical Review* 70 (1946) 103
- [166] Belushkin A.V., *Neutron scattering: history, present state and perspectives*, *Joint Institute for Nuclear Research* 152 (1999) E14
- [167] Squires G.L., *Introduction to the theory of thermal neutron scattering*, Cambridge University Press, Cambridge (1972)
- [168] Bée M., *Quasielastic neutron scattering: principles and applications in solid state chemistry, biology, and material science*, Adam Hilger, Bristol (1988)
- [169] Van Hove L., *Correlations in space and time and born approximation scattering in systems of interacting particles*, *Physical Review* 95:1 (1954) 249-262
- [170] Schirò G., *Probing the dynamics of biological matter by elastic, quasi-elastic, and inelastic neutron scattering*, *EPJ Web of Conferences* 236 (2020) 05001
- [171] Teixeira J., Bellissent-Funel M.-C., Chen S.H., Dianoux A.J., *Experimental-determination of the nature of diffusive motions of water-molecules at low-temperatures*, *Physical Review A: Atomic, Molecular and Optical Physics* 31:3 (1985) 1913-1917

REFERENCES

- [172] Schirò G., Weik M., *Role of hydration water in the onset of protein structural dynamics*, Journal of Physics: Condensed Matter 31 (2019) 463002
- [173] Benedetto A., *Low-temperature decoupling of water and protein dynamics measured by neutron scattering*, The Journal of Physical Chemistry Letters 8:19 (2017) 4883-4886
- [174] Kämpf K., Demuth D., Zamponi M., Wuttke Z., Vogel M., *Quasielastic neutron scattering studies on couplings of protein and water dynamics in hydrated elastin*, The Journal of Chemical Physics 152:24 (2020) 245101
- [175] Pounot K., Chaaban H., Foderà V., Schirò G., Weik M., Seydel T., *Tracking internal and global diffusive dynamics during protein aggregation by high-resolution neutron spectroscopy*, The Journal of Physical Chemical Letters 11:15 (2020) 6299-6304
- [176] Weik M., Lehnert U., Zaccai G., *Liquid-like water confined in stacks of biological membranes at 200 K and its relation to protein dynamics*, Biophysical Journal 89:5 (2005) 3639-3646
- [177] Yamada T., Takahashi N., Tominaga T., Takata S., Seto H., *Dynamical behavior of hydration water molecules between phospholipid membranes*, The Journal of Physical Chemistry B 121:35 (2017) 8322-8329
- [178] Mamontov E., O'Neill H., *Microscopic relaxations in a protein sustained down to 160 K in a non-glass forming organic solvent*, Biochimica et Biophysica Acta 1861 (2017) 3513-3519
- [179] Meineke J., Weik M., Zaccai G., Fragneto G., *Behavior of hydrated lipid bilayers at cryogenic temperatures*, Frontiers in Chemistry 8 (2020) 455
- [180] Yepuri N.R., Darwish T.A., Krause-Heuer A.M., Leung A.E., Delhom R., Wacklin H.P. Holden P.J., *Synthesis of perdeuterated 1-palmitoyl-2-oleoyl-sn-glycero-3-phosphocholine ([d82]POPC) and characterisation of its lipid bilayer membrane structure by neutron reflectometry*, ChemPlusChem 81:3 (2016) 315-321
- [181] Tan P., Li J., Hong L., *Statistical properties for diffusive motion of hydration water on protein surface*, Physica B: Condensed Matter 562 (2019) 1-5
- [182] Unruh T., Neuhaus J., Petry W., *The high-resolution time-of-flight spectrometer TOFTOF*, Nuclear Instruments and Methods in Physics Research A 580 (2007) 1414-1422

REFERENCES

- [183] Heinz Maier-Leibnitz Zentrum et al., *TOFTOF: Cold neutron time-of-flight spectrometer*, Journal of large-scale research facilities 1:A15 <http://dx.doi.org/10.17815/jlsrf-1-40> (2015)
- [184] Hill E., Wall M.J., Moffat K.G., Karikari T.K., *Understanding the pathophysiological actions of Tau oligomers: a critical review of current electrophysiological approaches*, Frontiers in Molecular Neuroscience 13 (2020) 155
- [185] Amann-Winkel K., Bellissent-Funel M.-C., Bove L.E., Loerting T., Nilsson A., Paciaroni A., Schlesinger D., Skinner L., *X-ray and neutron scattering of water*, Chemical Reviews 116 (2016) 7570-7589
- [186] Dembinski H., Ongmongkolkul P., Deil C., Menéndez Hurtado D., Schreiner H., Feickert M., ..., Zapata O., scikit-hep/iminuit: v2.3.0 (Version v2.3.0). Zenodo. <http://doi.org/10.5281/zenodo.4460551> (2021)

Acknowledgments

I am deeply grateful to all the people I have met along the way of this incredible journey that is coming to the end.

I want to remember with gratitude the mentorship of Prof. Luigi Sportelli, who guided my first steps in academic research during my Bachelor's.

I would like to express my sincere appreciation to my supervisor, Prof. Rosa Bartucci, for her patience and enthusiasm in guiding me through my research path, and for her friendship.

Special thanks to Prof. Rita Guzzi and Dr. Bruno Rizzuti for their insightful and precious advice.

Appreciation and deep gratitude are owed to all the members of the Weik's group in Grenoble for their warm welcoming and for making me feel at home. In particular, thanks to Dr. Giorgio Schirò for his unwavering support throughout these years.

I would like to thank all the committee members and referees for dedicating their time to evaluate my research.

To all the colleagues of the Physics department that I am so lucky to call friends, thank you for sharing with me the emotional roller-coaster of this long college experience.

Thanks to my family and beloved ones for their tremendous understanding and treasured encouragement all through my studies. This accomplishment would not have been possible without you.